Synthesis, Characterization and Application of intermetallic Pd-X (Ga, Zn) Nanoparticles derived from ternary Hydrotalcite-like precursors

vorgelegt von
Diplomchemikerin
Antje Ota
aus Hennigsdorf

Von der Fakultät II - Mathematik und Naturwissenschaften
der Technischen Universität Berlin
zur Erlangung des akademischen Grades
Doktorin der Naturwissenschaften
Dr. rer. nat.

genehmigte Dissertation

Promotionsausschuss:

Vorsitzender: Prof. Dr. Reinhard Schomäcker
Berichter/Gutachter: Prof. Dr. Robert Schlögl
Berichter/Gutachter: Prof. Dr. Thorsten Ressler
Berichter/Gutachter: Prof. Dr. Günther Rupprechter

Tag der wissenschaftlichen Aussprache: 27.03.2012

Berlin, 2012
D 83

Abstract

A novel, feasible synthesis approach for supported intermetallic Pd_2Ga and $PdZn$ nanoparticles derived from Hydrotalcite-like compounds (HTlc) is introduced. Ternary HTlc with the nominal composition $(Pd^{2+},M^{2+})_{0.70}(M^{3+})_{0.30}(OH)_2(CO_3)_{0.15} \cdot m\ H_2O$ are synthesized by pH-controlled co-precipitation. Mg^{2+}/Ga^{3+} and Zn^{2+}/Al^{3+} are chosen as M^{2+}/M^{3+} combinations to permit formation of the nanocrystalline Pd_2Ga and $PdZn$ intermetallic compounds on a porous $MgO/MgGa_2O_4$ and $ZnO/ZnAl_2O_4$ support, respectively. In addition, a PdMgAl HTlc is prepared as monometallic Pd reference compound on a $MgO/MgAl_2O_4$ support.

Incorporation of Pd^{2+} into the HTlc structure requires octahedral coordination, while Pd^{2+} ions prefer square planar coordination in aqueous solution. At the same substitution degree of M^{2+} by Pd^{2+}, complete insertion is achieved for PdZnAl HTlc. In case of PdMgGa and PdMgAl HTlc a minor fraction is present as segregated Pd^{2+} on the external surface of the platelet-like particles with a local environment similar to PdO, i.e. in a square planar coordination. A limit of incorporation into the HTlc lattice exists at < 1 mol% for the Pd^{2+} containing precursors.

Upon thermal decomposition in reductive atmosphere, intermetallic and metallic nanoparticles ranging from below 2 nm to 6 nm in size and exhibiting monomodal particle size distributions are formed. Alloying of Pd with Ga and Zn changes the crystal structure as well as the electronic structure and leads to the increased formation of isolated adsorption sites at the surface. Furthermore, dynamic surface changes of intermetallic Pd_2Ga nanoparticles were noticed at longer exposure time to CO and higher CO coverage. This is attributed to the decomposition into metallic Pd and Ga_2O_3.

The nanostructured Pd_2Ga catalyst shows excellent performance in the selective semi-hydrogenation of acetylene similar to a bulk Pd_2Ga model catalyst. In comparison to the elemental Pd catalyst the selectivity to ethylene is drastically improved by formation of Pd_2Ga. Interestingly, the nanostructered catalyst slowly activates in the feed gas. The activation is triggered faster by a treatment in oxidative atmosphere. These dynamics of the Pd_2Ga nanoparticles can be explained by the interplay of surface decomposition into Pd^0 and Ga_2O_3 in oxygen and reversal of the strong-metal support interaction state leading to an increased activity.

Furthermore, increased activities and selectivities in methanol steam reforming and methanol synthesis from CO_2 are observed for the Pd_2Ga and $PdZn$ nanoparticles in contrast to the unmodified Pd particles. These structurally modified Pd catalysts exhibit a considerably lower selectivity to CO and enhanced formation of methanol compared to the monometallic Pd catalyst.

Zusammenfassung

Für die Herstellung von geträgerten, intermetallischen Pd_2Ga und PdZn Nanopartikeln wird ein neuartiger, leicht anwendbarer Syntheseansatz aus Hydrotalcit-ähnlichen (HT) Verbindungen vorgestellt. Die ternären HT Verbindungen mit der nominellen Zusammensetzung $(Pd^{2+},M^{2+})_{0.70}(M^{3+})_{0.30}(OH)_2(CO_3)_{0.15} \cdot m\ H_2O$ werden durch pH-kontrollierte Co-Fällung hergestellt. Die Kombination der zwei- und dreiwertigen Kationen variiert zwischen Mg^{2+}/Ga^{3+} bzw. Zn^{2+}/Al^{3+}, um die Bildung von nanokristallinen Pd_2Ga und PdZn intermetallischen Verbindungen geträgert auf porösem $MgO/MgGa_2O_4$ bzw. $ZnO/ZnAl_2O_4$ Support zu ermöglichen. Zusätzlich wird für die Herstellung einer monometallischen Pd-Referenz auf einem $MgO/MgAl_2O_4$ Träger ein PdMgAl HT synthetisiert.

Der erfolgreiche Einbau von Pd in die HT Struktur erfordert eine oktaedrische Koordination des Pd^{2+}, wobei Pd^{2+} Ionen in wässriger Lösung bevorzugt quadratisch planar koordiniert vorliegen. Bei gleichem Substitutionsgrad von M^{2+} durch Pd^{2+} konnte vollständiger Pd Einbau für die PdZnAl HT Verbindung erreicht werden. Im Falle von PdMgGa und PdMgAl HT liegt ein geringer Anteil des Pd^{2+} in segregierter Form auf der Oberfläche der HT Plättchen vor. Das nicht eingebaute Pd weist eine ähnliche Koordinationssphäre wie quadratisch planar koordiniertes Pd^{2+} in PdO auf. Die Grenze für den vollständigen Einbau von Pd^{2+} liegt bei unter 1 mol% Pd.

Die thermische Zersetzung in reduzierender Atmosphäre führt zur Bildung von intermetallischen und metallischen Nanopartikeln in der Größenordnung von unter 2 bis 6 nm und monomodaler Partikelgrößenverteilung. Durch das Legieren von Pd mit Ga bzw. Zn wird sowohl die Kristallstruktur als auch die elektronische Struktur verändert, was zur Ausbildung von isolierten Adsorptionszentren an der Oberfläche führte. Des Weiteren wurde bei längerer CO Exposition und erhöhten CO Drücken eine dynamische Veränderung der Pd_2Ga Oberfläche beobachtet. Dies lässt sich durch die Zersetzung von Pd_2Ga zu metallischem Pd und Ga_2O_3 erklären.

Der nanostrukturierte Pd_2Ga Katalysator erzielt im Vergleich zum Pd_2Ga Bulkkatalysator ähnliche Selektivität und Stabilität in der selektiven Semihydrierung von Ethin. Die Selektivität zu Ethen verbesserte sich gegenüber metallischem Palladium deutlich durch die Bildung der intermetallischen Pd_2Ga Phase. Interessanterweise wird eine langsame Aktivierung des Katalysators im Reaktionsgas beobachtet, die sich mittels oxidativer Vorbehandlung drastisch verkürzt. Diese Dynamik kann durch das Zusammenspiel von der Oberflächenzersetzung zu Pd^0 und Ga_2O_3 und der Umkehrung der starken Metall-Träger-Wechselwirkung erklärt werden, was zu einer deutlichen Aktivitätserhöhung führt.

Zusätzlich zeigten Pd_2Ga und PdZn Nanopartikel im Gegensatz zum reinen Pd Katalysator erhöhte Aktivitäten und Selektivitäten in der Reformierung von Methanol und der Methanolsynthese. Diese strukturell modifizierten Pd Katalysatoren weisen im Vergleich zum monometallischen Pd Katalysator deutlich verringerte CO Selektivitäten und erhöhte Bildung von Methanol auf.

Danksagung

Zu Beginn dieser Arbeit möchte ich mich ganz herzlich bei all denjenigen bedanken, die mich in den letzten Jahren und insbesondere in den letzten Monaten, sei es wissenschaftlich oder auch moralisch gewesen, unterstützt und zum Gelingen dieser Arbeit beigetragen haben.

Mein besonderer Dank gilt Prof. Schlögl für die interessante wissenschaftliche Fragestellung, die mit dieser Arbeit verbunden war. Ich bedanke mich für das in mich gesetzte Vertrauen und die stete Unterstützung während meiner Zeit am Fritz-Haber-Institut. Zudem möchte ich ausdrücklich meinem Gruppenleiter Dr. Malte Behrens für sein enormes Motivationsvermögen, die Diskussionsbereitschaft und seine stets offene Bürotür danken.

Ferner bedanke ich mich speziell bei der Nanostructure-Gruppe für die wissenschaftliche und moralische Unterstützung. Insbesondere danke ich Stefan Zander und Dr. Thomas Cotter für das außerordentlich angenehme Büroklima und ihre Unterstützung bei der Bewältigung des wissenschaftlichen Alltags. Sylvia Reiche, Steffi Kühl, Gregor Wowsnick, Dr. Edward Kunkes, Dr. Dirk Rosenthal, Pierre Kube, Klaus Friedel und Julia Neuendorf danke ich für die interessanten Unterhaltungen sowohl in beruflichem als auch privatem Kreis. Weiterhin bedanke ich mich bei all den fleißigen Helfern, die mit ihren Messungen meiner Proben einen entscheidenden Anteil an dieser Arbeit haben: Edith Kitzelmann (XRD und TG), Dr. Andrey Tarasov (TG), Gisela Lorenz und Maike Hashagen (BET), GiselaWeinberg (SEM), Jutta Kröhnert und Neil Hamilton (IR), Dr. Igor Kasatkin, Dr. Wei Zhang und Dr. Marc Willinger (TEM). Des Weiteren möchte ich mich bei allen anderen, nicht namentlich genannten Mitarbeitern für die ausgesprochen angenehme und kollegiale Arbeitsatmosphäre bedanken.

Der Deutschen Forschungsgemeinschaft möchte ich für die finanzielle Unterstützung danken, die meine Forschungsarbeit in Rio den Janeiro in Brasilien, einer der angeblich schönsten Städte der Welt, ermöglichte. Prof. Schmal sowie Dr. Fabio Toniolo, Dr. Marta Amorim de Carvalho, Antônio José de Almeida, Maria Auxiliadora S. Baldanza und Rodrigo Brackmann der Universidade Federal do Rio de Janeiro danke ich für angenehme Zusammenarbeit und die unvergessliche Zeit.

Zu Dank verpflichtet bin ich ebenfalls Dr. Marc Armbrüster und Matthias Friedrich, welche es ermöglichten, Katalysemessungen am Max-Planck-Institut für Chemische Physik fester Stoffe in Dresden durchzuführen. Desweiteren danke ich Dr. Olga Safanova und Dr. Maarten Nachtegaal für die Unterstützung während der Messzeit an der SLS Super-XAS Beamline am Paul-Scherrer-Institut in Villigen.

Meinen Eltern und meinem Freund Matthias Zwick möchte ich an dieser Stelle danken für ihre Unterstützung, das Vertrauen und die Zuversicht, die sie mir entgegen gebracht haben und dass sie immer für mich da gewesen sind.

Table of Contents

List of Figures

List of Tables

List of Abbreviations

BET	adsorption isotherm model of Brunauer, Emmet and Teller
DSC	differential scanning calorimetry
EDX	energy dispersive X-ray spectroscopy
FT-IR	fourier transformed infrared spectroscopy
HRTEM	high resolution transmission electron microscopy
HTlc	hydrotalcite-like compound
ICP-OES	inductively coupled plasma optical emission spectrometry
IMC	intermetallic compound
IR	infrared spectroscopy
MS	mass spectrometry
MSR	methanol steam reforming
PSD	particle size distribution
SSA	specific surface area
SEM	scanning electron microscopy
STEM	scanning transmission electron microscopy
S.V.	space velocity
TCD	thermal conductivity detector
TEM	transmission electron microscopy
TG(A)	thermo gravimetry (analysis)
TOS	time on stream
TPO	temperature programmed oxidation
TPR	temperature programmed reduction
XANES	x-ray absorption near edge spectroscopy
XPS	x-ray photoelectron spectroscopy
XRD	x-ray diffraction

Chapter 1: Introduction and Overview

Preface

The first chapter will give a broad overview about the relevant literature, open questions and research strategy that will be presented and discussed in the following chapters. First, the class of intermetallic compounds (IMCs) and its relevance as a research subject will be introduced. Subsequently attention will be shifted to the novel synthesis approach, which was applied to obtain nanoparticulate IMCs. On basis of this approach metallic and intermetallic compounds were synthesized and tested for different kinds of reactions.

In this thesis the focus is placed in particular on the Pd-Ga system. In addition the Pd-Zn and monometallic Pd system will also be discussed as another IMC example and reference system respectively. Moreover, the catalytically relevant reactions, which are the subject of the following chapters, will be briefly introduced.

1.1.   Intermetallic compounds

IMCs result from the combination of various metals and form a large and manifold class of materials.[1] According to the simple definition given by Schulze [2] intermetallics are compounds whose crystal structure is different from those of the constituent metals. In contrast to some other alloys, they are single-phase materials and their crystal structure and properties are determined by the strength and character of the bonding in the crystal. Partly covalent or ionic character of intermetallic compounds lead to higher structural stability and less segregation compared to alloys. Contribution of covalent or ionic bonding of IMCs result in reduced ductility and reduced electric conductivity compared to pure metals or alloys consisting of miscible metals. Their classification is rather complicated and presence of the same crystal structure does not automatically lead to similarities with respect to bonding and properties. Thus, intermetallics are grouped according to similarities in properties rather than crystal structure. Furthermore, IMCs do often not possess a strictly defined stoichiometric composition, instead they are stabile over a broad homogeneity range. For instance, in γ- brass the Zn content may vary from 60 - 70 at%. Nevertheless, small changes in composition can be of crucial importance for physical properties. For example the ferromagnetic Laves-phase $ZrFe_2$ has a homogeneity range from 66 - 72.5 at% Fe. Depending on the composition the Curie-temperature varies from 610 K at 66.7 at% to 798 K at 72.3 at% Fe.[2]

Intermetallic compounds are known since ancient time [1] and the discovery of first intermetallics resulting from alloys with low melting temperatures marked the epoch of the Bronze age around 3000 B.C. Their outstanding hardness, wear resistance and metallic properties were important for their application as weapons, tools and coins. Also decorative aspects played a role in their application because of their metallic brilliance. Bronze coatings in the ancient Egypt (2500 B.C.) and the mirrors used by ancient Chinese (206 B.C. – 220 A.D.) are classical examples.[3]

Early work on intermetallics during the first decades of last century basically included studies of phase stabilities, phase equilibria and phase transitions in order to establish phase diagrams. Furthermore, studies of various properties were performed, i.e. chemical and electrochemical properties, physical properties including magnetism and superconductivity, and mechanical properties were investigated. In second half of the last century intermetallics were first employed for functional materials application that go far beyond the classical functions in the metal industry. The first industrial applications relied on the special magnetic behavior of ternary FeSiAl phases (Sendust), which were widely used for wear resistant, magnetic heads in tape recorders.[4, 5] In addition, aluminides attracted attention with respect to applications at high temperatures. For instance, the NiAl exhibit low density, good thermal stability, high melting point (1913 K) and excellent oxidation resistance allowing the several potential engineering applications such coatings, turbine blades and vanes, semiconductor or high voltage electrodes.[1, 6] The only catalytic application of commercial significance so far is Raney nickel catalyst, which is most commonly used for hydrogenation reactions.[7] The preparation is carried out by melting of a mixture of 30-50 wt% Ni with 50-70 wt% Al, whereas depending on the initial chemical composition different Ni-Al intermetallic compounds are formed, primary $NiAl_3$, Ni_2Al_3 und NiAl.[8, 9] Subsequent leaching by sodium hydroxide leads to the active phase and dissolves most of the Al. While Ni_2Al_3 and $NiAl_3$ readily leach and form a tight skeletal Ni structure, the NiAl phase is only slightly soluble. The porous structure left behind has a large specific area, which gives a high catalytic activity.

1.2. Motivation

At the beginning of this century Pd-Ga IMCs became of academic interest because of their extraordinary catalytic performance in industrially relevant selective hydrogenation of acetylene to ethylene. Most commonly used industrial catalyst for this process is based on Pd-Ag alloys supported on Al_2O_3.[10] , but it is usually complicated to define the active-sites for supported metal, metal mixture and alloy catalysts. Therefore well-defined, ordered and in-situ stable

unsupported Pd-Ga IMCs were employed as model system. In the crystal structure of PdGa and Pd_3Ga_7 compound, the Pd atoms are exclusively coordinated by Ga atoms, which allow the isolation of the active sites. These sites were directly correlated with the catalytic performance of these materials.[11-13] As mentioned, these compounds are model system and during the last years the research interest in the preparation of nanostructured systems has grown constantly. The focus is placed on the size reduction of already existing bulk phases to transfer the properties of the model system to real applications. Nanocrystalline intermetallics are high surface materials which exhibit a higher dispersion of the noble metal species and therefore possess enormous potential for application as low-cost and high-performance catalyst.

1.3.   Synthesis strategy for binary Pd-X intermetallic nanoparticles

Intermetallics are traditionally synthesized using metallurgical techniques, which require high temperature and long annealing periods. These techniques lead to well-defined and phase-pure model materials, which are very useful to study the intrinsic properties of IMCs. Unfortunately, these materials obtained in thermodynamic equilibrium, exhibit rather low specific surface area (typically < 1 m^2/g). Top-down approaches, e.g. milling or etching of intermetallic compounds, lead to an increase in surface area [14], but partially destroy the IMC crystal. In order to synthesize nanoparticulate intermetallics various synthetic approaches have been applied in literature, for instance co-reduction of organometallic metal precursors. Single-phase and nanosized Pd-Ga intermetallic compounds were synthesized by co-reduction of $GaCl_3$ and $Pd(acac)_2$ in THF by Superhydride.[15] The synthesis leads to very small particles of the intermetallic compounds and surface areas higher than 2 m^2/g. However, this method of preparation necessitates expensive reactants as well as inert atmosphere during the synthesis process. A more feasible preparation was obtained by co-impregnation of the metal nitrates on CNT. Subsequent calcination and reduction at 823 K lead to nanocrystalline Pd_2Ga supported on CNT.[16] Furthermore, the reaction between noble metal and the oxide support was applied for the controlled and target-oriented preparation of supported and dispersed IMCs. Pd supported on Ga_2O_3 and ZnO has been first studied by Iwasa et al. [17, 18]. The IMCs were formed by reductive treatment at elevated temperatures. In order to obtain homogenous materials, it is important to control the particle size and the metal distribution during the whole synthesis. This can be difficult because of the high adhesive forces of Pd nanoparticles and their tendency to form agglomerates. Inhomogeneous particle size distribution may affect the formation process of the IMCs and can also lead to incomplete phase formation. Furthermore,

scalability and reproducibility are crucial aspects of the synthesis procedure, which are sometimes hard to realize by impregnation.

Herein, a novel, more feasible synthesis approach will be presented using Hydrotalcite-based materials as precursor for supported Pd-X (X= Ga, Zn) IMCs. The class of Hydrotalcite-like compounds (HTlc) originate from the mineral Hydrotalcite $Mg_6Al_2(OH)_{16}CO_3 \cdot 4H_2O$ that is a hydroxycarbonate of Mg and Al with rhombohedral crystal structure.[19] In literature this mineral group is also referred to as layered double hydroxide (LDH). HTlc may be described by the general formula $[M1^{II}_{1-x}M2^{III}_{x}(OH)_2]^{x+}(A^{n-})_{x/n} \cdot mH_2O$ (0.2 < x < 0.4), where $M1^{II}$ and $M2^{III}$ are divalent and trivalent metals respectively and A^{n-} is an anion. Di- and trivalent cations are octahedrally coordinated by hydroxyl groups and build up a joint cationic lattice, that is isostructural to brucite $(Mg(OH)_2)$, presented in Figure 1- 1. By introducing trivalent cations into the brucite-like layers a positive charge is created. Inorganic and organic anions such as chlorides, nitrates, chromates or carboxylates are intercalated between the layers to maintain charge balance. Crystallization water is usually also found in the interlayer space.[20]
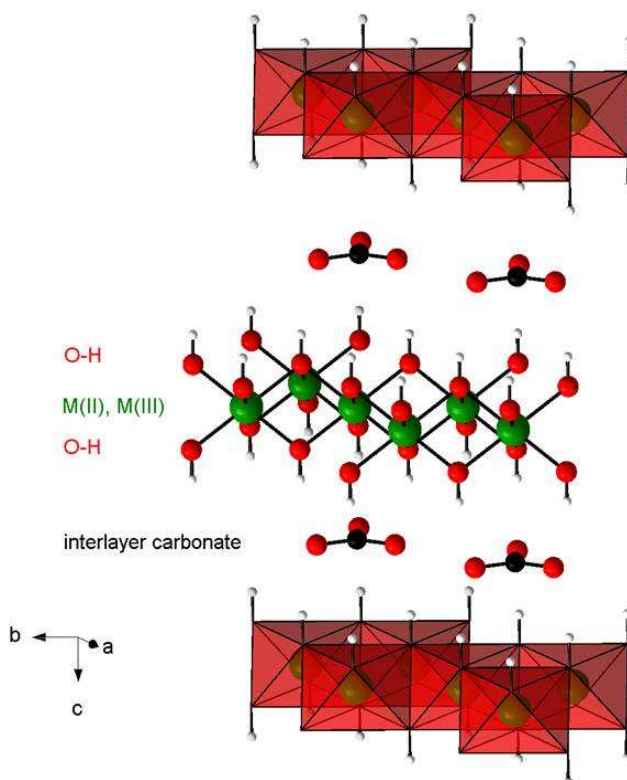
Figure 1- 1: Schematic representation of the Hydrotalcite-like structure (interlayer water not shown for clarity).

In general, the variety of metal ions is quite high and all cations with an ionic radius in the range of 0.5 - 0.8 Å are capable of HTlc formation, such as $M1^{II} = Mg^{2+}, Zn^{2+}, Mn^{2+}, Co^{2+}, Ni^{2+}, Cu^{2+}$ and $M2^{III} = Al^{3+}, Ga^{3+}, Fe^{3+}, Cr^{3+}$.[20, 21] A number of synthetic techniques have been successfully employed in preparation of HTlc and the most common preparation method is co-precipitation of the corresponding metal solutions. Co-precipitation allows for high reproducibility and scalability - important factors for commercial applications. The relevance of HTlc precursors for catalysis has been comprehensively reviewed by Cavani et al. [21] as well as by Forano et al. [19]. Both investigators pointed out the relevance of the homogeneous distribution of all metal cations inside the brucite layers in yielding well-dispersed, small and stable metal particles on mixed oxides support after calcination and reduction. HTlc already represent well established precursor systems [21] for bulk catalysts, applied e.g. in preparation of Ni-Al steam reforming [22] or Cu-Zn-Al methanol synthesis catalysts [23].

In our synthesis approach, ternary Hydrotalcite-like compounds were synthesized by co-precipitation. Variation of the $M1^{II}$ and $M2^{III}$ cations lead the preparation of three final compounds: two intermetallic and one metallic system. In case of the Pd-Ga intermetallic system Mg^{2+} was chosen as second divalent ion in order to build up the HTlc structure and not to interfere with redox chemistry, while for the Pd-Zn system Al^{3+} was selected as third, inert component for the formation of the HTlc structure. The pure metallic system consisted of Pd^{2+}, Mg^{2+}, Al^{3+} cations and no intermetallic formation is expected under the applied conditions. The HTlc mainly consisted of Mg^{2+} and Zn^{2+} ions, while these cations are only partially substituted by Pd^{2+} ions. The M^{2+}/M^{3+} ratio was set to 70:30 and the Pd content was varied from 0 - 2.5 mol%. The resulting interlayer space is   filled with carbonate ions and water.

In literature, synthesis of Pd-free MgGa HTlc [24, 25], ZnAl HTlc [26, 27] and MgAl HTlc [28, 29] materials has already been reported and phase-pure precursors could be obtained. However, there are only a few reports about Pd containing ternary HT systems obtained by co-precipitation.[30-32] More often, impregnation was used for the synthesis of noble metal containing HTl compounds.[33-37]

It is noted that Pd^{2+} prefers square planar coordination in aqueous solution, while incorporation into the HTlc lattice requires octahedral coordination. Furthermore, the large ionic radius (0.86 Å [38]) of Pd^{2+} exceeds the empirical limit of approximately 0.80 Å [20] for the incorporation into the HTlc. The incorporation of Pd into lattice of MgAl-HTl compounds was claimed by means of XRD. The existence single phase hydrotalcite-like precursor indicated that Pd^{2+} ion is isomorphously substituted for Mg in the Mg–Al brucite layer. Furthermore, the nominal composition was experimentally proven to be reflected in the HTlc including all Pd species.[30, 32] However, at low Pd loading (< 5 mol%) it is hard to confirm the incorporation of Pd by

means of XRD. The limit of incorporation depends on the Pd loading and precursor system, as it will be discussed in the second and third chapter.
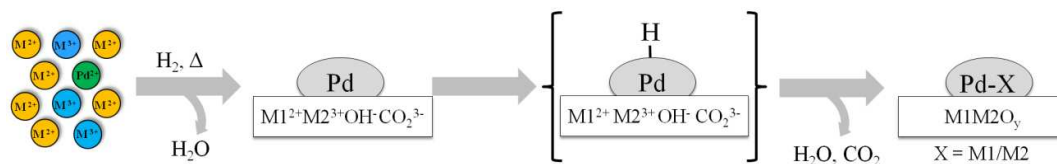
Figure 1- 2: Simplified scheme of the formation process of intermetallic nanoparticles based on Pd-M^{2+}-M^{3+} Hydrotalcite-like precursor.

A simplified reaction scheme starting from a Pd-based HTl compound and leading to the intermetallic compound is presented in Figure 1- 2. Upon heating in hydrogen small, metallic Pd particles are formed on the hydroxycarbonate matrix. Spilled-over atomic hydrogen is supposed to be formed on embedded Pd^0 particles under reductive conditions that interact with the surrounding Ga^{3+} or Zn^{2+}-oxide matrix and lead to the formation of the IMCs. Mg and Al as well as residual Ga and Zn will remain in their oxide state and form the support material. The formation of single phase nanoparticulate Pd-X IMCs is expected, due to the initial homogeneity of metals ions and small, reactive Pd^0/Pd-H particles that will be achieved on the basis of ternary HTl materials.

1.4.   Pd-Ga system

The nomenclature of Pd-Ga intermetallic compounds is quite controversial in literature, but according to the IUPAC recommendation 2005 [39] the intermetallic compounds will be named hereafter as Pd_xGa_y.

The phase diagram [40], shown in Figure 1- 3, emerged from the phase diagram of Massalski [41], who has summarized the first investigations published by Schubert et al.[42] and Khalaff et al.[43]. In addition, Wannek et al. [44] investigated the palladium-rich part (65 - 77 at.% Pd) of the phase diagram by means of powder x-ray diffraction and thermal analyses. These modifications were included in the Ga-Pd phase diagram below. It consists of nine intermetallic phases. It includes the 1:1 stoichiometric compound PdGa as well as gallium-rich $PdGa_5$ and Pd_3Ga_7 compounds. Palladium-rich compounds are for instance Pd_2Ga, Pd_2Ga_5 and $Pd_{13}Ga_5$ that were indentified in the binary system.
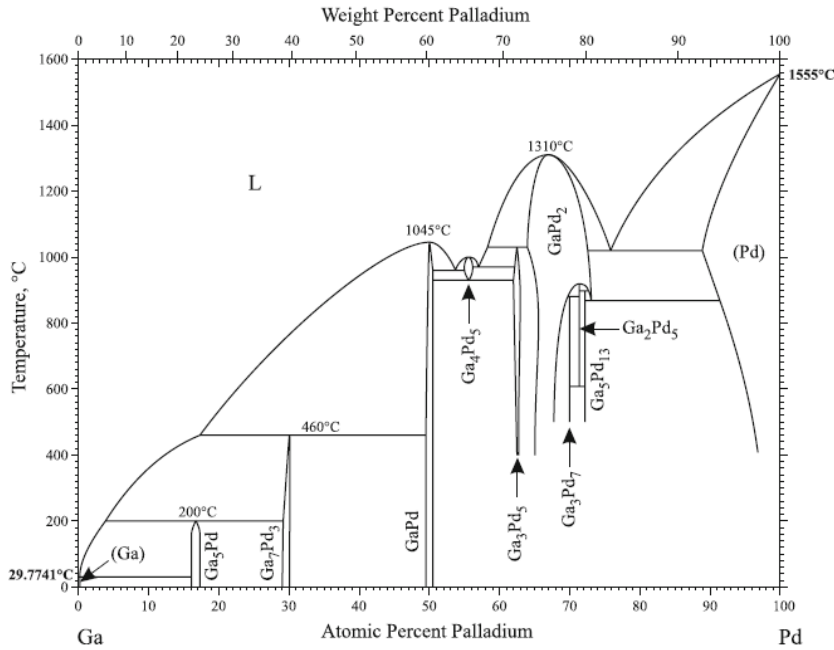
Figure 1- 3: Ga-Pd phase diagram according to Okamoto.[40]

1.5.   The Pd-Ga intermetallic compound Pd$_2$Ga

The thermodynamically most stable compound of the Pd-Ga system is Pd$_2$Ga. According to the Ga-Pd phase diagram, the Pd$_2$Ga compound displays an extraordinary broad homogeneity range at higher temperatures (T > 1173 K) that ranges from 27 - 36 Ga%. At low temperatures (< 773 K) the homogeneity range is limited to higher Ga content and varies from 33 - 35% Ga. Pd$_2$Ga exhibit orthorhombic structure with $a = 5.4829(8)$ Å, $b = 4.0560(4)$ Å, $c = 7.7863(8)$ Å [45] and crystallizes in Co$_2$Si type of structure.[46]

As shown in Figure 1- 4, two different kinds of Pd coordination spheres are obtained for the Pd$_2$Ga structure. Each Pd1 atom is surrounded by four Ga in a distorted tetrahedral coordination with distances varying between 2.54 Å and 2.56 Å. One additional Ga atom is quite far away at a distance of 2.96 Å. The environment of Pd2 atom is different: nonplanar trigonal coordination by three Ga atoms with d(Pd-Ga) = 2.56 Å – 2.62 Å and two other Ga atoms at a considerably longer distance of 2.84 Å. The coordination sphere of each palladium site is completed by eight Pd atoms with d(Pd-Pd) between 2.82 Å and 2.99 Å, thus increasing the coordination number of both Pd atoms to 13. In comparison to fcc Pd metal (2.75 Å) the interatomic distance is significantly increased.[45] All interatomic distances including the Ga atoms are given in Table 1- 1.

7

The formation of the nanoparticulate Pd_2Ga, obtained by reduction of Pd/Ga_2O_3 powder sample at 673 K, was first reported by Penner et al.[47] This result was in disagreement with earlier studies performed by Iwasa et al.[18], which obtained a phase mixture of Pd_5Ga_2 and $PdGa_5$ after reductive treatment.
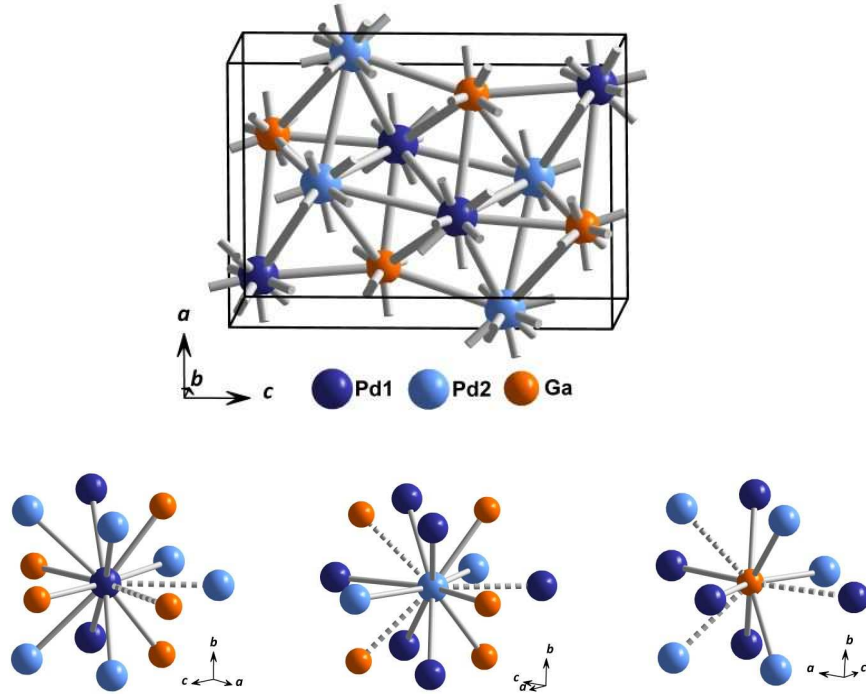
Figure 1- 4: Unit cell of Pd_2Ga and coordination sphere of Pd1, Pd2 and Ga.

Table 1- 1: Interatomic distances shorter than 3 Å for Pd1, Pd2 and Ga in the Pd_2Ga structure.

Pd1			d [Å]	Pd2			d [Å]	Ga1			d [Å]
	Ga	2x	2.54		Ga	2x	2.56		Pd1	2x	2.54
	Ga	1x	2.55		Ga	1x	2.62		Pd1	1x	2.55
	Ga	1x	2.56		Pd2	2x	2.81		Pd1	1x	2.56
	Pd2	2x	2.82		Pd1	2x	2.82		Pd2	2x	2.56
	Pd2	1x	2.85		Ga	2x	2.84		Pd2	1x	2.62
	Pd2	2x	2.90		Pd1	1x	2.85		Pd2	2x	2.85
	Pd1	2x	2.91		Pd1	2x	2.90		Pd1	1x	2.96
	Ga	1x	2.96		Pd1	1x	2.99					
	Pd2	1x	2.99								

1.6.   Pd-Zn phase system

In contrast to Pd-Ga system, the Pd-Zn phase diagram is less complex and reveals five bimetallic Pd_xZn_y structures according to Okamoto.[48] The Pd-Zn system, similarly to the Pd-Ga system, includes a Pd-rich phase with a Pd:Zn ratio of 2:1 that also crystallizes in CoSi-Type structure.[49] The most important and also thermodynamically stable phase is the tetragonal PdZn (here referred as ZnPd rt), which is usually obtained on supported Pd/ZnO powder catalyst after reductive treatment at elevated temperatures (473 - 573 K). It crystallizes in tetragonal (AuCu-type) L10 structure and its composition ranges from 37 - 56 at% Zn. Since its extraordinary high selectivity towards CO_2 in the steam reforming of methanol was reported in literature by Iwasa et al. [17], the PdZn system was intensively studied as model and real catalyst for this reaction (see section 1.8) by several groups.[50-54]
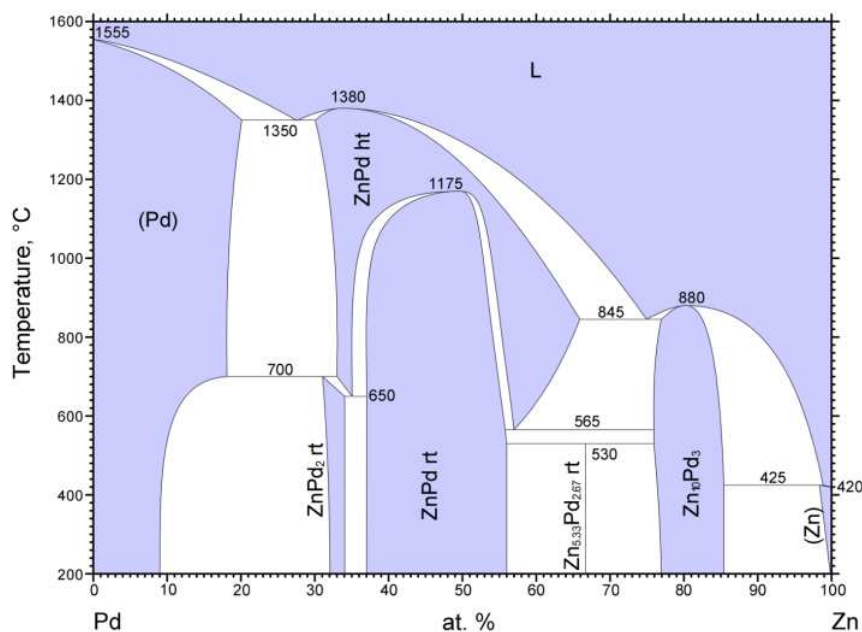
Figure 1- 5: Pd-Zn phase diagram according to Okamoto.[48]

1.7.   Pd-Ga IMCs as selective acetylene hydrogenation catalysts

The selective hydrogenation of acetylene to ethylene is an important industrial reaction in course of the production of polyethylene (50 Megatons/year) from ethylene.

$$C_2H_2 + H_2 \rightarrow C_2H_4 \qquad \Delta H = \text{-172 kJ/mol (298 K)} \ [55] \qquad (1)$$
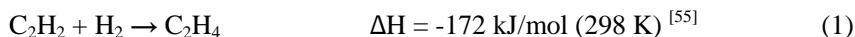
The ethylene stream produced by cracking of light alkanes has to be purified from acetylene, which would otherwise leads to poisoning of the polymerization catalyst. The acetylene concentration has to be lowered from usually around 1% to the low ppm range. The extent of complete hydrogenation of ethylene either originating from the stream or hydrogenation of acetylene to ethane (reaction 2) should be minimized to maximize the final polyethylene yield. The reaction is usually performed at 323 – 353 K.

$$C_2H_4 + H_2 \rightarrow C_2H_6 \qquad \text{(2) hydrogenation of ethylene to ethane}$$
$$n\ C_2H_2 + \tfrac{1}{2}\ n\ H_2 \rightarrow (C_2H_3)_n \qquad \text{(3) dimerization and oligomerization (n= 2, 3, 4, ..)}$$
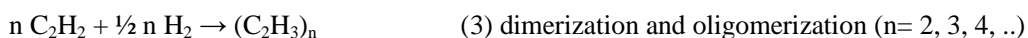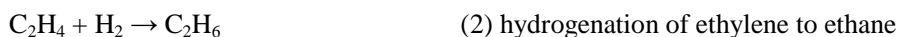
Dimerization and oligomerization lead to the formation of 1,3-butadiene (reaction 3, n=2) that can be further hydrogenated to C_4 hydrocarbons (1-butene, n-butane, cis- and trans-butene). C_4 species are suggested to be the precursor for C_6-hydrocarbons which are formed in small quantities and called green oil.[55, 56] Hydrocarbon deposits and hydrocarbon decomposition with subsequent formation of carbonaceous deposits on the catalyst surface lead to deactivation.[57, 58] It is well known that among the metals of group VIII, palladium dispersed on a support is highly active in the hydrogenation of acetylene, but only poorly selective, leading to the formation of ethane. The long-term stability of Pd is also reduced by the formation of other by products such as C_4 and higher hydrocarbons. The formation of C_4 species leads to strong deactivation which requires a frequent exchange or regeneration of the catalyst in the hydrogenation reactor. The changes to Pd catalyst during reaction and studies of the reaction mechanism have been recently summarized and reviewed by Borodziński and Bond.[59, 60]

Numerous examples and explanations as to how the selectivity and stability of Pd catalysts can be controlled are given in literature. The outstanding ability of Pd to dissociate and dissolve hydrogen is of fundamental importance in the selective hydrogenation process of triple to double bonds. It was experimentally demonstrated [61] and theoretically validated [62, 63] that dissolved hydrogen in the subsurface of Pd can diffuse to surface and further hydrogenate the adsorbates. As shown by Khan et al.[64] subsurface hydrogen was found to favor the total

hydrogenation of acetylene, whereas the presence of only surface H is more selective towards partial hydrogenation.[65]

The selective hydrogenation of acetylene proceeds via surface vinyl intermediates to ethylene, while over-hydrogenation of vinyl to ethylidene results in ethane or ethylidene. Isolation of surface Pd atoms is suggested to reduce the surface concentration and disfavor di-σ-adsorbed ethylene, which takes place on neighboring sites, forming ethylidyne and vinylidene species strongly bound to the surface.[66-68] These species may act as precursors for carbonaceous deposits and cause deactivation. On the other hand, these species play a role in separating the active sites and to reducing their size by surface blocking, which strongly affects the catalytic properties.[56, 59] Furthermore, the supply of hydrogen to the surface and subsurface will be decreased by the absence of neighboring sites, thus changing selectivity [69] as well as catalyst stability. It was shown by Teschner et al.[70] that under certain conditions alkyne fragmentation leads to formation of a Pd-C surface phase in pure Pd. This Pd-C surface leads to increased selectivity by hindered diffusion of hydrogen to bulk. Earlier work of Ziemicke et al.[71] have shown that Pd undergoes the formation of PdC_x solution by fragmentation of acetylene on Pd Black at temperatures 423 K. Using X-ray diffraction, a lattice expansion of approximately 3% was calculated for 15% incorporated carbon ($PdC_{0.15}$). In fact, the migration of carbon to the subsurface leads to formation of Pd-C subsurface that can prevent hydride formation.[72] It was proposed that the role of dissolved carbon and the Pd-C surface phase is to exclude bulk-dissolved hydrogen participating in the reaction. In-situ prompt gamma activation analysis (PGAA) was used to determine the hydrogen content in Pd during reaction. Indeed, the unselective hydrogenation proceeded via bulk hydrides, whereas selective hydrogenation was only possible after decoupling bulk properties from the surface events.

In addition to carbon formation and suppressed hydride formation, further specific surface modifications by deposition or poisoning to avoid overhydrogenation on Pd catalyst are reported in literature. For instance, it was shown that the addition of TiO_2 to Pd catalyst [73] leads to an increased selectivity to ethylene. TiO_2 was selected as potential promoter because it strongly interacts with Pd, particularly after high temperature treatment. This phenomenon is referred to as "the strong metal-support interaction" (SMSI) first proposed by Tauster [74, 75], has been observed with catalysts supported on reducible metal oxides. The SMSI phenomenon is explained by the decoration of the metal surface with partially reduced metal oxides [76, 77] or by an electron transfer between the support and the dispersed metals.[78, 79] Similar effects were also proposed for doping Pd/Al_2O_3 catalyst with potassium. It was suggested that the K-doped Al_2O_3 induces an electron transfer to Pd. Ethylene desorbs more readily before it can be further

hydrogenated to ethane. Changes in the electronic structure lead to different adsorptive properties that positively affect the selectivity.

Another concept considers geometric reasons for an improved selectivity. The currently industrially employed system, a Pd-Ag alloy show a superior selectivity [80] and stability in comparison to pure Pd catalyst. By alloying Pd with Ag the surface concentration of Pd is reduced, as well as the average size of the active ensembles. Consequently, different adsorptive and electronic properties are acquired. Studt et al. [81] developed scaling relations between different adsorption energies of reactants and intermediates and used that analysis to identify a descriptor for both catalytic activity and selectivity. Calculations of the potential energy diagram of the hydrogenation of acetylene over pure Pd and a PdAg catalyst have shown that the addition of Ag lowers the energy barrier of desorption of the intermediately formed ethylene with respect to the energy barrier of further hydrogenation to ethane and thus makes the catalyst more selective.[81] The same group also pointed out that similar effects are also present in case of other modifying atoms in the subsurface of Pd like carbon.[82]

Bulk Pd-Ga compounds benefit from geometric, electronic and adsorptive effects that increase the selectivity and long-term stability in the hydrogenation of acetylene. In case of the PdGa and Pd_3Ga_7 compound, the Pd atom posses none or only one Pd atom in the first coordination shell, while in Pd_2Ga the Pd-Pd coordination number is increased to 8. In comparison to *fcc* Pd metal (CN = 12) it is still lower. XPS measurements have shown that electronic properties of these compounds are different from those of metallic Pd. The Pd 3d binding energy is shifted to higher energies, which was explained by the filling of Pd d band due covalent interactions of Pd and Ga.[83, 84] The highest shift is observed for PdGa, followed by Pd_3Ga_7 and Pd_2Ga. Moreover the changes of electronic structure were experimentally shown with CO-IR adsorption on PdGa. One single adsorption band at 2047 cm^{-1} was detected indicating absence of multiple bonding and increased backdonation of from the Pd d-bands to the CO. Furthermore, the stability of PdGa and Pd_3Ga_7 was tested under in-situ conditions. Neither bulk nor the surface undergo any changes. During acetylene hydrogenation no hydride or carbon formation were observed by PGAA and in-situ XPS measurements, respectively.[13, 85] There are no studies of bulk Pd_2Ga under reaction conditions so far, but hydride formation can be excluded according to Kohlmann.[86] A very weak DSC signal and small unit cell increase of 1% at hydrogen pressures up to 39 MPa and temperatures up to 700 K were observed by in-situ DSC and ex-situ XRPD suggesting no significant hydrogen uptake. Based on these promising observations for the bulk materials it was worthwhile preparing and studying nanostructured Pd-Ga compounds.

1.8. Pd based IMCs in methanol synthesis and methanol steam reforming

Methanol is a widely used as a feedstock for the chemical industry and has potential to be applied directly in fuel cells, whereas hydrogen is considered as one of the most promising and clean energy carriers of the future. Methanol synthesis from CO_2 and its reverse reaction, methanol steam reforming is shown in equation 1. While MSR is not thermodynamically limited and is carried out at atmospheric pressure, methanol synthesis requires high pressures (30 - 100 bar) and lower operating temperatures due to unfavorable thermodynamics.[87] Reverse water gas shift (rWGS, reaction 2) is a side reaction to methanol synthesis and thus diminishes selectivity. In MSR, methanol decomposition (reaction 3) as well as rWGS are undesired side reactions and yield CO - a poison for fuel cell electrodes.

$$CO_2 + 3\ H_2 \leftrightarrow CH_3OH + H_2O \quad \Delta H_0 = \text{-49.8 kJ/mol} \qquad (1)$$

$$CO_2 + H_2 \leftrightarrow CO + H_2O \qquad \Delta H_0 = \text{+41.2 kJ/mol} \qquad (2)$$

$$CH_3OH \leftrightarrow CO + 2\ H_2 \qquad \Delta H_0 = \text{+91.0 kJ/mol} \qquad (3)$$

Both, methanol synthesis and steam reforming, are carried out at similar temperatures (523 - 603 K) on Cu/ZnO based catalysts. A major drawback of Cu-based catalyst is their poor long-term stability. Low Hüttig and Tammann temperatures, which reflect a relatively low melting point of Cu (1358 K), lead to thermal sintering at temperatures above 573 K. Additionally, deactivation of the Cu-based catalysts occurs by poisoning from impurities (sulfur, chlorine) and inhibition by co-products. While poisoning by contaminants of the feed gas and coking are normally the main reasons for catalyst deactivation in methanol decomposition and methanol steam reforming reactions, the main source of deactivation was stated to be the thermal sintering of the copper phase in methanol synthesis.[88]

Apart from the advanced Cu-based catalyst, Pd supported on Ga_2O_3 [47, 89, 90] and ZnO [17, 53, 91] were identified as efficient catalyst for methanol synthesis from CO_2 as well as for methanol steam reforming. Their high selectivity and activity is attributed to alloy formation that results from the partial reduction of the support. As already mentioned, several phases (Pd_2Ga, Pd_5Ga_2 and $PdGa_5$) were obtained in case of the Pd/Ga_2O_3 powder catalysts. Whereas for supported Pd/ZnO tetragonal bimetallic PdZn was identified as intermetallic phase. In contrast, other supported Pd catalyst, e.g. on SiO_2, Al_2O_3, were poorly selective in methanol synthesis [92] and methanol steam reforming [93]. In particular, the PdZn/ZnO system exhibits good selectivity and stability in MSR and therefore performs similarly to Cu based catalysts. XPS and UPS measurements have shown that the electronic structure of PdZn (1:1) resembles that of metallic

Cu [94, 95], which was confirmed by DFT calculations of the density of states.[96, 97] Neyman et al.[97] calculated the reaction barriers for methoxy dehydrogenation to CO and H_2 on Pd, PdZn and Cu surfaces. Similar barriers for dehydrogenation of intermediate formaldehyde to CO were found on Cu and PdZn, which are both remarkably higher than on Pd and therefore explain the high CO_2 selectivity.[81]

1.9. Aims of this work and thesis structure

The overall goal of this project is the synthesis of Pd-X (Ga, Zn) intermetallic nanoparticles by wet-chemical synthesis approach and characterization of their structural and catalytic properties. As already mentioned Hydrotalcite-like compounds were selected as precursor in order to achieve a close interaction between Pd and Ga/Zn that facilitates the IMC formation and yields homogenously distributed nanoparticles. Of particular interest is the catalytic activity in the selective hydrogenation of acetylene as well as methanol steam reforming (MSR) and methanol synthesis from CO_2. The following chapters will address several aspects:

·   Syntheses of well-defined Pd based Hydrotalcite-like precursors in order to obtain intermetallic Pd-X nanoparticles.
·   Characterization of the precursors in terms of phase-purity, Pd incorporation and textural properties.
·   Investigation of the phase formation process.
·   Analysis of the catalyst's physical and chemical properties including adsorption properties and structural stability compared to the monometallic catalyst.
·   Evaluation of the catalytic activity in the semi-hydrogenation of acetylene, methanol synthesis and methanol steam reforming reaction among the different systems.

These topics are described over three chapters with each chapter comprising an independent publication manuscript; containing: abstract, introduction, literature review, methods, results, discussion and conclusions. The structure is as follows:

Chapter Two - Intermetallic compound Pd_2Ga as a selective catalyst for the semi-hydrogenation of acetylene: From model to high performance systems - contains a comparative study of the obtained supported nanoparticulate Pd_2Ga compound with the bulk Pd_2Ga model catalyst. This chapter will include characterization data that explicitly confirms the formation of the nanocrystalline Pd_2Ga particle. The activity data of the preformed selective hydrogenation of acetylene is presented and compared to the intrinsic properties of the nanosized and bulk material in comparison to elemental Pd.

Chapter Three - Synthesis and dynamic surface processes of supported, catalytically active Pd_2Ga nanoparticles derived from ternary Hydrotalcite-like Precursors: A series of Pd-substituted MgGa Hydrotalcite-like compounds with different Pd loadings have been studied in terms of loading, phase formation and stability. The incorporation of Pd into the layered

structure of the precursor was proven. Furthermore, the activation process that was presented in Chapter 2 was investigated in more detail.

<u>Chapter Four - Synthesis, Characterization and Comparative Catalytic Study in Methanol Synthesis and Methanol Steam Reforming of Supported Pd_2Ga and PdZn Intermetallic Nanoparticles:</u> The successfully applied synthesis procedure of Chapters 2 & 3 was adopted to prepare intermetallic Pd-Zn compound as well as pure Pd reference system. The extent of Pd incorporation for the different samples was studied as well the IMC formation processes. The adsorptive properties, the activity of the intermetallic and monometallic catalysts were compared in the methanol synthesis (from CO_2) and methanol steam reforming reaction.

<u>Chapter Five - Summary and Conclusions</u> gives a brief synopsis of the combined findings and the conclusions that can be drawn from this work.

1.10.   References

[1]   Sauthoff, *Intermetallics*, Wiley-VCH Verlag GmbH Weinheim, **1995**.
[2]   G. E. R. Schulze, *Metallphysik*, Springer Verlag Wien New York, **1967**.
[3]   J. Westbrook, *Metallurgical and Materials Transactions A* **1977**, *8*, 1327-1360.
[4]   T. Yamamoto, in *The Development of Sendust and Other Ferromagnetic Alloys* (Ed.: T. Yamamoto), Committee of Academic Achievements, Chiba, **1980**, pp. 1-6.
[5]   M. B. Bever, in *Encyclopedia of Materials Science and Engineering* (Ed.: G. W. Brock), Pergamon, Oxford, **1986**, pp. 2679 -2682.
[6]   D. B. Miracle, *Acta Metallurgica et Materialia* **1993**, *41*, 649-684.
[7]   K. N. Campbell, B. K. Campbell, *Chemical Reviews* **1942**, *31*, 77-175.
[8]   A. J. Smith, D. L. Trimm, *Annual Review of Materials Research* **2005**, *35*, 127-142.
[9]   R. Schröter, *Angewandte Chemie* **1941**, *54*, 229-234.
[10]   C. N. Thanh, B. Didillon, P. Sarrazin, C. Cameron, **2000**.
[11]   K. Kovnir, M. Armbrüster, D. Teschner, T. V. Venkov, F. C. Jentoft, A. Knop-Gericke, Y. Grin, R. Schlögl, *Science and Technology of Advanced Materials* **2007**, *8*, 420-427.
[12]   J. Osswald, R. Giedigkeit, R. E. Jentoft, M. Armbrüster, F. Girgsdies, K. Kovnir, T. Ressler, Y. Grin, R. Schlögl, *Journal of Catalysis* **2008**, *258*, 210-218.
[13]   J. Osswald, K. Kovnir, M. Armbrüster, R. Giedigkeit, R. E. Jentoft, U. Wild, Y. Grin, R. Schlögl, *Journal of Catalysis* **2008**, *258*, 219-227.
[14]   K. Kovnir, J. Osswald, M. Armbruster, D. Teschner, G. Weinberg, U. Wild, A. Knop-Gericke, T. Ressler, Y. Grin, R. Schlogl, *Journal of Catalysis* **2009**, *264*, 93-103.
[15]   M. Armbrüster, G. Wowsnick, M. Friedrich, M. Heggen, R. Cardoso-Gil, *Journal of the American Chemical Society* **2011**, *133*, 9112-9118.
[16]   L. Shao, W. Zhang, M. Armbrüster, D. Teschner, F. Girgsdies, B. Zhang, O. Timpe, M. Friedrich, R. Schlögl, D. S. Su, *Angewandte Chemie International Edition* **2011**, *50*, 10231-10235.
[17]   N. Iwasa, S. Masuda, N. Ogawa, N. Takezawa, *Applied Catalysis A: General* **1995**, *125*, 145-157.
[18]   N. Iwasa, T. Mayanagi, N. Ogawa, K. Sakata, N. Takezawa, *Catalysis Letters* **1998**, *54*, 119-123.
[19]   C. Forano, T. Hibino, F. Leroux, C. Taviot-Gueho, in *Handbook of Clay Science* (Eds.: F. Bergaya, B. K. G. Theng, G. Lagaly), Elsevier, **2006**, pp. 1021-1095.
[20]   A. De Roy, *Molecular Crystals and Liquid Crystals Science and Technology. Section A. Molecular Crystals and Liquid Crystals* **1998**, *311*, 173 -193.
[21]   F. Cavani, F. Trifirò, A. Vaccari, *Catalysis Today* **1991**, *11*, 173-301.
[22]   F. Basile, A. Vaccari, in *Layered Double Hydroxides-Present and Future* (Ed.: V. Rives), Nova Science Publishers Inc, New York, **2001**.
[23]   M. Behrens, I. Kasatkin, S. Kűhl, G. Weinberg, *Chemistry of Materials* **2009**, *22*, 386-397.
[24]   E. López-Salinas, M. García-Sánchez, M. L. Ramón-García, I. Schifter, *Journal of Porous Materials* **1996**, *3*, 169-174.
[25]   M. A. Aramendia, Y. Aviles, V. Borau, J. M. Luque, J. M. Marinas, J. R. Ruiz, F. J. Urbano, *Journal of Materials Chemistry* **1999**, *9*, 1603-1607.
[26]   F. Thevenot, R. Szymanski, P. Chaumette, *Clays and Clay Minerals* **1989**, *37*, 396-402.
[27]   J. T. Kloprogge, L. Hickey, R. L. Frost, *Journal of Solid State Chemistry* **2004**, *177*, 4047-4057.
[28]   P. Kuśtrowski, L. Chmielarz, E. Bożek, M. Sawalha, F. Roessner, *Materials Research Bulletin* **2004**, *39*, 263-281.
[29]   M. R. Othman, N. M. Rasid, W. J. N. Fernando, *Microporous and Mesoporous Materials* **2006**, *93*, 23-28.

[30]   F. Basile, G. Fornasari, M. Gazzano, A. Vaccari, *Applied Clay Science* **2000**, *16*, 185-200.
[31]   A. Morato, C. Alonso, F. Medina, Y. Cesteros, P. Salagre, J. E. Sueiras, D. Tichit, B. Coq, *Applied Catalysis B: Environmental* **2001**, *32*, 167-179.
[32]   N. N. Das, S. C. Srivastava, *Bulletin of Materials Science* **2002**, *25*, 283-289.
[33]   S. Narayanan, K. Krishna, *Applied Catalysis A: General* **1998**, *174*, 221-229.
[34]   F. Prinetto, M. Manzoli, G. Ghiotti, M. D. M. Ortiz, D. Tichit, B. Coq, *Journal of Catalysis* **2004**, *222*, 238-249.
[35]   A. H. Padmasri, A. Venugopal, V. S. Kumar, V. Shashikala, B. M. Nagaraja, P. Seetharamulu, B. Sreedhar, B. D. Raju, P. K. Rao, K. S. R. Rao, *Journal of Molecular Catalysis a-Chemical* **2004**, *223*, 329-337.
[36]   A. A. Nikolopoulos, B. W. L. Jang, J. J. Spivey, *Applied Catalysis A: General* **2005**, *296*, 128-136.
[37]   B. T. Meshesha, R. J. Chimentão, A. M. Segarra, J. Llorca, F. Medina, B. Coq, J. E. Sueiras, *Applied Catalysis B: Environmental* **2011**, *105*, 361-372.
[38]   R. Shannon, *Acta Crystallographica Section A* **1976**, *32*, 751-767.
[39]   N. G. Connelly, T. Damhus, R. M. Hartshorn, A. T. Hutton, *Nomenclature of Inorganic Chemistry -*
IUPAC Recommendations 2005, The Royal Society of Chemistry: Cambridge, **2005**.
[40]   H. Okamoto, *Journal of Phase Equilibria and Diffusion* **2008**, *29*, 466-467.
[41]   T. B. Massalski, *Binary Alloy Phase Diagrams*, 2 ed., ASM international, Ohio, USA, **1990**.
[42]   K. Schubert, H. Breimer, W. Burkhardt, E. Grunzel, R. Haufler, H. L. Lukas, H. Vetter, J. Wegst, M. Wilkens, *Naturwissenshaften* **1959**, *44*, 229-230.
[43]   K. Khalaff, K. Schubert, *Journal of the Less Common Metals* **1974**, *37*, 129-140.
[44]   C. Wannek, B. Harbrecht, *Journal of Alloys and Compounds* **2001**, *316*, 99-106.
[45]   K. Kovnir, M. Schmidt, C. Waurisch, M. Armbrüster, Y. Prots, Y. Grin, *Zeitschrift für Kristallographie NCS* **2008**, *223*, 7-8.
[46]   S. Geller, V. M. Wolontis, *Acta Crystallographica* **1955**, *8*, 83-87.
[47]   S. Penner, H. Lorenz, W. Jochum, M. Stöger-Pollach, D. Wang, C. Rameshan, B. Klötzer, *Applied Catalysis A: General* **2009**, *358*, 193-202.
[48]   H. Okamoto, in *Binary Alloy Phase Diagrams*, 2nd ed. (Ed.: T. B. Massalski), **1990**, pp. 3068-3070.
[49]   H. H. Stadelmaier, W. K. Hardy, *Zeitschrift Metallkd* **1961**, *52* 391-396.
[50]   S. Penner, B. Jenewein, H. Gabasch, B. Klötzer, D. Wang, A. Knop-Gericke, R. Schlögl, K. Hayek, *Journal of Catalysis* **2006**, *241*, 14-19.
[51]   C. Rameshan, W. Stadlmayr, C. Weilach, S. Penner, H. Lorenz, M. Hävecker, R. Blume, T. Rocha, D. Teschner, A. Knop-Gericke, R. Schlögl, N. Memmel, D. Zemlyanov, G. Rupprechter, B. Klötzer, *Angewandte Chemie International Edition* **2010**, *49*, 3224-3227.
[52]   B. Halevi, E. J. Peterson, A. DeLaRiva, E. Jeroro, V. M. Lebarbier, Y. Wang, J. M. Vohs, B. Kiefer, E. Kunkes, M. Havecker, M. Behrens, R. Schlögl, A. K. Datye, *The Journal of Physical Chemistry C* **2010**, *114*, 17181-17190.
[53]   K. Föttinger, J. A. van Bokhoven, M. Nachtegaal, G. n. Rupprechter, *The Journal of Physical Chemistry Letters* **2011**, *2*, 428-433.
[54]   M. W. Tew, H. Emerich, J. A. van Bokhoven, *The Journal of Physical Chemistry C* **2011**, *115*, 8457-8465.
[55]   A. N. R. Bos, K. R. Westerterp, *Chemical Engineering and Processing: Process Intensification* **1993**, *32*, 1-7.
[56]   Á. Molnár, A. Sárkány, M. Varga, *Journal of Molecular Catalysis A: Chemical* **2001**, *173*, 185-221.
[57]   A. Sárkány, L. Guczi, A. H. Weiss, *Applied Catalysis* **1984**, *10*, 369-388.
[58]   S. Asplund, *Journal of Catalysis* **1996**, *158*, 267-278.

[59]   A. Borodziński, G. C. Bond, *Catalysis Reviews: Science and Engineering* **2006**, *48*, 91 - 144.

[60]   A. Borodziński, G. C. Bond, *Catalysis Reviews: Science and Engineering* **2008**, *50*, 379 - 469.

[61]   A. D. Johnson, S. P. Daley, A. L. Utz, S. T. Ceyer, *Science* **1992**, *257*, 223-225.

[62]   A. Michaelides, P. Hu, A. Alavi, *The Journal of Chemical Physics* **1999**, *111*, 1343-1345.

[63]   V. Ledentu, W. Dong, P. Sautet, *Journal of the American Chemical Society* **2000**, *122*, 1796-1801.

[64]   N. A. Khan, A. Uhl, S. Shaikhutdinov, H. J. Freund, *Surface Science* **2006**, *600*, 1849-1853.

[65]   N. Khan, S. Shaikhutdinov, H. Freund, *Catalysis Letters* **2006**, *108*, 159-164.

[66]   A. M. Doyle, S. K. Shaikhutdinov, H. J. Freund, *Journal of Catalysis* **2004**, *223*, 444-453.

[67]   S. Shaikhutdinov, M. Heemeier, M. Bäumer, T. Lear, D. Lennon, R. J. Oldman, S. D. Jackson, H. J. Freund, *Journal of Catalysis* **2001**, *200*, 330-339.

[68]   S. K. Shaikhutdinov, M. Frank, M. Bäumer, S. D. Jackson, R. J. Oldman, J. C. Hemminger, H. J. Freund, *Catalysis Letters* **2002**, *80*, 115-122.

[69]   G. C. Bond, P. B. Wells, *Journal of Catalysis* **1966**, *5*, 65-73.

[70]   D. Teschner, E. Vass, M. Hävecker, S. Zafeiratos, P. Schnörch, H. Sauer, A. Knop-Gericke, R. Schlögl, M. Chamam, A. Wootsch, A. S. Canning, J. J. Gamman, S. D. Jackson, J. McGregor, L. F. Gladden, *Journal of Catalysis* **2006**, *242*, 26-37.

[71]   S. B. Ziemecki, G. A. Jones, D. G. Swartzfager, R. L. Harlow, J. Faber, *Journal of the American Chemical Society* **1985**, *107*, 4547-4548.

[72]   D. Teschner, J. Borsodi, A. Wootsch, Z. Révay, M. Hävecker, A. Knop-Gericke, S. D. Jackson, R. Schlögl, *Science* **2008**, *320*, 86-89.

[73]   J. H. Kang, E. W. Shin, W. J. Kim, J. D. Park, S. H. Moon, *Journal of Catalysis* **2002**, *208*, 310-320.

[74]   S. J. Tauster, S. C. Fung, R. L. Garten, *Journal of the American Chemical Society* **1978**, *100*, 170-175.

[75]   S. J. Tauster, *Accounts of Chemical Research* **1987**, *20*, 389-394.

[76]   J. Santos, J. Phillips, J. A. Dumesic, *Journal of Catalysis* **1983**, *81*, 147-167.

[77]   H. R. Sadeghi, V. E. Henrich, *Journal of Catalysis* **1984**, *87*, 279-282.

[78]   P. Chou, M. A. Vannice, *Journal of Catalysis* **1987**, *104*, 1-16.

[79]   J. M. Herrmann, M. Gravelle-Rumeau-Maillot, P. C. Gravelle, *Journal of Catalysis* **1987**, *104*, 136-146.

[80]   G. C. Bond, G. Webb, P. B. Wells, J. M. Winterbottom, *Journal of Catalysis* **1962**, *1*, 74-84.

[81]   F. Studt, F. Abild-Pedersen, T. Bligaard, R. Z. Sørensen, C. H. Christensen, J. K. Nørskov, *Science* **2008**, *320*, 1320-1322.

[82]   F. Studt, F. Abild-Pedersen, T. Bligaard, R. Z. Sorensen, C. H. Christensen, J. K. Norskov, *Angewandte Chemie-International Edition* **2008**, *47*, 9299-9302.

[83]   K. Kovnir, D. Teschner, M. Armbrüster, P. Schnörch, M. Hävecker, A. Knop-Gericke, Y. Grin, R. Schlögl, *Bessy Highlights 2007* **2008**, 22-23.

[84]   L. Shao, W. Zhang, M. Armbrüster, D. Teschner, F. Girgsdies, B. Zhang, O. Timpe, M. Friedrich, R. Schlögl, D. S. Su, *Angewandte Chemie International Edition* **2011**, n/a-n/a.

[85]   J. Osswald, PhD thesis, Technical University Berlin (Berlin), **2006**.

[86]   H. Kohlmann, *Journal of Solid State Chemistry* **2010**, *183*, 367-372.

[87]   R. Schögl, *Energy Storage Materials*, Walter de Gruyter, Berlin, **2012**.

[88]   M. V. Twigg, M. S. Spencer, *Topics in Catalysis* **2003**, *22*, 191-203.

[89]   H. Lorenz, S. Penner, W. Jochum, C. Rameshan, B. Klötzer, *Applied Catalysis A: General* **2009**, *358*, 203-210.

[90]   A. Haghofer, K. Föttinger, F. Girgsdies, D. Teschner, A. Knop-Gericke, R. Schlögl, G. Rupprechter, *Journal of Catalysis* **2012**, *286*, 13-21.

[91]   T. Conant, A. M. Karim, V. Lebarbier, Y. Wang, F. Girgsdies, R. Schlögl, A. Datye, *Journal of Catalysis* **2008**, *257*, 64-70.

[92]   T. Fujitani, M. Saito, Y. Kanai, T. Watanabe, J. Nakamura, T. Uchijima, *Applied Catalysis A: General* **1995**, *125*, L199-L202.

[93]   N. Takezawa, N. Iwasa, *Catalysis Today* **1997**, *36*, 45-56.

[94]   A. P. Tsai, K. Satoshi, I. Yasushi, *Journal of the Physical Society of Japan* **2004**, *12*, 3270.

[95]   A. Bayer, K. Flechtner, R. Denecke, H. P. Steinruck, K. M. Neyman, N. Rosch, *Surface Science* **2006**, *600*, 78-94.

[96]   Z. X. Chen, K. M. Neyman, A. B. Gordienko, N. Rosch, *Physical Review B* **2003**, *68*.

[97]   K. M. Neyman, K. H. Lim, Z. X. Chen, L. V. Moskaleva, A. Bayer, A. Reindl, D. Borgmann, R. Denecke, H. P. Steinruck, N. Rosch, *Physical Chemistry Chemical Physics* **2007**, *9*, 3470-3482.

Chapter 2: Intermetallic Compound Pd$_2$Ga as a Selective Catalyst for the Semi-Hydrogenation of Acetylene: From Model to High performance Catalyst

Authors: Antje Ota, Marc Armbrüster, Malte Behrens, Dirk Rosenthal, Matthias Friedrich, Igor Kasatkin, Frank Girgsdies, Wei Zhang, Ronald Wagner, and Robert Schlögl.

Abstract

A novel nanostructured Pd$_2$Ga intermetallic catalyst is presented and compared to elemental Pd and a macroscopic bulk Pd$_2$Ga material concerning physical and chemical properties. The new material was prepared by controlled coprecipitation from a single phase layered double hydroxide precursor or hydrotalcite-like compound, of the composition Pd$_{0.025}$Mg$_{0.675}$Ga$_{0.3}$(OH)$_2$(CO$_3$)$_{0.15}$ · mH$_2$O. Upon thermal reduction in hydrogen, bimetallic nanoparticles of an average size less than 10 nm and a porous MgO/MgGa$_2$O$_4$ support were formed. HRTEM images confirmed the presence of the intermetallic compound Pd$_2$Ga and are corroborated by XPS investigations which revealed an interaction between Pd and Ga. Due to the relatively high dispersion of the intermetallic compound, the catalytic activity of the sample in the semihydrogenation of acetylene was more than 5000 times higher than observed for a bulk Pd$_2$Ga model catalyst. Interestingly, the high selectivity of the model catalyst toward the semihydrogenated product of 74% was only slightly lowered to 70% for the nanostructured catalyst, while an elemental Pd reference catalyst showed only a selectivity of around 20% under these testing conditions. This result indicates the structural integrity of the intermetallic compound and the absence of elemental Pd in the nanosized particles. Thus, this work serves as an example of how the unique properties of an intermetallic compound, well-studied as a model catalyst, can be made accessible as real high-performing material allowing establishment of structure-performance relationships and other application-related investigations. The general synthesis approach is assumed to be applicable to several Pd-X intermetallic catalysts, with X being elements forming hydrotalcite-like precursors in their ionic form.

2.1 Introduction

Pd is a highly active noble metal catalyst for hydrogenation reactions, [1, 2] e.g., the hydrogenation of acetylene. Among the Pd-based catalysts, Pd-Ag alloy catalysts show a higher selectivity toward the semi-hydrogenated product, ethylene, than pure Pd catalysts, which favor total hydrogenation to ethane, and are the currently industrially employed system for this process.[3] The modification of the electronic, adsorptive, and catalytic properties of Pd-based catalysts by the presence of a second species has recently received considerable attention. Calculations of the potential energy diagram for the hydrogenation of acetylene over pure Pd and Pd-Ag have shown that the addition of Ag lowers the energy barrier of desorption of the intermediately formed ethylene with respect to the energy barrier of further hydrogenation to ethane and thus makes the catalyst more selective.[4] Similar effects are also predicted for other modifying atoms in the subsurface of Pd.[5] It was shown experimentally that conditions of selective alkyne hydrogenation can also be found if pure Pd metal is used as starting material. In situ investigations have shown that under these conditions in fact a Pd-C phase is in operation,[6] which was formed by fragmentation of the reactant molecule and migration of carbon into the subsurface.[7] Among the Pd-X materials investigated as hydrogenation catalysts, bulk Pd-Ga intermetallic compounds (IMCs) have shown extraordinarily high selectivities and stability in the semi-hydrogenation of acetylene.[8] IMCs are single-phase materials which consist of two or more metallic elements. In contrast to alloys, they adopt an ordered crystal structure different from those of the constituting metals themselves. [8, 9] Thus, also their chemical properties may differ substantially, and they should be considered as a class of materials in their own right, requiring an independent physicochemical characterization. This has recently been demonstrated for the structurally ordered IMCs PdGa and Pd$_3$Ga$_7$.[10, 11] The in situ stability of these IMCs in reaction atmosphere and the important suppression of hydride formation were attributed to the presence of an ordered and partially covalent bonding network between Pd and Ga in contrast to statistically arranged substitutional alloys. Unfortunately, as for most other Pd-X systems, homogeneous and nanostructured versions of Pd-Ga IMCs allowing a transfer of theoretically predicted properties or of the results already confirmed for macroscopic model systems to "real" catalysts are hard to obtain.

The general procedure to synthesize Pd-Ga IMCs is by melting the appropriate amounts of the elements followed by annealing at high temperatures in inert atmosphere. This direct reaction leads to well-defined and phase-pure model materials, which are very useful to study the intrinsic catalytic properties of IMCs. The material obtained is in thermodynamic equilibrium, easing the reproducible synthesis. Top-down approaches, e.g., milling or etching of bulk intermetallic compounds,[12] lead to an increase in surface area but go hand in hand with a partial

destruction of the IMC crystal structure, not only being detrimental for the catalytic selectivity but also complicating the establishment of structure-performance relationships. Thus, to check if the unique structural and catalytic properties of bulk IMCs can be maintained or even extrapolated from the world of model catalysis to real systems, i.e., over several orders of magnitude in particle size, bottom-up approaches are necessary. One possibility to prepare supported and dispersed IMCs is by reaction between noble metal and the oxide support. An example is the formation of Pd-Ga intermetallic compounds by reductive treatment at elevated temperatures of Pd/Ga$_2$O$_3$.[13-15] Single-phase and nanosized Pd-Ga intermetallic compounds can be synthesized by co-reduction of GaCl$_3$ and Pd(acac)$_2$ in THF by Superhydride.[16] This synthesis leads to very small particles of the intermetallic compounds and surface areas of more than 2 m²/g. Applied as catalysts, these materials were shown to keep the high intrinsic selectivity of the Pd-Ga IMCs, while the specific activity is increased by a factor of up to 32 000. However, this method of preparation necessitates expensive reactants as well as inert atmosphere during the synthesis process, making it ineligible for industrial application. Herein, we present a novel nanosized IMC catalyst prepared by a more feasible synthetic approach using a hydrotalcite-based material as precursor for supported Pd-Ga IMCs and address the question if the unique structural and electronic properties found in this system also persist in the form of nanoparticles enabling interesting catalytic performance. Hydrotalcite-like compounds (HTlc) are easily accessible by coprecipitation from aqueous solutions and represent well-established precursor systems [17] for bulk catalysts, applied, e.g., in preparation of Ni-Al steam reforming [18] or Cu-Zn-Al methanol synthesis catalysts.[19] HTlc exhibit the general composition (M1$_{II}$,M2$_{II}$)$_{1-x}$-M3$_{III\ x}$(OH)$_2$(CO$_3$)$_{x/2}$ ·mH$_2$O (0.25 < x < 0.33) and a layered structure, in which all metal cations are uniformly distributed in slabs of edge-sharing MO$_6$ octahedra. HTlc precursors thus present well-defined and homogeneous starting materials for the preparation of supported IMCs.

The final Pd$_2$Ga/MgO/MgGa$_2$O$_4$ catalyst obtained by the HTlc precursor approach described above was characterized using nitrogen physisorption, XRD, HRTEM, and XPS. To investigate possible particle size effects in this system, the structural, electronic, and catalytic properties in the semi-hydrogenation of acetylene are compared to those of elemental Pd and those of the unsupported bulk counterpart, a Pd$_2$Ga catalyst prepared by direct reaction of the elements as described in refs 10 and 11.

2.2 Experimental Section

2.2.1 Synthesis Procedures

The PdMgGa HTlc precursor (atomic ratio 2.5:67.5:30) was synthesized by controlled coprecipitation at pH = 8.5 and 55 °C by cofeeding appropriate amounts of mixed aqueous metal nitrate ($[Pd^{2+}] + [Mg^{2+}] + [Ga^{3+}] = 0.2$ M) and 0.345 M sodium carbonate solution as the precipitating agent. Both solutions were added simultaneously dropwise into a 2 L precipitation reactor (Mettler-Toledo LabMax). The nitrate solution was automatically pumped with a constant dosing rate, and the basic solution was added to maintain a constant pH of 8.5. After completion of addition, the mixture was stirred for 1 h at 55 °C. The precipitate was filtered and washed twice with warm deionized water (55 °C) to remove all nitrate and sodium ions. The obtained conductivity of the filtrate was lower than 0.5 mS/cm, and no sodium contamination could be detected by EDX. The solid was dried for 12 h at 80 °C in air. The precursor was reduced in 5% H$_2$ in argon at 550 °C to obtain the supported Pd-Ga intermetallic compound. The heating rate was 2 °C/min, and the final temperature was kept for 4 h. A second catalyst, consisting of bulk Pd$_2$Ga, was prepared for reference purposes by melting Pd (ChemPur 99.95%) and Ga (ChemPur 99.99%) in a 2:1 molar ratio in glassy carbon crucibles under an argon atmosphere in a high-frequency induction furnace. After the exothermic reaction of the metals, the product was cooled to ambient temperature, enclosed in an evacuated quartz glass ampule, and annealed at 900 °C for 100 h. Subsequently, the samples were quenched in water, and the phase purity was verified by transmission powder X-ray diffraction.

2.2.2 Characterization Techniques

Electron Microscopy:

For TEM investigations, a Philips CM200FEG microscope operated at 200 kV and equipped with a field emission gun, the Gatan imaging filter, and energy-dispersive X-ray (EDX) analyzer was used. The coefficient of spherical aberration was $C_s = 1.35$ mm, and the information limit was better than 0.18 nm. High resolution images with a pixel size of 0.016 nm were taken at the magnification of 1 083 000 with a CCD camera, and selected areas were processed to obtain the power spectra (square of the Fourier transform of the image), which were used for measuring interplanar distances (±0.5%) and angles (±0.5°) for phase identification. Scanning electron microscopy was employed for investigation of particle morphology and metal distribution of the HTlc precursor using a Hitachi S-4800 (FEG) system.

X-ray Diffraction:

XRD measurements of the Pd$_2$Ga sample obtained by the direct reaction between the metals were performed on an image plate Guinier camera (G670, Huber, Cu Kα_1 radiation, $\lambda = 1.54056$ Å, quartz monochromator, $3° \leq 2\theta \leq 100°$) in transmission mode. For the measurements, the finely powdered sample was mounted with the aid of Vaseline on a 3 μm Kapton foil. For the ex-HTlc samples the measurements were performed in Bragg-Brentano reflection geometry on a Bruker AXS D8 Advance diffractometer equipped with a secondary graphite monochromator (Cu Kα radiation) and scintillation detector. The sample powder was filled into the flat circular recess of a sample holder which was sealed with an airtight X-ray transparent dome to avoid prolonged air contact. XRD patterns of the HTlc precursor and its decomposition products were recorded on a STOE Stadi P diffractometer in transmission geometry using Cu Kα1 radiation, a primary Ge monochromator, and a 3° linear position sensitive detector.

X-ray Photoemission Spectroscopy:

All XP spectra were recorded with fixed analyzer transmission at room temperature, using non-monochromatized Mg Kα radiation at a pass energy of 20 eV leading to fwhm < 1.1 eV of Ag 3d$_{5/2}$. The binding energy scale of the system was calibrated using Au 4f$_{7/2}$) 84.0 eV and Cu 2p$_{3/2}$) 932.7 eV from foil samples. The angle between the sample normal and the analyzer was 30° and between the X-ray gun and the sample normal 54°. Deconvolution of the spectra was conducted by 70/30 G-Lorentz product functions after subtraction of a Shirley background. To avoid contamination or oxidations on the surface, the catalyst pellet was prereduced at 550 °C in diluted hydrogen (5%) for 4 h to have the as-synthesized state prior to the measurement and transferred to the XPS chamber without air contact.

Specific Surface Area Determination:

Specific surface areas of the precursors and the reduced samples were determined by N$_2$ physisorption in an Autosorb-1C setup (Quantachrome) using the BET method. Prior to the measurements, 30 mg of the samples was degassed for 2 h at 80 °C for the precursors and at 150 °C for the reduced samples, respectively.

Chemical Analysis:

About 5 mg of sample was exactly weighed and dissolved in 2 mL of aqua regia. The solutions were transferred to and filled up 50 mL volumetric flasks. The content of the metals was determined with ICP-OES (Vista RL, Varian) after matrix-matched calibration.

2.2.3 Catalytic Measurements

Catalytic investigations were performed in a quartz glass plug flow reactor with an inner diameter of 7 mm. The catalyst bed was supported by a quartz glass frit and consisted of the

stated sample amounts diluted in 150 mg of catalytically inert boron nitride (hexagonal, 99.5%, 325 mesh, Aldrich) to improve the flow characteristics. No pressure drop was observed at a total gas flow of 30 mL/min. In the case of the directly synthesized Pd$_2$Ga, the samples were comminuted in an agate mortar in inert atmosphere prior to the catalytic measurements resulting in particle sizes below 20 μm. In the case of the HTlc approach, the precursor (0.4-1 μm) was reduced in situ (5% H$_2$, 4 h, 500 °C). The reactant mixture consisted of 0.5% C$_2$H$_2$ (premixed 5% C$_2$H$_2$, 99.6% in He, 99.996%), 5% H$_2$ (99.999%), and 50% C$_2$H$_4$ (99.95%) in helium (99.999%). All gases except ethylene (Westfalen Gas) were obtained by Praxair. Gases were mixed using Bronkhorst mass flow controllers. Reactant and product composition were analyzed with a Varian CP 4900 micro gas chromatograph. Conversion of acetylene and selectivity to ethylene were calculated as

$$X_{C_2H_2} = \frac{c_{feed} - c_x}{c_{feed}} \times 100\%$$

and

$$S_{C_2H_4} = \frac{c_{C_2H_4}}{c_{C_2H_4} + c_{C_2H_6} + 2c_{C_4H_x}} = \frac{X_{C_2H_2}}{X_{C_2H_2} + c_{C_2H_6} + 2c_{C_4H_x}} =$$

$$\frac{\left(c_{C_2H_2,feed} - c_{C_2H_2,product}\right)}{\left(c_{C_2H_2,feed} - c_{C_2H_2,product}\right) + c_{C_2H_6} + 2c_{C_4H_x}}$$

, where c_{feed} represents the acetylene concentration in the feed and c_x is the acetylene concentration in the product. It is assumed that acetylene is only hydrogenated to ethylene, which may be further hydrogenated to ethane. Higher hydrocarbons than C$_4$ were not observed in the experiments. The reaction temperature was 200 °C. The other conditions were chosen to be comparable to those reported in refs 10 and 11.

2.3   Results and Discussion

It is noted that Pd^{2+} is not easily incorporated in the HTlc layers due to its larger ionic size compared to Mg^{2+}, which exceeds the empirical limit of approximately 0.80 Å for the incorporation into a HTlc.[20] Furthermore, Pd^{2+} exhibits a tendency toward 4-fold square-planar coordination in aqueous solutions instead of an octahedral one present in HTlc. Therefore, only small amounts of Pd^{2+} could be incorporated in the HTlc precursor, and a second bivalent cation is required to achieve crystallization of all Pd ions in a single HTlc phase. In our example, we have chosen M$_2^{II}$ = Mg^{2+} to not interfere with the redox chemistry of the Pd-Ga system. The relative amount of trivalent cations in HTlc ranges from approximately 1:4 to 1:3, and the value of x was set to 0.3 in our preparation. Mg as well as residual Ga will remain in their oxidized states and form the support material for the Pd-Ga IMC nanoparticles. Thus, due to the homogeneous distribution and the low amount of Pd in the HTlc precursor, the formation of very small and reactive Pd0 particles is expected upon initial reduction, and the interaction with the surrounding Ga^{3+}-oxide matrix is assumed to be maximized. Clearly, the challenging step is the unfavorable reduction of Ga^{3+}, which requires elevated temperatures and competes with phase segregation and sintering. The single-phase HTlc precursor is expected to favor the formation of homogeneous, single-phase, and nanosized Pd-Ga IMCs because it provides a homogeneous microstructure concerning Pd particle size and Pd metal-oxide interactions. The Ga reduction is likely to be triggered by the strong reducing power of atomic spillover hydrogen formed on the initially formed embedded Pd^0 particles.[21] An additional advantage of the HTlc precursor method is that the synthesis is based on conventional aqueous coprecipitation which allows a feasible up-scaling.

Figure 2- 1 shows the XRD pattern of a Pd-doped HTlc precursor (2.5 mol% Pd, i.e., Pd$_{0.025}$Mg$_{0.675}$Ga$_{0.3}$(OH)$_2$(CO$_3$)$_{0.15}$ · mH$_2$O, corresponding to 3.21 wt% Pd) in comparison with the undoped pure MgGa HTlc, Mg$_{0.7}$Ga$_{0.3}$(OH)$_2$(CO$_3$)$_{0.15}$ · m H$_2$O. Both materials crystallize in the HTlc structure and exhibit high crystallinity. No other crystalline phases could be detected by XRD. The Pd content was determined to 2.83 wt% in the precursor by ICP-OES, from which a water content of m) 0.66 results, in accordance with ref [22]. Due to the low total amount of Pd, the lattice parameters of the HTlc precursors change only slightly (Table 2- 1).
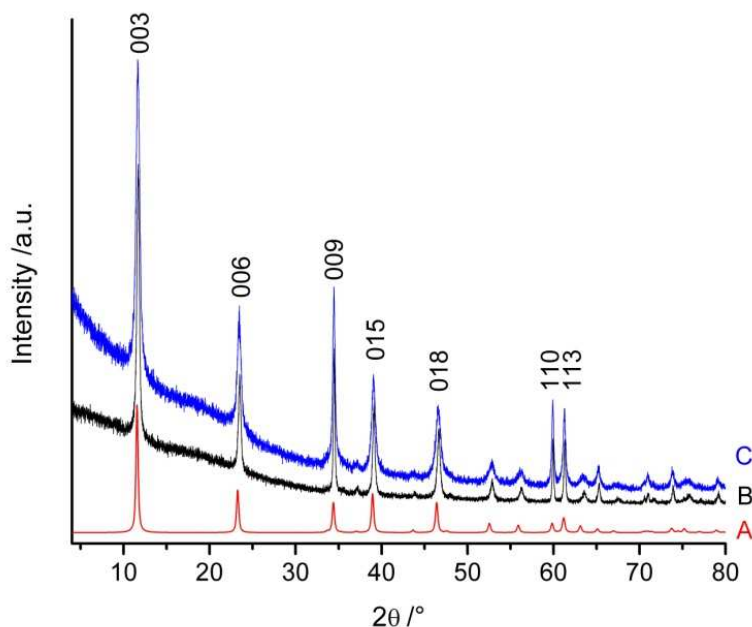
Figure 2- 1: (A) Simulated XRD pattern of MgGa HTlc. (B) XRD pattern (A) of undoped MgGa HTlc precursor. (C) Pd-doped MgGa HTlc precursor.

Table 2- 1: XRD Results of the HTl Precursors.

Sample	Lattice parameter		FWHM	
	a (Å)	c (Å)	d_{003}(2θ)	d_{110}(2θ)
Mg$_{0.66}$Ga$_{0.34}$	3.087	22.740	0.29	0.18
Mg$_{0.63}$Ga$_{0.34}$Pd$_{0.03}$	3.088	22.784	0.49	0.26

As expected for HTlc, the particle morphology is platelet-like, and the homogeneous distribution of Pd within the platelets is evidenced by elemental mapping of the precursor in the SEM (Figure 2- 2). No Pd-rich aggregates of Pd oxide or hydroxide could be detected. The specific surface area increased from 45 m^2/g to 67 m^2/g by substitution of 2.5% Mg by Pd probably due to hindered crystallite growth in the Pd-distorted HTlc. This assumption is supported by significantly higher fwhm values of the HTlc material, corresponding to smaller crystallites, in the case of the Pd-doped precursor (Table 2- 1). The particle size of the HTlc platelets is in the range of 0.4-1 μm, according to SEM (Figure 2- 2C).
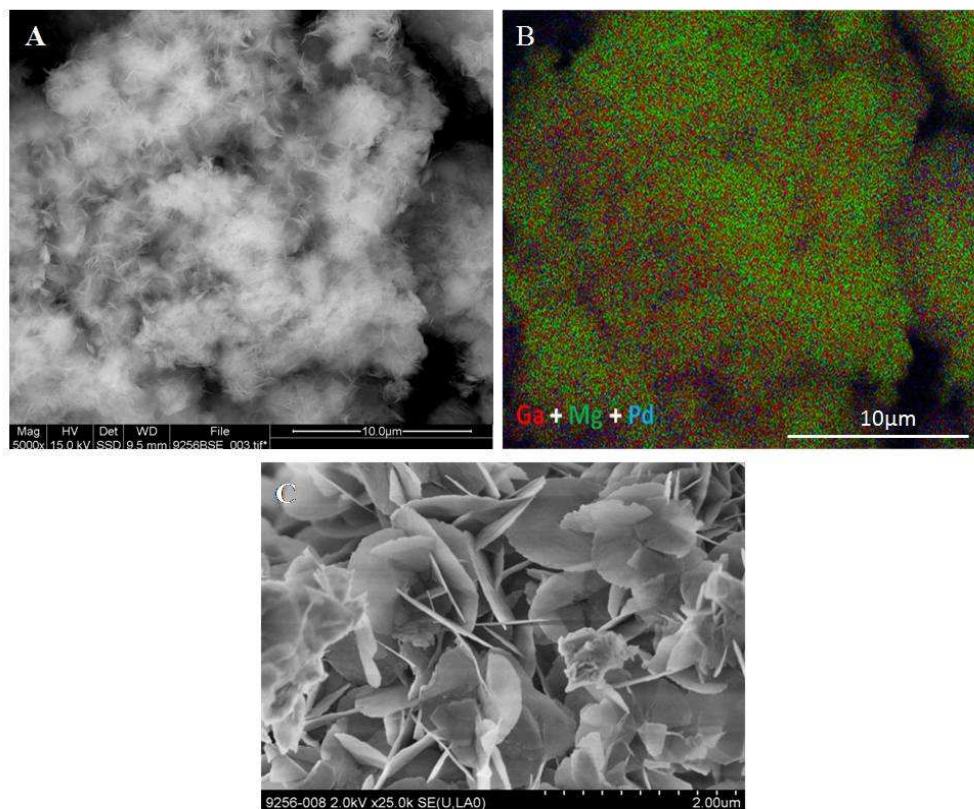
Figure 2- 2: Morphological characterization and elemental mapping of the 2.5 mol % Pd-doped
HTlc precursor. A: Low magnification SEM image. B: Corresponding elemental mapping. C:
Particle morphology at higher magnification.

To obtain the IMC, the reduction of the crystalline precursor was performed without prior
calcination in diluted hydrogen at 550 °C. The reduction enhanced the porosity of the material,
and an increased surface area of 109 m^2/g was measured for the Pd-doped sample after
reduction. By taking into account the weight loss of water and carbon dioxide during thermal
reduction, the Pd content of the reduced material is calculated to 4.49 wt%. The HTlc structure
was destroyed by the thermal treatment, and only broad modulations assigned to poorly
crystalline MgO and MgGa$_2$O$_4$ spinel (Figure 2- 3) could be detected by XRD. In particular, no
crystalline Pd phase could be unambiguously identified after thermal treatment. This is most
probably a crystallite size effect caused by the high dispersion and low total amount of the Pd
containing phase.
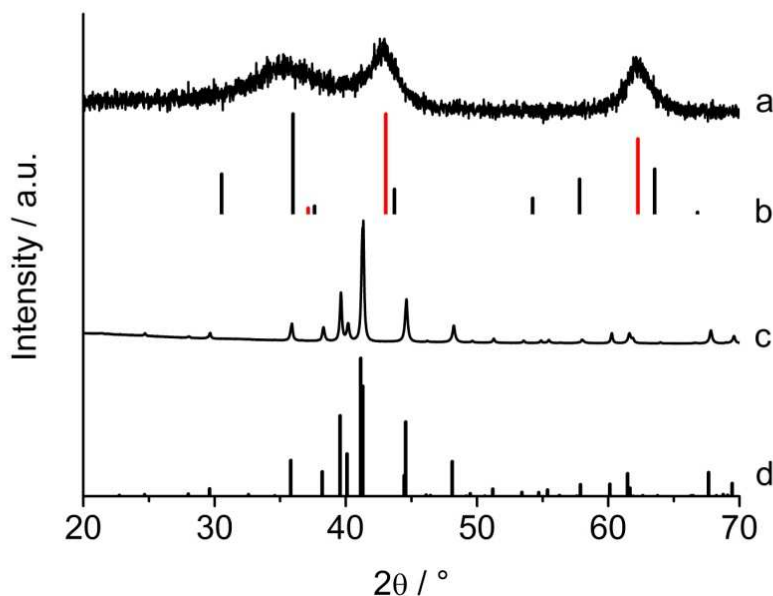
Figure 2- 3: a) XRD patterns of the catalyst obtained by reduction of the Pd doped HTlc
precursor; b) ICDD 10-113 MgGa$_2$O$_4$ (black); ICDD 1-1235 MgO (red); c) bulk Pd$_2$Ga obtained
by direct synthesis; d) Pd$_2$Ga.[23]

Using HRTEM, however, spherical and faceted particles of the IMC Pd$_2$Ga were identified after
reduction of the precursor (Figure 2- 4). In agreement with XRD, the crystalline fraction of the
oxidic support was identified as MgGa$_2$O$_4$ spinel, which has maintained the platelet-like
morphology. No particles of elemental Pd or other Pd-Ga IMCs than Pd$_2$Ga were detected by
HRTEM even after careful investigation, supporting the homogeneity of the supported
Pd$_2$Ga/MgO/MgGa$_2$O$_4$ catalyst. The mean particle diameter of the supported Pd$_2$Ga sample was
determined from projected areas measured for 882 particles in several representative images and
amounts to 6.7 ± 0.1 nm (standard deviation). The particle size distribution ranges from 1 to 30
nm for individual particles (Figure 2- 4, inset) and the volume-weighted mean size is 8.6 nm.
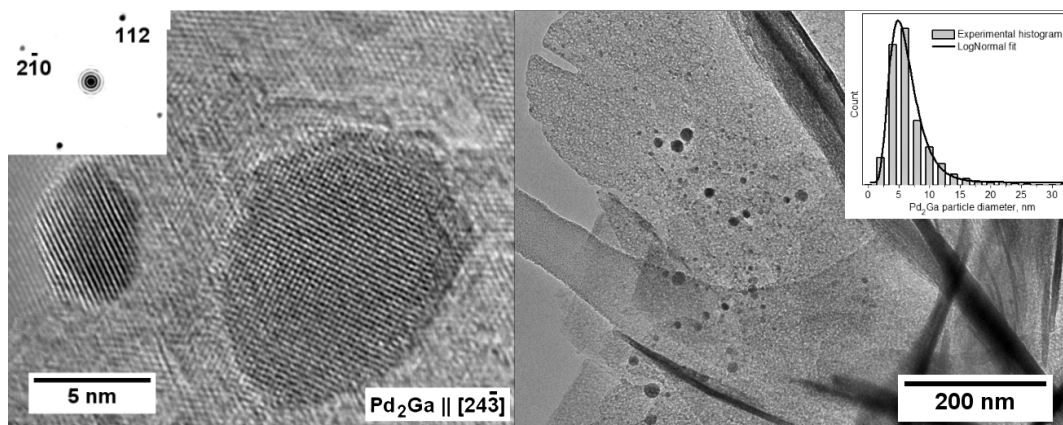
Figure 2- 4: HRTEM images of Pd$_2$Ga/MgO/MgGa$_2$O$_4$ after reduction at 550 °C in 5% H$_2$/Ar. Inset in the left image shows a Fourier transform of the larger particle; the zone axis direction is indicated in the image. Inset in the right image shows the particle size frequency distribution histogram fitted with a log-normal curve.

To get more integral information on the Pd$_2$Ga phase, the surface of the catalyst was investigated by XPS after a pretreatment in hydrogen and without exposure to air. The sample shows strong charging during XPS measurements. After several hours, the peak positions remain constant. All signals are shifted by 5.5 eV referenced to the strongest carbon 1s signal at 285.0 eV. This results in a binding energy for Mg 2p$_{3/2}$ of 50.2 eV. The Ga 2p$_{3/2}$ peak exhibited a binding energy of 1118.8 eV for the oxidic gallium but also a small component at 1116.1 eV which is in a good agreement with metallic Ga (1116.3 eV [24]). The Pd 3d$_{5/2}$ signal at 336.1 eV is shifted to higher binding energies compared to metallic Pd (Figure 2- 5) and almost symmetric. In comparison to the bulk Pd$_2$Ga phase, the measured Pd3d$_{5/2}$ binding energy of the ex-HTlc catalyst is slightly higher.[25] This could be a size effect since for small particles the positive charge of the core hole will be screened less effective, and hence the final state electron will have less kinetic energy.[26, 27]
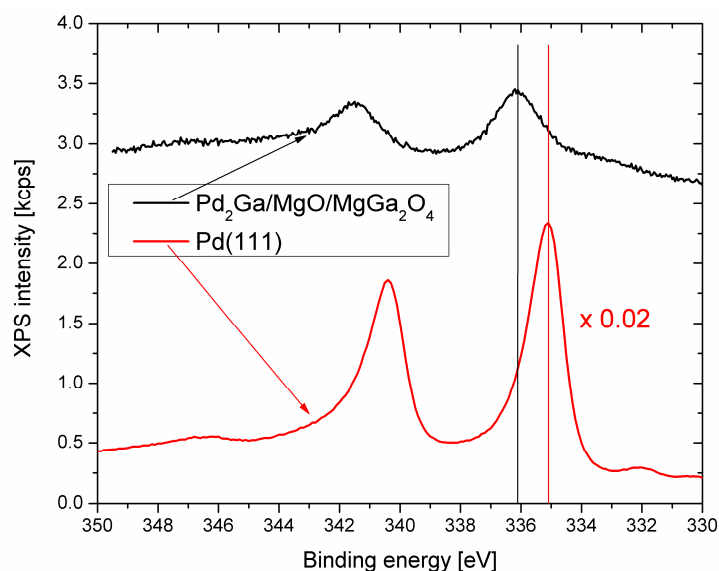
Figure 2- 5: XPS data of the Pd3d peaks of the nanostructured Pd$_2$Ga/MgO/MgGa$_2$O$_4$ catalyst compared with metallic Pd.

On the basis of the characterization results, it can be concluded that the IMC Pd$_2$Ga was accessed by the HTlc precursor approach in the form of structurally ordered nanoparticles. Their size well below 10 nm is much smaller than could be achieved by top-down approaches starting from bulk IMCs. However, the presence of minor amounts of elemental Pd particles or nanoparticulate intermetallic compounds with higher Pd content than in Pd$_2$Ga cannot be excluded, but no evidence was found by the methods applied. It is interesting to note that despite the large excess of Ga in the HTlc precursor the IMC formed at reduction temperatures up to 700 °C was always the 2:1 phase Pd$_2$Ga. This is probably due to the high stability of this phase and the nonability of this compound to form highly reactive hydrides which could reduce the Ga^{3+} in the vicinity. Furthermore, the presence of only oxidic Mg is proof for the successful parting of the Ga/Mg redox chemistry. To finally test if not only the structural but also the excellent intrinsic catalytic properties of Pd-Ga IMCs reported in the literature [10, 11] have been carried over to a nanostructured system, reference data of a well-defined bulk Pd$_2$Ga sample are needed for comparison. Such material is accessible by direct synthesis from the elements, which resulted in a single-phase sample after annealing at 900 °C (Figure 2- 3). In contrast to the HTlc approach, the synthesis is thermodynamically controlled, and the process parameters can be varied in a relatively wide temperature and also a limited compositional range according to the binary phase diagram.[28] Considering the dramatically different catalytic properties of Pd-Ga IMCs compared to elemental Pd, the observed selectivity of the samples in triple bond hydrogenation can be used as a sensitive test for the structural integrity of the IMC and the

absence of residual elemental Pd. Catalytic tests in the semi hydrogenation of acetylene were conducted at 200 °C and under atmospheric pressure for up to 25 h on stream.

Figure 2- 6 shows the conversion and selectivity of the melt-prepared bulk Pd₂Ga catalyst and the nanostructured HTlc-derived Pd₂Ga sample in comparison to a commercially available Pd/Al₂O₃ catalyst (5 wt%, Sigma Aldrich, 50 - 180 μm). Both IMC catalysts show a stable conversion of acetylene between 94 and 98% (Table 2- 2). For the supported material, an activation of about 900% was observed in the first 23 h on stream, which cannot be due to incomplete reduction of the Pd species considering the pretreatment of the catalyst in hydrogen at 500 °C for 4 h. In contrast, the Pd/Al₂O₃ catalyst showed a strong deactivation from 100 to 20% conversion not reaching steady state conditions within 20 h on stream, which is most likely due to coke formation.[29] As expected, the selectivity of the pure Pd catalyst is much lower compared to the IMCs, and an ethylene selectivity of 20% was detected after 20 h. The highest selectivity of 74% was reached with the bulk Pd₂Ga catalyst. After the strong and slow activation, the Pd₂Ga/MgO/MgGa₂O₄ catalyst showed a minimally lower selectivity of 70% after 23 h. The selectivity to higher hydrocarbons up to C₄ was not higher than 5% for all catalysts.
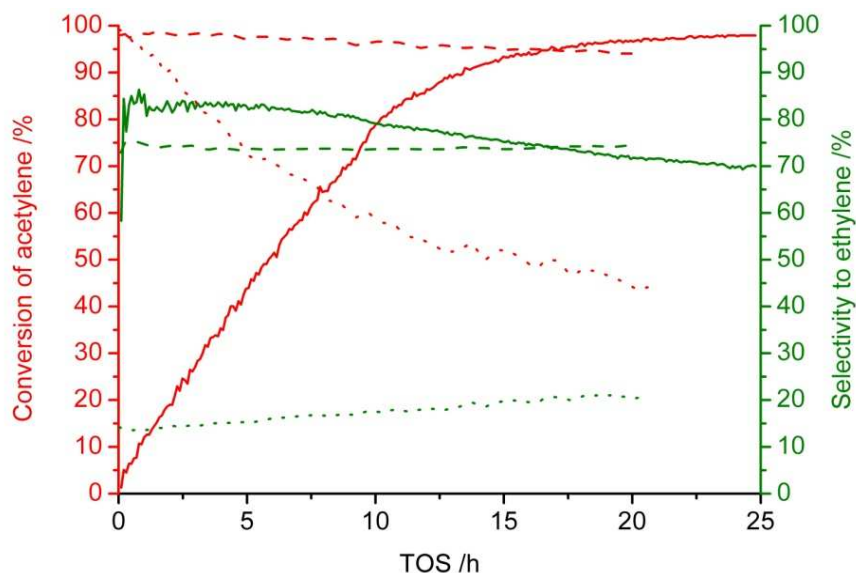
Figure 2- 6: Catalytic properties of Pd₂Ga/MgO/MgGa₂O₄ (solid line), bulk Pd₂Ga (dashed line), and 5 wt % Pd/Al₂O₃ (Aldrich; dotted line).

Table 2- 2: Catalytic Properties of Pd-Ga-Based Materials Obtained at 200 °C[a].

Catalysts	Mass / mg	Pd / mg	TOS / h	X / %	S_{C2H4}/ %	S_{C2H6}/ %	S_{C4}/ %	$W/F_{C2H2,0}$/ g·min·mol^{-1}	Activity/ mol$_{C2H2}$/mol$_{Pd}$
Bulk Pd$_2$Ga	10	7.5	20	94	74	20.7	5.3	2043.4	4.9
Pd$_2$Ga/MgO/ MgGa$_2$O$_4$	0.047[b]	1.1·10^{-3}	24	98	70	25.7	4.6	9.6	28600.4
5 wt% Pd/Al$_2$O$_3$	0.1	5·10^{-3}	20	44	20	77.8	2.2	20.4	3430.7

[a] Other experimental conditions are given in the text. [b] Mass of precursor.

In light of the similar catalytic properties of the two IMC catalysts under steady state conditions and the huge difference in particle sizes, it seems unlikely that the small difference in selectivity is related to a size effect. Other aspects also have to be considered when comparing bulk with nanoparticulate catalysts. Porosity, interactions between nanoparticles, and support or absorptivity of substrate and reaction products may also serve as an explanation for this differences.[30] In addition, the presence of minor amounts of other Pd-Ga IMC with higher Pd content and probably lower selectivity might be responsible for the slightly lower selectivity observed here. Further studies of the supported Pd$_2$Ga nanoparticles are needed to solve these issues. Nevertheless, the novel supported Pd$_2$Ga nanocatalyst clearly out-performs the nanostructured metallic Pd reference sample in selectivity as well as in stability and the bulk reference sample in activity (Table 2- 2). The activity per mass of Pd increased by a factor of 5700 compared to the bulk material. This renders the ex-HTlc Pd$_2$Ga/MgO/MgGa$_2$O$_4$ very promising for the application as a selective hydrogenation catalyst and reveals the high potential of our synthesis approach to achieve hydrogenation catalysts which resemble the selectivity of the model bulk material. Further optimization of this feasible synthesis route should enable the preparation of catalysts containing only Pd$_2$Ga as the catalytically active phase, possessing selectivities even closer to the bulk material.

2.4 Conclusion

Structurally ordered intermetallic compounds are a new promising class of catalytic materials, and Pd-Ga intermetallic compounds have shown excellent performance in the selective semi-hydrogenation substantially different from those of statistical alloys. Their intrinsic catalytic properties are related to the unique crystal and electronic structures. It was shown for the first time that these properties can be carried over from well-defined macroscopic model systems to nanostructured high performance materials by a preparation method comprising coprecipitation

of Pd, Ga, and Mg diluents in the form of a single-phase hydrotalcite-like precursor. This material can be decomposed in reducing atmosphere to yield Pd$_2$Ga nanoparticles (<10 nm) on a porous MgO/MgGa$_2$O$_4$ support. Due to the high dispersion and structural integrity of the intermetallic compound, the activity of the Pd$_2$Ga/MgO/MgGa$_2$O$_4$ catalyst is higher by a factor of more than 5700 compared to a bulk Pd$_2$Ga sample, while the selectivity and stability are still much higher than for a commercial elemental Pd reference catalyst. We suggest that this precursor method is generally promising for the synthesis of catalysts based on ordered Pd-X intermetallic compounds, X being elements forming hydrotalcite-like materials in their ionic form. Thereby, these materials, so far reported only in the form of model systems and not as high performance catalysts, are made available in the form of nanoparticles for comprehensive structural, electronic, and catalytic characterization.

2.5   References

[1]   J. Wambach, A. Baiker, A. Wokaun, *Physical Chemistry Chemical Physics* **1999**, *1*, 5071-5080.

[2]   A. Borodziński, G. C. Bond, *Catalysis Reviews: Science and Engineering* **2008**, *50*, 379 - 469.

[3]   C. N. Thanh, B. Didillon, P. Sarrazin, C. Cameron, **2000**.

[4]   F. Studt, F. Abild-Pedersen, T. Bligaard, R. Z. Sørensen, C. H. Christensen, J. K. Nørskov, *Science* **2008**, *320*, 1320-1322.

[5]   F. Studt, F. Abild-Pedersen, T. Bligaard, R. Z. Sorensen, C. H. Christensen, J. K. Norskov, *Angewandte Chemie-International Edition* **2008**, *47*, 9299-9302.

[6]   D. Teschner, J. Borsodi, A. Wootsch, Z. Révay, M. Hävecker, A. Knop-Gericke, S. D. Jackson, R. Schlögl, *Science* **2008**, *320*, 86-89.

[7]   D. Teschner, Z. Revay, J. Borsodi, M. Havecker, A. Knop-Gericke, R. Schlogl, D. Milroy, S. D. Jackson, D. Torres, P. Sautet, *Angewandte Chemie-International Edition* **2008**, *47*, 9274-9278.

[8]   K. Kovnir, M. Armbrüster, D. Teschner, T. V. Venkov, F. C. Jentoft, A. Knop-Gericke, Y. Grin, R. Schlögl, *Science and Technology of Advanced Materials* **2007**, *8*, 420-427.

[9]   H. Kohlmann, *Metal Hydrides in Encyclopedia of Physical Science and Technology*, 3rd ed., Academic Press, New York, **2002**.

[10]   J. Osswald, R. Giedigkeit, R. E. Jentoft, M. Armbrüster, F. Girgsdies, K. Kovnir, T. Ressler, Y. Grin, R. Schlögl, *Journal of Catalysis* **2008**, *258*, 210-218.

[11]   J. Osswald, K. Kovnir, M. Armbrüster, R. Giedigkeit, R. E. Jentoft, U. Wild, Y. Grin, R. Schlögl, *Journal of Catalysis* **2008**, *258*, 219-227.

[12]   K. Kovnir, J. Osswald, M. Armbruster, D. Teschner, G. Weinberg, U. Wild, A. Knop-Gericke, T. Ressler, Y. Grin, R. Schlogl, *Journal of Catalysis* **2009**, *264*, 93-103.

[13]   T. Komatsu, K. Inaba, T. Uezono, A. Onda, T. Yashima, *Applied Catalysis A: General* **2003**, *251*, 315-326.

[14]   S. Penner, H. Lorenz, W. Jochum, M. Stöger-Pollach, D. Wang, C. Rameshan, B. Klötzer, *Applied Catalysis A: General* **2009**, *358*, 193-202.

[15]   H. Lorenz, S. Penner, W. Jochum, C. Rameshan, B. Klötzer, *Applied Catalysis A: General* **2009**, *358*, 203-210.

[16]   M. Armbrüster, M. Schmidt, K. Kovnir, M. Friedrich, K. Weinhold, Y. Grin, R. Schlögl, *Vol. EP07021904A1* (Ed.: E. P. Application), **2007**.

[17]   F. Cavani, F. Trifirò, A. Vaccari, *Catalysis Today* **1991**, *11*, 173-301.

[18]   F. Basile, A. Vaccari, in *Layered Double Hydroxides-Present and Future* (Ed.: V. Rives), Nova Science Publishers Inc, New York, **2001**.

[19]   M. Behrens, I. Kasatkin, S. Kühl, G. Weinberg, *Chemistry of Materials* **2009**, *22*, 386-397.

[20]   A. De Roy, *Molecular Crystals and Liquid Crystals Science and Technology. Section A. Molecular Crystals and Liquid Crystals* **1998**, *311*, 173 -193.

[21]   V. V. Gorodetskii, A. A. Sametova, A. V. Matveev, V. M. Tapilin, *Catalysis Today* **2009**, *144*, 219-234.

[22]   M. A. Aramendia, Y. Aviles, V. Borau, J. M. Luque, J. M. Marinas, J. R. Ruiz, F. J. Urbano, *Journal of Materials Chemistry* **1999**, *9*, 1603-1607.

[23]   K. Kovnir, M. Schmidt, C. Waurisch, M. Armbrüster, Y. Prots, Y. Grin, *Zeitschrift für Kristallographie NCS* **2008**, *223*, 7-8.

[24]   S. Gunnar, *Journal of Electron Spectroscopy and Related Phenomena* **1973**, *2*, 75-86.

[25]   K. Kovnir, D. Teschner, M. Armbrüster, P. Schnörch, M. Hävecker, A. Knop-Gericke, Y. Grin, R. Schlögl, *Bessy Highlights 2007* **2008**, 22-23.

[26]   L. Zhang, R. Persaud, T. E. Madey, *Physical Review B* **1997**, *56*, 10549-10557.

[27]   L. Oberli, R. Monot, H. J. Mathieu, D. Landolt, J. Buttet, *Surface Science* **1981**, *106*, 301-307.
[28]   H. Okamoto, *Journal of Phase Equilibria and Diffusion* **2008**, *29*, 466-467.
[29]   I. Y. Ahn, J. H. Lee, S. K. Kim, S. H. Moon, *Applied Catalysis A: General* **2009**, *360*, 38-42.
[30]   G. C. Bond, *Chemical Society Reviews* **1991**, *20*, 441-475.

Chapter 3: Dynamic Surface Processes of nanostructured Pd$_2$Ga catalysts derived from ternary Hydrotalcite-like Precursors

Authors: Antje Ota, Jutta Kröhnert, Gisela Weinberg, Igor Kasatkin, Edward L. Kunkes, Frank Girgsdies, Neil Hamilton, Marc Armbrüster, Robert Schlögl, and Malte Behrens.

Abstract

A precursor synthesis approach was applied to synthesize supported intermetallic Pd$_2$Ga nanoparticles. A series of Pd-substituted MgGa-hydrotalcite-like compounds with different Pd loading was prepared by co-precipitation and studied in terms of loading, phase formation, stability and catalytic performance in selective hydrogenation of acetylene.

Higher Pd loadings than 1 mol% revealed to an incomplete incorporation of Pd into the HT lattice as evidenced by XANES and TPR measurements. Upon thermal reduction Pd$_2$Ga nanoparticles with particle sizes from 2 to 6 nm was obtained. Formation of intermetallic Pd$_2$Ga nanoparticles led to a change of the CO adsorption properties as was evidenced by IR spectroscopy. Dynamic changes of the surface were noticed at longer exposure times of CO and higher coverage at room temperature. These were ascribed to the decomposition into metallic Pd and Ga$_2$O$_3$, which was suppressed at liquid nitrogen temperature.

Reduction of the Pd precursor at 473 K is not sufficient to form the Pd$_2$Ga phase and yielded a poorly selective catalyst (26% selectivity to ethylene) in the semi-hydrogenation of acetylene. After reduction at 773 K the selectivity was increased to 80% due a change from monometallic to intermetallic state. The conversion slowly rose from 22 – 94% with time on stream. The data is interpreted in the light of chemical response of Pd and Pd$_2$Ga to the chemical potential of the reactants.

3.1 Introduction

Ordered intermetallic compounds (IMCs) are of fundamental interest due to their often complex bonding situation [1] and their application as, e.g. coating materials [2], magnets or superconductors.[3] In catalysis, IMCs have been shown to exhibit properties that differ dramatically from those of the constituting elements or of statistical alloys.[4] For example, systematic studies of metallurgically prepared bulk materials in the system Pd-Ga showed that interesting properties in selective hydrogenation are intrinsic to the IMCs Pd$_2$Ga [5] and PdGa [6, 7]. For catalytic application such IMCs are needed in form of nanoparticles supported on a high surface area material.

We have recently introduced a synthesis approach for Pd$_2$Ga intermetallic nanoparticles derived from ternary Hydrotalcite-like compounds (HTlc).[8] Pd$_2$Ga crystallizes in the orthorhombic space group P*bnm* with $a = 5.4829(8)$ Å, $b = 4.0560(4)$ Å, $c = 7.7863(8)$ Å [9] and the phase exhibits a broad homogeneity range of 27 – 36% Ga.[10] The unsupported, macrocrystalline material was reported to show a remarkable selectivity and stability in the semi-hydrogenation of acetylene [11], which were higher compared to pure Pd metal. This reaction is of industrial relevance for polyethylene production.[12] The feed gas has to be cleaned from impurities of acetylene, which otherwise poison the downstream polymerization catalyst. Thus, high selectivity towards ethylene is important not to decrease the ethylene concentration by total hydrogenation, but to effectively remove traces of acetylene at the same time.

The key to a feasible synthesis of supported Pd$_2$Ga nanoparticles is to evenly distribute the constituent species of the intermetallic compound and the support in a precursor phase. From that precursor, Pd nanoparticles are formed under reducing conditions. Upon further increase of the reduction temperature, partial reduction of the gallium species by spillover of atomic hydrogen from the metallic Pd surface [13] sets in forming the IMC, while unreduced components of the precursor constitute the oxide support. HTlc allow a high flexibility of di- and trivalent cations that are both octahedrally coordinated by hydroxyl groups and build up a joint cationic lattice that is isostructural to brucite (Mg(OH)$_2$). Edge-sharing MO$_6$ units form layers, which are positively charged due to the fraction of trivalent cations. Between these cationic sheets anions, together with neutral molecules, are intercalated to maintain the electro neutrality.[14] HTlc (or layered double hydroxides) are a highly studied class of materials due to their unique properties making them attractive for many different applications.[15-18] In catalysis, the possibility to homogenously incorporate catalytically active metal ions in the HT lattice is used to obtain well-dispersed, small and stable metal particles on a mixed oxidic support after calcination and reduction.[19]

In our previous work, the Pd^{2+}, Mg^{2+} and Ga^{3+} containing HTlc precursor was decomposed in reducing atmospheres and yielded dispersed Pd$_2$Ga nanoparticles of an average size of less than 10 nm on a porous MgO/MgGa$_2$O$_4$ support.[8] The catalytic performance in the selective hydrogenation of acetylene was tested and compared to that of bulk Pd$_2$Ga.[5, 11] We showed that catalytic bulk properties of Pd$_2$Ga were successfully transferred to a nanostructured supported system. Ethylene selectivities of 70 - 75% were reached at high conversion levels of acetylene in an excess of ethylene. Due to the successful nanostructuring, the metal based activity of the ex-HTlc catalysts was higher by more than four orders of magnitude compared to the bulk samples.

In this work, a series of Pd containing MgGa HTlc with Pd contents between 0 and 2.5 mol% was synthesized by co-precipitation of the corresponding metal nitrates. Mg^{2+} was chosen to adjust the M^{2+}/M^{3+} ratio to obtain phase pure HTlc and in order not to interfere with the redox chemistry of the Pd-Ga system. Mg as well as residual Ga will remain in their oxide state and form the support material. The substitution of Mg^{2+} by Pd^{2+} in HTlc is hindered due to its larger effective ionic radius (0.86 Å compared to 0.72 Å for Mg^{2+} [20]) and its tendency towards four-fold square-planar coordination in aqueous solutions. We examine the Pd^{2+} incorporation into the HTlc precursor, the role of Pd loading, the Ga reduction and IMC formation mechanism. The stability of the resulting intermetallic nanoparticles is investigated in different atmospheres and under reaction conditions. A multi-technique approach (XRD, BET, XANES, TPR-MS, CO-IR) was used to characterize the precursor as well as the resulting catalyst in detail and their catalytic performance was tested in the semi-hydrogenation of acetylene.

3.2   Experimental

3.2.1   Synthesis conditions

The Pd-Mg-Ga HTlc precursors were synthesized by controlled co-precipitation at pH = 8.5 and 328 K by co-feeding appropriate amounts of mixed aqueous metal nitrate ([Pd^{2+}] + [Mg^{2+}] + [Ga^{3+}] = 0.2 M) and 0.345 M sodium carbonate solution as precipitating agent. Both solutions were added simultaneously dropwise into a 2 L precipitation reactor (Mettler-Toledo LabMax). The nitrate solution was automatically pumped with a constant dosing rate and the basic solution was added to maintain a constant pH of 8.5. After completion of addition, the mixture was aged for 1 h at 328 K. A typical co-precipitation log is presented as supporting information (Figure S3- 1). The precipitate was filtered and washed twice with warm deionized water in

order to remove the nitrate and sodium ions until the conductivity of the filtrate lower than 0.2 mS/cm. The solid was dried for 12 h at 353 K in air. The ($[Mg^{2+}]+[Pd^{2+}]$)/Ga^{3+} ratio was fixed at 70:30 and the Pd^{2+} content was varied between 0 and 2.5 mol% resulting in HTlc compositions of $(Mg_{0.7-x}Pd_x)Ga_{0.3}(OH)_2(CO_3) \cdot m\ H_2O$ with $0 \leq x \leq 0.025$. The precursors were reduced in 5 Vol% H$_2$ in Argon at 773 K to obtain the supported Pd$_2$Ga compounds. The heating rate was 2 K/min and the final temperature was kept for 4 h. Precursor samples will be hereafter referred to as Pdx, where x is the nominal Pd content (mol% · 10), whereas the reduced samples will be referred to as Pd$_2$Gax.

3.2.2   Characterization

X-ray diffraction (XRD) patterns of the HTlc precursor and its decomposition products were recorded on a STOE Stadi P diffractometer in transmission geometry using Cu Kα$_1$ radiation, a primary Ge monochromater and a 3° linear position sensitive detector. Specific surface areas (SSA) of the precursors and reduced compounds were determined by N$_2$ adsorption–desorption measurements at 77 K by employing the BET method (Autosorb-1C, Quantachrome). Prior to N$_2$ adsorption, the samples were outgassed at 353K (precursors) or 423 K (reduced catalyst) to desorb moisture adsorbed on the surface and inside the porous network.

For chemical analysis about 5 mg were exactly weighted in and dissolved in 2 ml aqua regia. The solutions were transferred and filled up in 50 ml volumetric flasks. The content of the metals were determined with ICP-OES (Vista RL, Varian) after matrix matched calibration. The temperature programmed reduction (TPR) experiments were performed in a fixed bed reactor using 400 mg of precursor (100 - 250 µm sieve fraction). Precursors were reduced in 5 Vol% H$_2$ in Argon at a heating rate 2 K/min (100ml/min flow), up to a sample temperature of 773 K. The temperature was kept constant for 4 h and recorded with a thermocouple. The hydrogen consumption was monitored with a thermal conductivity detector. Evolved gas was analyzed in on a quadrupole mass spectrometer (QMS200 Omnistar, Balzers).

X-ray absorption near edge structure (XANES) measurements at the Pd K edge (24.350 keV) were carried out at the Super-XAS beamline at the Swiss Light Source (Villigen, Switzerland), using ion chambers as detectors and a Si(311) Quick EXAFS monochromator. A Pd foil placed between the second and third ion chamber was measured simultaneously as an internal reference. In-situ XANES measurements during hydrogen TPR were performed in transmission mode, using a capillary reactor cell. The precursor (63-100 µm, 30 mg) was filled in the capillary between quartz wool plugs. The cell was connected to a gas manifold. Spectra were collected during the reduction in 5 Vol % H$_2$/N$_2$ in the temperature range of 303 - 773 K. Reduction of the XAS data was performed using the Athena 0.8.056 software package.

For the XANES evaluation, two reference spectra for square-planar and octahedral environment were used in order to study Pd coordination geometry. A commercial PdO (puriss, Fluka) and PdZnAl Hydrotalcite-like precursor (molar Pd:Zn:Al ratio = 1.0:69.5:29.5), that was prepared by co-precipitation as well. On the appropriateness of the latter material as a reference of Pd^{2+} in HTlc see ref. [21] and supporting information (Figure S3- 2). Linear combination analysis of the spectra of PdO and PdZnAl HTlc was used to obtain the fraction of Pd in MgGa HTlc present as PdO and as incorporated within HTlc structure.

The adsorption of CO on the reduced catalyst was studied with IR spectroscopy. Measurements were carried out using a Perkin-Elmer Pe100 spectrometer equipped with a MCI detector. The spectra were recorded with a resolution of 2 cm^{-1} and an accumulation of 64 scans. Self-supported wafers were obtained by pressing the powdery sample under a pressure of 123 MPa. The sample was treated directly in the IR cell which is connected to a vacuum system with a residual pressure of about 10^{-7} mbar. Prior the CO adsorption measurements, the samples were reduced in 500 mbar H$_2$ at 473 or 773 K for 2 or 4 h and then evacuated at the same temperature for 30 min. For low-temperature CO adsorption, the sample was cooled to liquid nitrogen temperature (77 K). The empty cell was used to generate background spectra. Difference spectra were obtained through subtraction of the spectrum of the treated sample in vacuum from the spectrum in presence of CO. In order to understand the activation process, which was observed during the acetylene hydrogenation, the treatment was adopted comparable to the catalytic measurements. A freshly reduced catalyst was exposed to 5 Vol% O$_2$/He for 30 min at 473 K. Pellets of this samples were afterwards pre-treated at 473 K under static conditions in 200 mbar H$_2$ and in 10 mbar 1:15:30 C$_2$H$_2$:H$_2$:C$_2$H$_4$ mixture. The gaseous atmosphere was exchanged every 15 min to remove the evolved products. Before the CO adsorption measurements, the samples were evacuated at 473 K before cooling to room temperature.

Scanning electron microscopy (SEM) images were acquired with a Hitachi S4800 FEG microscope equipped with an EDS system (EDAX) for elemental analysis. The samples were loosely dispersed on a conductive carbon tape to preserve the as-prepared morphology as much as possible. EDX spectra were acquired at an accelerating voltage of 15 kV. High resolution transition electron microscopy (HRTEM) images were acquired using a FEI TITAN microscope, equipped with a field emission gun (FEG) and operated at 300 kV. With computer assisted correction and alignment, the value of the spherical aberration constant Cs was kept below 100 nm in the present experiments. Selected areas of the high resolution images have been Fourier transformed to obtain power spectra and the lattice distances and angles were measured (accuracy ± 1 % and ± 0.5 deg, correspondingly) for phase identification. For particle size determination, projected areas have been measured and equivalent diameters calculated for

500 - 2500 metallic Pd or intermetallic Pd_2Ga nanoparticles in each sample. In all cases the values of standard error of the mean diameter were ≤ 0.1 nm. Frequency distributions of the particle sizes fitted well to Gauss functions rather than Log Normal functions.

3.2.3 Catalytic performance in the selective hydrogenation of acetylene

Measurements were performed in a quartz tube reactor at ambient pressure. The reaction temperature of 473 K was measured in the catalyst bed. The effluent of the reactor was analyzed in 20 min-intervals using an Agilent 7890A gas chromatograph equipped with a J&W scientific Haysep Q and Agilent DB1 column, a flame ionization detector and a thermal conductivity detector. Gas-phase species up to C_6 were quantified. A pre-mixed gas mixture (Westfalen) was used consisting of 1 Vol% Acetylene (2.6), 15 Vol% Hydrogen (5.0), 30 Vol% Ethane (2.5), 5 Vol% Argon (5.0) and 49 Vol% Helium (4.6). This mixture approximates the composition of a front-end stream of a cracking process. The flow rate of the reactants was 100 ml/min. Prior the measurements the HTlc precursor was diluted to 100:1 with boron nitride and mixed with 1 g SiO_2 (100-250 µm), before being filled into the reactor. Herein 0.2 mg of the 2.5 mol% PdMgGa HTlc was used for catalytic tests, while for the low temperature reduction 0.4 mg of the precursor lead to a similar conversion. The samples were reduced in-situ at 473 (2 h)/773 K (4 h) in 5 Vol% H_2/Argon and afterwards cooled to the reaction temperature. After reaching the reaction temperature, the feed gas was switched on and after 5 min the first chromatogram was measured. Conversion of acetylene and the ethylene selectivity has been calculated according to the following equations:

$$X_{C_2H_2} = \frac{r_{acetylene,\,in} - r_{acetylene,\,out}}{r_{acetylene,\,in}}$$

$$Sel_{C_2H_4} = \frac{r_{acetylene,in} - r_{acetylene,out}}{\left(r_{acetylene,in} - r_{acetylene,out}\right) + r_{ethane} + 2r_{C_4H_x} + 3r_{C_6H_x}}$$

It is noted that a full conversion $X_{C2H2} = 100\%$ does not necessarily correspond to complete thermodynamic control, which would result in full hydrogenation of all unsaturated bond, i.e. also of all ethylene in the feed. Internal mass transport limitations were excluded based on the Weisz-Prater criterion ($N_{W-P} = 1.7 \; 10^{-2}$).

3.3   Results and Discussion

3.3.1   Structural and textural properties of the precursor material

HTlc precursors of the nominal composition $(Mg_{0.7-x}Pd_x)Ga_{0.3}(OH)_2(CO_3) \cdot m H_2O$ have been
prepared by co-precipitation with Pd contents of 0 - 2.5 mol%. Chemical analysis shows a
constant, but slightly lower than expected Mg:Ga ratio for all samples and confirms the
presence of Pd in the precipitates (Table 3- 1).

Table 3- 1: Chemical composition, surface area and lattice parameter.

Sample	Chemical Composition[a] Pd:Mg:Ga	SSA Precursor [m²/g]	Pd content [wt%][b]	SSA after reduction [m²/g]	Lattice parameter		Fwhm d(003)
					a [Å]	c [Å]	
Pd0	0.0:63.2:36.8	34	0	130	3.087	22.740	0.224
Pd01	0.1:65.6:34.3	42	0.16	103	3.087	22.763	0.325
Pd03	0.3:65.8:33.9	41	0.56	113	3.087	22.778	0.331
Pd05	0.6:64.0:35.4	44	0.98	108	3.086	22.721	0.347
Pd08	0.8:65.4:33.8	44	1.52	117	3.086	22.778	0.379
Pd10	1.0:64.5:34.5	48	1.81	116	3.087	22.755	0.374
Pd15	1.6:64.5:33.9	52	2.79	106	3.087	22.769	0.393
Pd25	2.8:63.6:33.6	59	4.87	118	3.085	22.753	0.421

[a] determined by ICP-OES; [b] Pd content after reduction at 773 K

The XRD patterns of the samples are shown in Figure 3- 1. All patterns indicate a high
crystallinity and phase-pure HTlc structure. No crystalline Pd containing by-phase was observed
up to a Pd loading of 2.5 mol%. By Rietveld refinement (not shown) the lattice parameters were
determined and are reported in Table 3- 1. For Pd0 the calculated *a* and *c* parameter of 3.087 Å
and 22.7 Å, respectively, are close to those reported in literature.[22-24] Lopéz et al. [22] varied the
Mg:Ga ratio from 12.9-1.8 in their studies and observed a linear decrease of the *a* parameter
(3.123 - 3.086 Å), indicating that smaller Ga^{3+} cations incorporate into the layered structure to a
variable extent. Also the interlayer spacing, related to the *c* parameter, shrinks (24.52 - 22.72 Å)
as the Ga content increases, due to a greater electrostatic attraction between layers and
interlayers. For our samples, the lattice parameters of the Pd substituted samples are similar to
those of the unsubstituted precursor and do not show a trend with the Pd content. This suggests
that the amount of Pd^{2+} incorporated into the HTlc is low or that substitution of Mg^{2+} by Pd^{2+}

has little impact on the structure although Pd^{2+} exhibits a larger ionic radius (0.86 Å [20]). However, no reliable conclusion about Pd incorporation in the investigated compositional range can be drawn from the XRD results. Recently, Das et al. [25] reported about ternary PdMgAl Hydrotalcite-like compounds with similarly low Pd contents and claimed incorporation of Pd^{2+} by means of XRD results. In our samples only a linear increase of the FWHM of the basal XRD peaks was observed (Table 3- 1). This trend is shown in Figure 3- 1 (bottom) for the 003 reflection. The presence of Pd in the HTlc lattice probably interferes with the crystallite growth and reduces the platelet thickness significantly. These observations are in agreement with an increase in the specific surface area from 34 to 59 m^2/g for 0 and 2.5 mol% Pd, respectively.
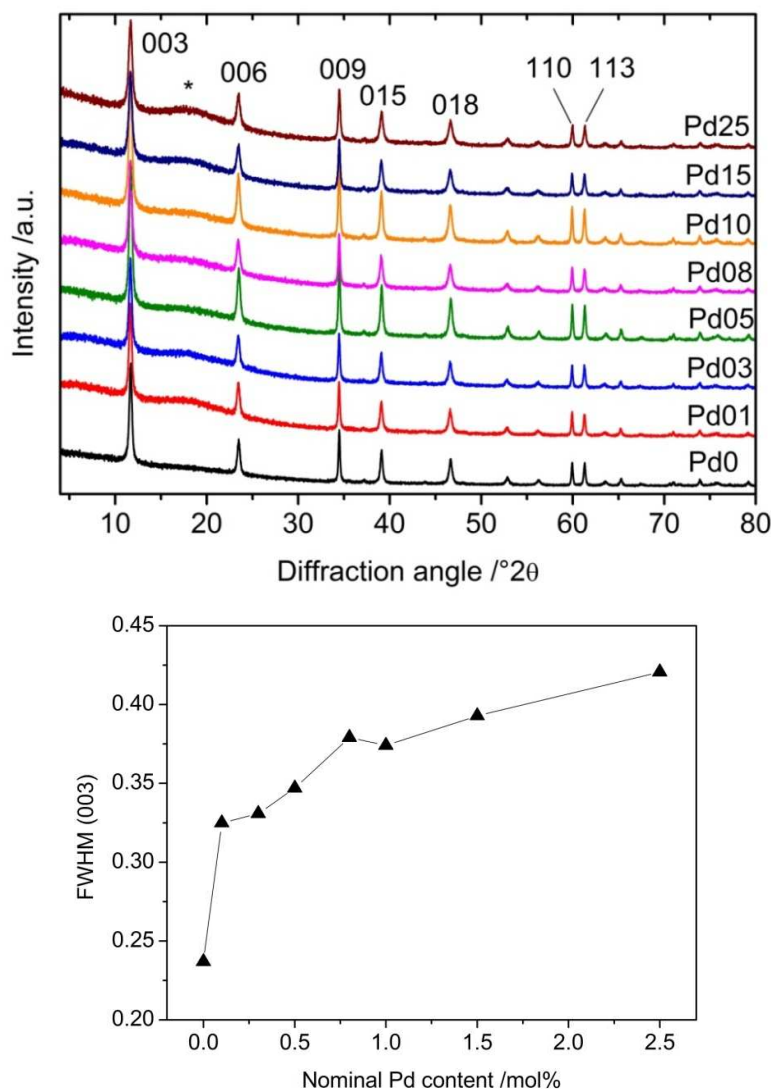
Figure 3- 1: (top) XRD patterns of the MgGa HTlc precursor with different Pd loadings (*grease). (bottom) FWHM of (003) reflection in dependency of the Pd loading.

45

Scanning electron microscopy was applied to study the morphological properties of the materials. Typical plate-like particles were obtained for all the samples, as illustrated in Figure 3- 2 for sample Pd10. The platelets are approximately 1 µm in diameter and the thickness is in the order of 5-20 nm. Elemental mapping (not shown) revealed a homogenous metal distribution and no agglomerates were observed. In case of 1 mol% Pd sample an EDX line scan of the Mg K-, Ga L- and Pd L fluorescence lines displayed a homogenous metal distribution for all three metal species within a larger aggregate (Figure 3- 2b). With this method, Pd rich areas were observed for 1.5 mol% and 2.5 mol% Pd loadings suggesting that either the upper limit for the incorporation of Pd into the HTlc layers is < 1 mol% or that the detection limit of the method is reached due to the small Pd content in the samples. This inhomogeneous metal distribution in the Pd-rich samples was confirmed by contrast fluctuations in the backscattering electron microscopy image (Figure S3- 3).
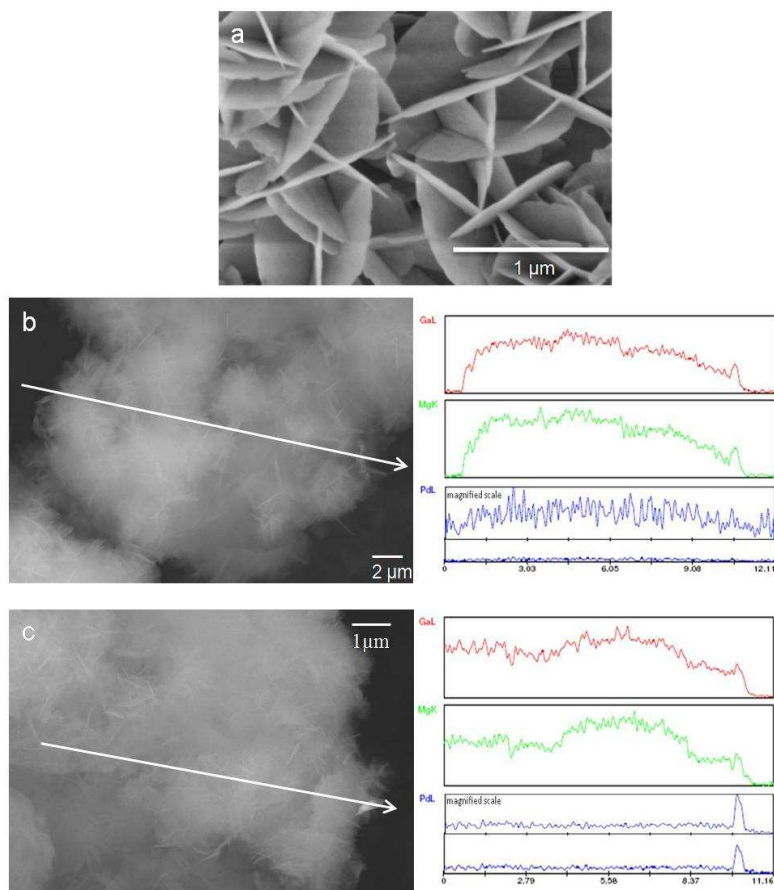
Figure 3- 2: SEM micrographs of Pd10 (a), EDX line of (b) Pd10 and (c) Pd25.

The analysis of the X-ray absorption near-edge structure (XANES) data, which contain information about the coordination environment of Pd, was used to determine the degree of incorporation of Pd^{2+} into the HTlc structure in our samples. As already mentioned, Pd^{2+} prefers square planar coordination, while incorporation into the HTlc lattice requires octahedral coordination of the cations. The low-spin d^8 electronic configuration of Pd^{2+} makes regular octahedral coordination unstable with respect to strong tetragonal elongations. Octahedral coordination of Pd^{2+} with oxygen was obtained at 12 GPa in a high pressure polymorph of PdO [26] and for higher oxidation states of Pd, tri- and tetravalent palladium. For instance, in Zn$_2$PdO$_4$ Pd^{4+} has regular octahedral symmetry in a cubic spinel structure [27], Pd^{3+} was stabilized in octahedral coordination in LaPdO$_3$ - a distorted perovskite structure.[28] The XANES spectra of Pd10 and 25 precursors are shown in Figure 3- 3. As reference, PdO is included as a typical example for Pd^{2+} in square planar coordination of oxygen. The reference sample for the octahedral coordination of Pd^{2+} is a Pd doped ZnAl HTlc sample, which is described in detail elsewhere [21] and shows a shape of the white line that is similar to that of Pd in distorted octahedral coordination in LaFe$_{0.95}$Pd$_{0.05}$O$_3$ perovskite.[29]
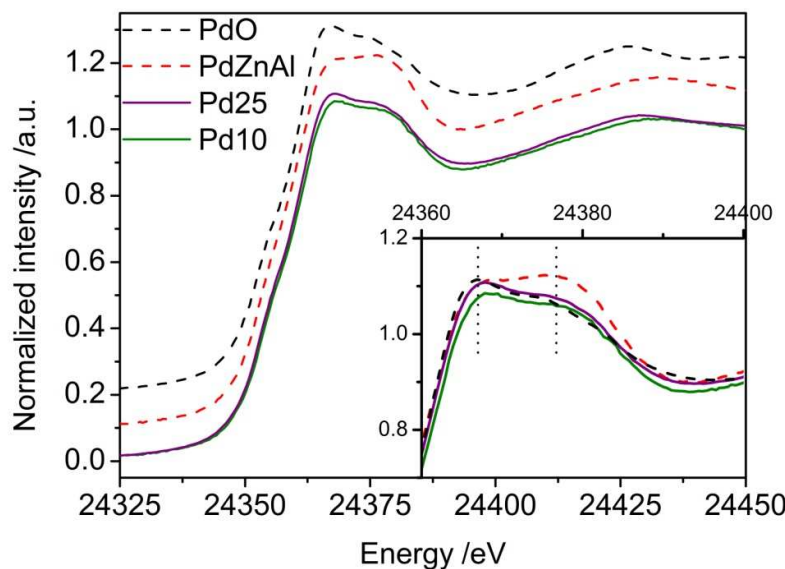
Figure 3- 3: Normalized XANES spectra at the Pd K-edge of Pd10 and Pd25 in comparison to PdO and PdZnAl HTlc, serving as reference spectra for Pd^{2+} in square planar and octahedral coordination of oxygen.

The XANES spectra of the two samples Pd10 and Pd25 show similarities with both references. While the first feature at 24367 eV can be assigned to segregated Pd in square planar coordination, the second maximum at 24376 eV is assigned to the octahedrally coordinated Pd

in the HTlc lattice. A linear combination analysis of the XANES region was applied to determine the contribution of square planar and octahedral coordination of Pd (Figure 3- 4). While for Pd25 46% of Pd is incorporated into the HTlc lattice, the amount increases to 68% with decreasing Pd loading to 1.0 mol%. With respect to the total metal content, these values correspond to 1.3 mol% and 0.7 mol% Pd residing in the HTlc lattice in Pd25 and Pd10, respectively. Apparently the limit for Pd incorporation into the HTlc precursors is not sharp, but seems to be around 1 mol%. Kinetic factors as well as the amount of incorporated Ga may also affect the size of the lattice site available for Pd and contribute to the amount of inserted Pd^{2+}.
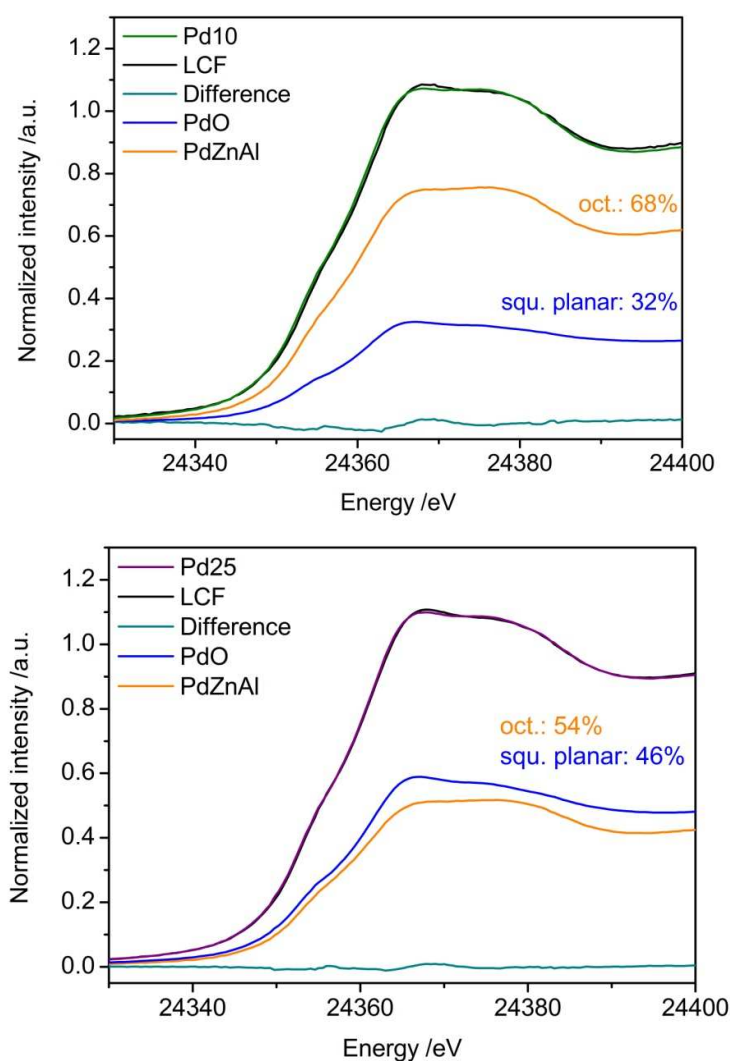
Figure 3- 4: Linear combination fit (LCF) of Pd10 and Pd25 with respect to square planar and octahedral coordination of Pd.

In summary, a series of Pd substituted MgGa HTlc samples are successfully synthesized via co-precipitation yielding highly crystalline, well defined precursors. By SEM-EDX analysis Pd-rich areas are noticed with increased Pd loading indicating a limit of incorporation of Pd into the HTlc lattice. XANES measurements confirm that incorporation of Pd^{2+} in the energetically disfavored octahedral environment is possible to a certain extent.

3.3.2   Reduction and intermetallic phase formation

The decomposition and reduction processes of the precursor samples were followed by temperature programmed reduction experiments. The hydrogen consumption was quantified by a TC detector and decomposition products were qualitatively analyzed by MS. Additionally, in-situ XAS measurements were performed to follow the formation of Pd_2Ga.

Upon feeding of hydrogen over the precursors at room temperature hydrogen was rapidly consumed. Between 10 and 100 min depending on the Pd content were spend before the TCD signal was stable again and the samples were heated to 773 K. For Pd10, Pd15 and Pd25 the consumption corresponds to 7.2 µmol, 46.3 µmol and 61.7 µmol hydrogen, respectively. The fraction of segregated PdO-like Pd species, which is assumed to be reduced at lower temperature compared to Pd^{2+} in the HTlc lattice, was estimated to 32% in sample Pd10 on basis of the XANES evaluation. This is in good agreement with hydrogen consumption at room temperature which result in a reduction degree of 25% of the total Pd content. Further reasonable agreement is obtained for Pd25, where according to TPR 54% of the Pd was reduced at room temperature and 68% extra-lattice Pd have been detected by XANES. Interestingly, up to a Pd content of 0.8 mol% only negligible amounts of hydrogen were consumed at room temperature. This indicates that all Pd^{2+} is octahedrally coordinated and stabilized in the HTlc lattice against room temperature reduction.

The profiles of mass signals m/e = 15, 18, 28 and 44 observed during reduction in hydrogen are shown in Figure 3- 5 for Pd0, Pd10 and Pd25. At the beginning of the reduction process mainly water (m/z = 18) is released from the interlamellar space. A maximum is observed at 448 K for all samples. Simultaneously, labile carbonate ions decompose into CO_2 (m/z = 44) and are observed in small quantities. Upon heating to 773 K additional water evolution is detected and leveled off during temperature holding. The release of water is related to the dehydroxylation of the brucite-like layers. CO_2 release starts around 573 K and result from decarboxylation of the interlayer space which is usually observed during thermal treatment for HTlc.[30] Shortly thereafter CO formation (m/z = 28) is noticed, which is a product of the reverse water gas shift reaction (rWGS: $CO_2 + H_2 \rightarrow CO + H_2O$) of the released CO_2 with the hydrogen feed over the pure support and the Pd modified surface. RWGS activity was also reported for pure Ga_2O_3 at

temperatures above 603 K.[31] Whereas conversion of CO_2 to CO occurs at the same temperature
for the Pd substituted precursors (693 K), it is delayed in case of the Pd free precursor (723 K)
as illustrated in Figure 3- 5 (left). Pd seems to promote the earlier formation of partially reduced
Ga species and shifts the onset of rWGS over Ga$_2$O$_3$ to lower temperatures. In addition, for
sample Pd25 traces of methane (m/z =15) are observed at 723 K, probably due to methanation
of CO on the relatively large amount of metallic Pd in this sample.
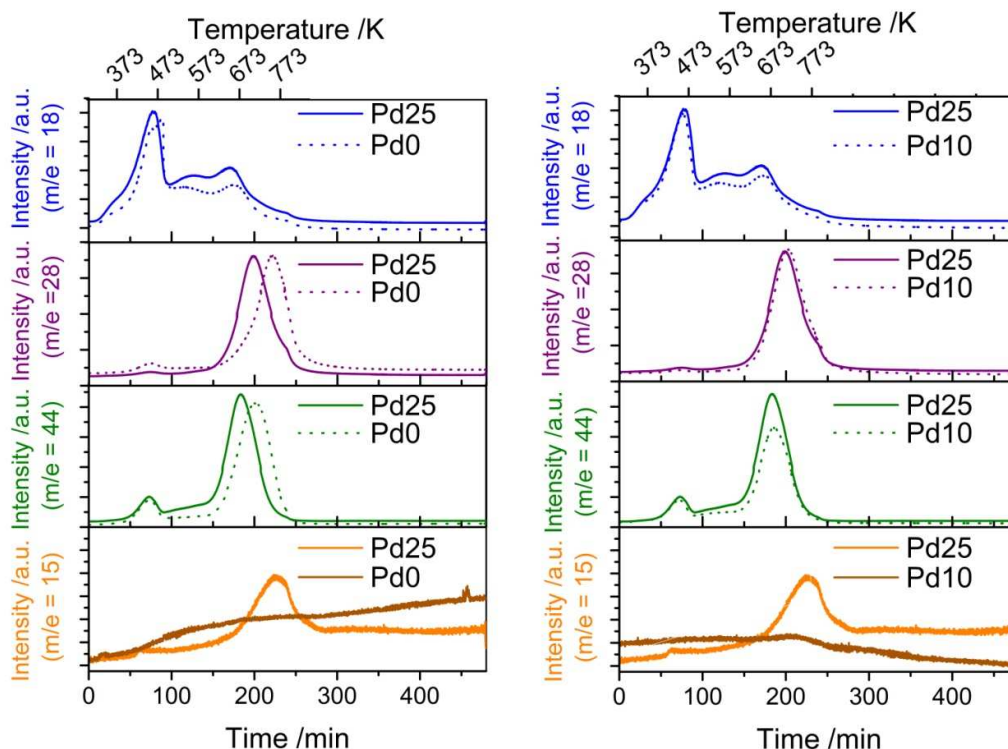
Figure 3- 5: Mass signals during thermal decomposition and reduction of Pd0, Pd10 and Pd25
HTlc in 5 Vol% H$_2$/Argon (heating rate 2 K/min).

Figure 3- 6 illustrates the TPR profiles after completion of RT reduction for various Pd
loadings. In general, two signals were observed for the Pd doped samples during heating. A low
temperature reduction (LTR) peak occurs at between 383 K and 403 K. This peak is assigned to
the reduction of Pd^{2+} incorporated into the HTlc lattice to metallic Pd. With increasing Pd
loading a slight shift to lower temperatures is observed, probably due to the increasing Pd
concentration in the precursor that facilitates formation of Pd^0 particles. The degree of Pd
reduction was found to decrease with increasing Pd content (Table 3- 2). Whereas the excess of
H$_2$/Pd added up to 215% for Pd01, it significantly decreased to 70% for Pd25. Taking the
amount the hydrogen consumed at room temperature also into account, the value of excess

H_2/Pd always exceeded 100% required for the stoichiometric reduction of PdO (PdO + H_2 → Pd + H_2O). This excess is probably attributed to PdH_x formation and spillover hydrogen from the metal to the support. Iwasa et al.[32] reported on TPR studies of Pt and Pd nanoparticles supported on several oxides, for instance ZnO, Ga_2O_3, MgO and Al_2O_3. They also observed higher hydrogen consumptions at room temperature than were required to reduce the Pd. In their samples, formation of a PdH_x phase was concluded and could be confirmed by in-situ XRD. In addition, desorption of hydrogen, producing a weak inverse peaks around 323 – 363 K, was observed. In contrast to the work of Iwasa et al.[32] no desorption of hydrogen was observed for our samples that result from decomposition of a Pd hydride phase.

A high temperature reduction (HTR) peak is observed between 693 and 709 K for all HTlc samples. The HTR peak is significantly shifted to lower temperature with increasing Pd content. The peak maxima shifts from 732 K (Pd0) to 692 K (Pd25). If the amount of hydrogen is related to reduction of gallium species, between 5 and 25% of Ga are reduced to Ga^0 during HTR in Pd0 and Pd25, respectively. These large values are easily explained by the observed rWGS (Figure 3- 5) in the same temperature range. Hence, the HTR peak has two contributions. On the one hand it is related CO formation and on the other hand to Ga reduction and intermetallic phase formation.
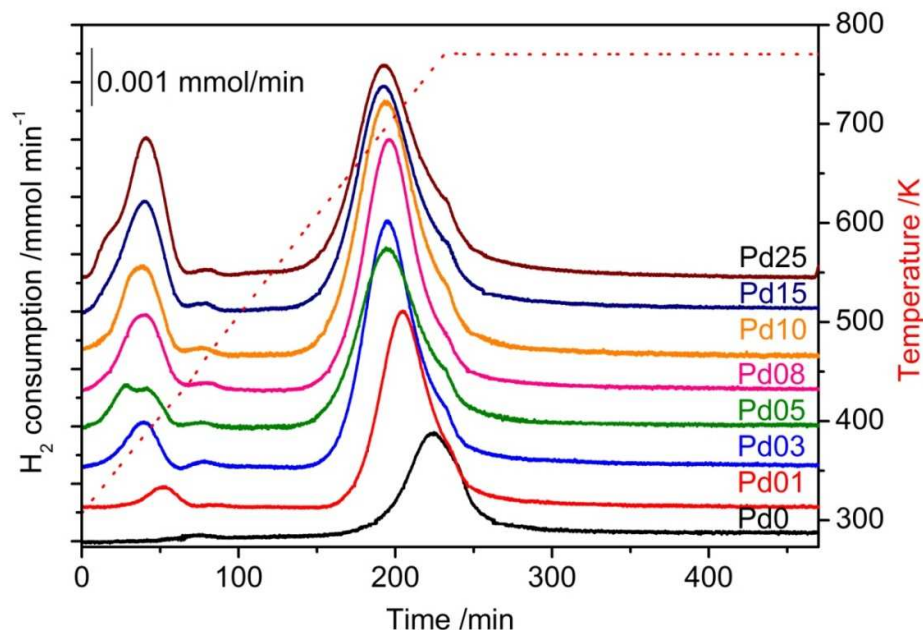
Figure 3- 6: TPR profiles of the HTlc precursors in 5%H_2/Argon.

Table 3- 2: Quantification of the TPR experiments.

Sample	Pd[a] [wt%]	Ga[a] [wt%]	T$_{LTR}$[b] [K]	T$_{HTR}$[b] [K]	Pd RTR[c] [%]	Pd LTR[c] [%]	Sum RTR+LTR[d] [%]
Support	0	25.8	-	732	-	-	-
Pd$_2$Ga01	0.10	25.2	403	709	0	216	216
Pd$_2$Ga03	0.35	25.1	395	700	10	140	150
Pd$_2$Ga05	0.61	25.8	387	696	5	129	134
Pd$_2$Ga08	0.94	24.9	384	697	15	107	121
Pd$_2$Ga10	1.13	25.2	382	694	26	102	128
Pd$_2$Ga15	1.73	24.7	387	693	70	85	155
Pd$_2$Ga25	3.01	24.2	386	692	61	70	131

[a] Pd/Ga content of precursor determined by ICP-OES; [b] Low (LTR) and high temperature reduction (HTR); [c] Calculated Pd fraction that is reduced at room temperature (RTR) / low temperature (LTR); [d] Total fraction of Pd that is reduced at RT and LT

Figure 3- 7 shows the in-situ XANES spectra of the Pd25 precursor collected during reduction in hydrogen compared with palladium foil and bulk Pd$_2$Ga (dashed black and red line, respectively). The most notable differences between the two references are generally lower amplitudes of the oscillations and a slight shift of the spectral features at 24390, and 24429 eV of bulk-Pd to lower energies (24387, and 24420 eV) for bulk-Pd$_2$Ga. A detailed representation of Pd25 is shown in Figure 3- 7B. With increasing reduction temperature and time the damping as well as the low-energy shift of the spectral features can be observed. With the exception of the spectrum collected at 373 K (pink line), which according to TPR and in agreement with the strong white line still contains oxidized Pd, five isosbestic points are observed suggesting that a direct transformation of Pd metal into Pd$_2$Ga occurs without Pd-containing intermediates. The phase formation from metallic palladium to intermetallic Pd$_2$Ga is completed when the temperature is kept constant at 773 K.
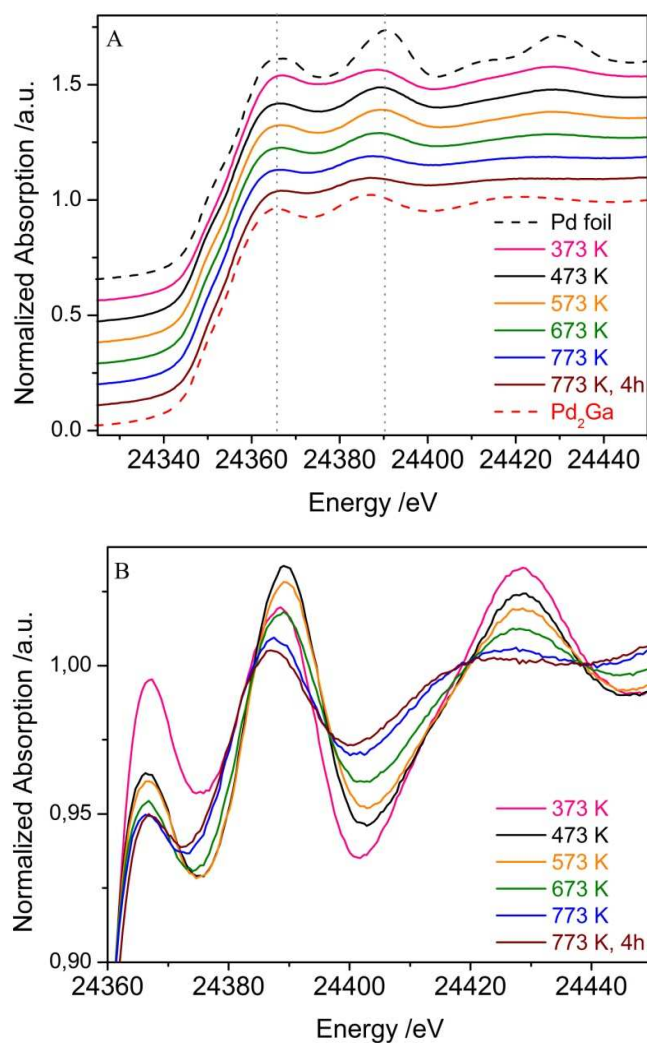
Figure 3- 7: Normalized XANES spectra of Pd25 during reduction. Pd foil and bulk Pd$_2$Ga are added as references (black and red dashed lines).

In brief, upon thermal reduction in hydrogen the precursor is decomposed and is transformed into supported intermetallic Pd$_2$Ga nanoparticles. The phase formation is accompanied by CO formation due to rWGS. The formation of metallic Pd as well as intermetallic Pd$_2$Ga is facilitated with increasing Pd loading and the onset of the reduction peaks are shifted to lower temperatures with increasing Pd loading. TPR and XANES measurements confirm that a temperature of 773 K is needed for complete transformation of Pd to Pd$_2$Ga nanoparticles.

3.3.3 Structural properties of Pd$_2$Ga nanoparticles

TEM analysis was used to study the morphology and the phase identification of Pd containing
particles as well the support. Samples with different Pd loadings were investigated with respect
to particle size and phase composition. Furthermore, the influence of reduction temperature and
the exposure to air after reduction were studied. Samples with 0.5, 1.0 and 2.5 mol% Pd loading
were selected as representatives.
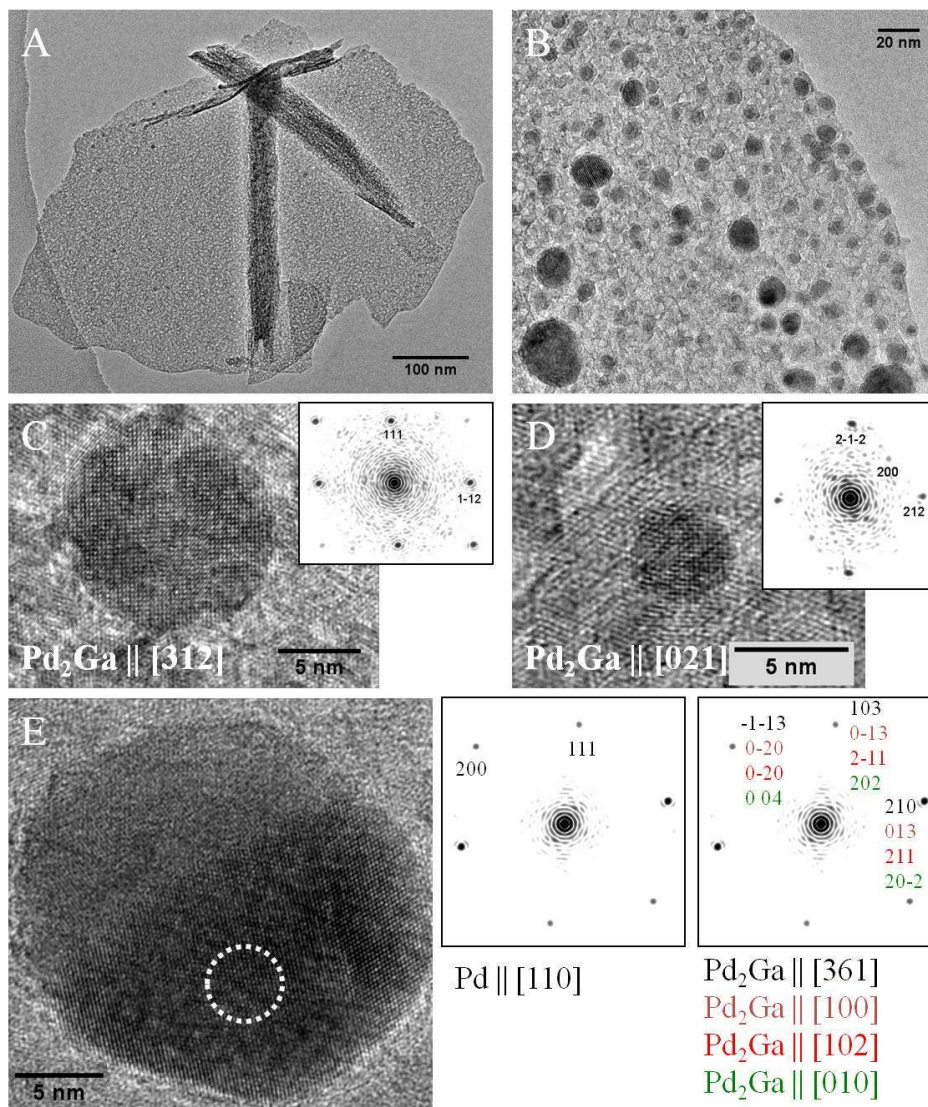
Figure 3- 8: (A+B) Overview micrographs, (C+D) HRTEM of Pd$_2$Ga10 with corresponding
FFT pattern after reduction at 773 K. Micrograph E demonstrates the structural similarity of Pd
and Pd$_2$Ga.

As depicted in Figure 3- 8, the reduction of Pd10 at 773 K yield metallic particles supported on an oxide matrix. The platelet-like morphology is maintained upon decomposition and reduction (Figure 3- 8A). XRD and HRTEM analysis reveal that the oxide support consists of MgO and MgGa$_2$O$_4$ spinel (Figure S3- 4). In some HRTEM images (Figure 3- 8C+D), the metallic phase is unambiguously identified as Pd$_2$Ga. In certain orientation and for lower Pd loadings, however, the phase identification is ambiguous due to small and highly defective particles. An assignment of the obtained lattice fringes to either Pd or Pd$_2$Ga is further complicated by the fact that different crystallographic orientations of the two structures lead to similar lattice fringe images with closely matching lattice spacing and angles between sets of lattice planes. Figure 3- 8 C and D show two cases where particles are oriented such that an assignment can only be made to the [321] and [021] orientation of the intermetallic phase, respectively. In contrast, there are at least four different orientations of the Pd$_2$Ga structure for which the obtained lattice fringes and the corresponding FFT power spectra are similar to the case of Pd particles oriented along the [110] zone axis, as shown in Figure 3- 8E. Due to the small size of the particles and the presence of defects, the intensities of the spots in the power spectra also deviate from the theoretical values. Therefore, it is not easy from the analysis of the electron diffraction patterns to exclude the presence of Pd particles.
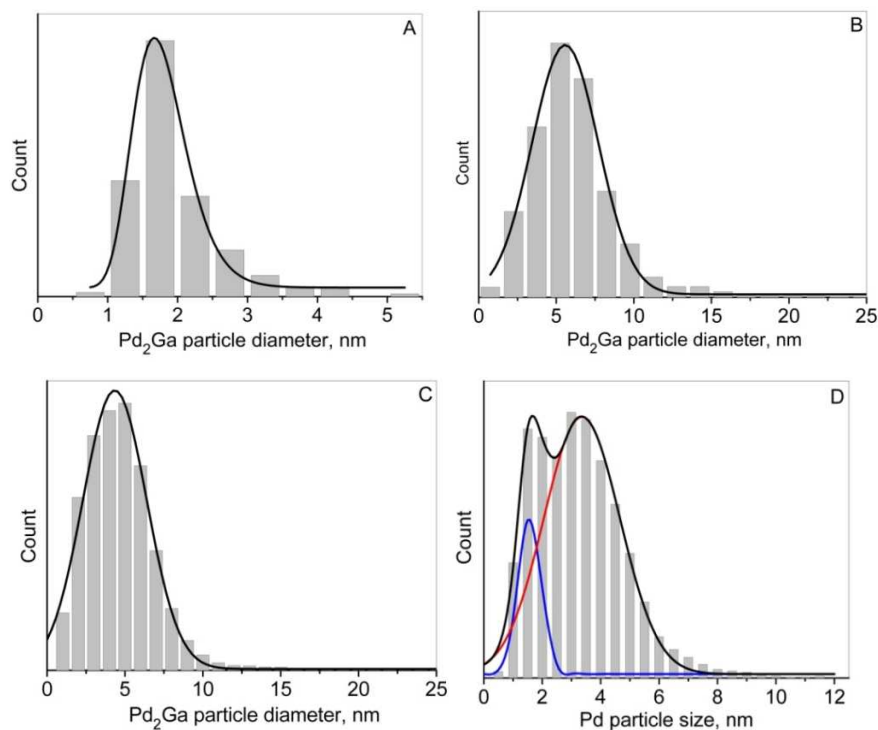
Figure 3- 9: Particle size distribution of (A) Pd05 (B) Pd10 and (C) Pd25 after HTR (773 K). (D) Pd25 after LTR (473 K).

The determined average particle sizes for Pd$_2$Ga 05, 10 and 25 are 1.8, 6.1 and 4.8 nm, respectively. Monomodal particle size distributions are obtained with narrow particle sizes, as presented in Figure 3- 9. Furthermore, the surface of the nanoparticles is often covered by a partially ordered layer.

To exclude that oxidation of Pd$_2$Ga in air was the origin of the oxide shells, Pd$_2$Ga25 was investigated without air exposure. Nevertheless, uniform overlayers around the intermetallic particles are observed as shown in Figure 3- 10. These shells are identified either as cubic Ga$_2$O$_3$ (γ-phase), MgGa$_2$O$_4$ or other Pd$_x$Ga$_y$ phases on basis of lattice fringes, while Pd, PdO and MgO are excluded. Surface coverage of noble metals is often associated with reducible supports and is widely discussed in terms of strong-metal support interaction (SMSI). SMSI influences the chemisorption properties of the metal depending on the reduction temperature.[33, 34] Full access to metal surface is only possible at low reduction temperature while at high temperature the chemisorption capability is heavily disturbed by oxide encapsulation.[35] This phenomenon is reversible, i.e. re-oxidation and mild reduction allows the catalyst to recover the original chemisorption capacity. Therefore, the morphology of Pd25 was also studied after LTR at 473 K (Figure 3- 11). According to the XANES spectrum, Pd$_2$Ga has not yet been formed at that temperature. Careful investigation of the electron diffraction pattern confirms that the main crystallographic phase is metallic Pd, as shown in Figure 3- 11C. The Pd particles show a bimodal size distribution (Figure 3- 9D). A minor fraction exhibits an average size of 1.6 nm, while for the larger fraction the particles size is 3.3 nm. It is supposed that the smaller particles originate from Pd^{2+} which is incorporated into the HTlc layers and the larger ones from segregated PdO-like Pd^{2+}. Upon temperature increase to 773 K the particles grow at the expanse of the smaller ones and result in an average particle size of 4.8 nm. Furthermore, particle encapsulation and core-shell structures were also observed upon reduction to 473 K as illustrated in Figure 3- 11B. The encircled areas in Figure 3- 11A are identified as crystalline MgGa$_2$O$_4$ spinel that is formed in addition to amorphous spinel phase and MgO upon reduction.
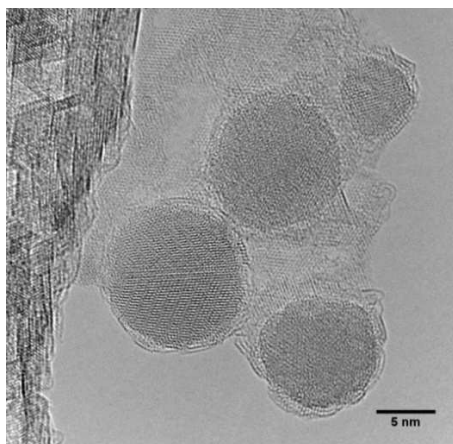
Figure 3- 10: HRTEM images of Pd$_2$Ga25 without air contact.
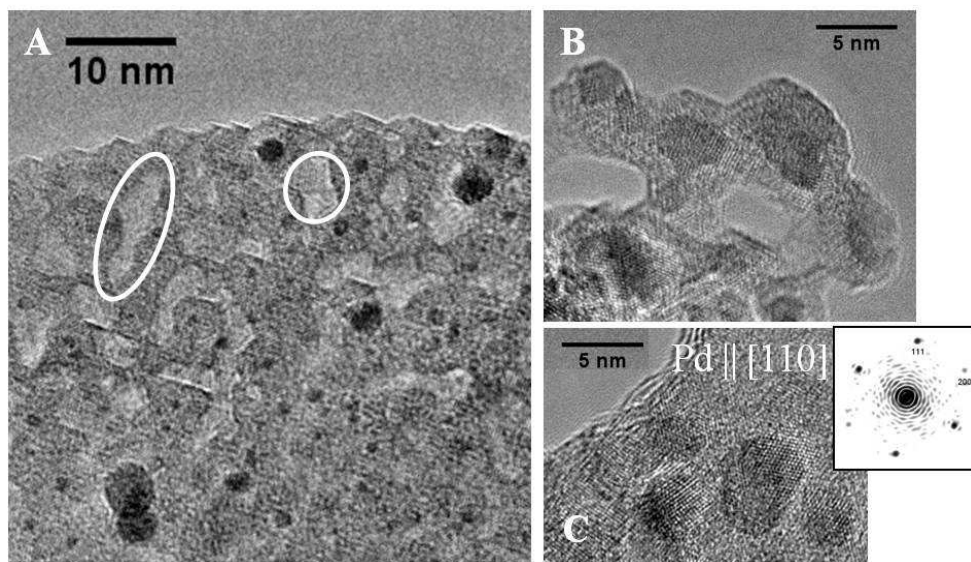
Figure 3- 11: (A) Overview micrographs, (B, C) HRTEM of Pd25 after LTR (473 K) and corresponding FFT pattern.

According to the XANES spectrum, Pd$_2$Ga has not yet been formed at that temperature. The particles show a bimodal size distribution (Figure 3- 9D). A minor fraction with an average size of 1.6 nm and a larger fraction with 3.3 nm coexist. It is supposed that the smaller particles originate from Pd^{2+} which was incorporated into the HTlc layers and the larger ones from segregated PdO-like Pd. Upon temperature increase the particle size further increased to 4.8 nm and the different origin of the two types of Pd cannot be discriminated. Furthermore, distinctive core shell structures were also observed upon reduction to 200 °C as illustrated in Figure 3- 11.

These shells are probably related to the synthesis approach rather than to SMSI state that should not be formed at that temperature. Moreover, partial embedment of the Pd particles can serve as an explanation for the core-shell structures.

In summary, TEM analysis was applied to determine the Pd phase and give estimation of the particle size. A reduction temperature of 473 K leads to bimodal distribution of metallic Pd, which is explained by the partial incorporation of Pd^{2+} in the HTlc precursor. Monomodal particle size distributions have been obtained for samples reduced at 773 K. The particle size of Pd$_2$Ga could be controlled by Pd loading to a certain extent and varies from 2 to 6 nm. Furthermore, the appearance of surface covering is noticed indicating a SMSI state of the catalysts.

3.3.4 IR characterization of supported Pd$_2$Ga nanoparticles during exposure to CO

In this section the adsorption properties of the Pd phases obtained after low and high temperature reduction as well as the interaction of CO with the oxide support are presented.

The spectra exhibited in Figure 3- 12 display characteristic bands in the carbonyl region of 2100 - 2000 cm^{-1} and 1970 - 1800 cm^{-1}. These bands are typical for linearly and multiply-bonded CO on metallic Pd surfaces, respectively.[36] It is noted that at CO pressures above 1 mbar the gas phase rotational bands of CO are resolved in the spectra. As already mentioned, reduction of the PdMgGa HTlc precursors at 473 K results in metallic Pd particles. CO adsorption at RT and a pressure of 50 mbar lead to population of on-top (2074 cm^{-1}), 2-fold bridging (1983 cm^{-1}) and 3-fold hollow sites (1896 cm^{-1}) on Pd^0 (Figure 3- 12A). A coverage dependent shift was observed for all bands ($\Delta \upsilon = +25$ cm^{-1}) due to increased dipole-dipole coupling. Additionally, a sharp band at 2016 cm^{-1} emerged during CO exposure at elevated pressures above 1 mbar. According to literature, it is either related to carbidic areas of the Pd sites due to CO disproportionation [37] or attributed to isolated Pd sites, whose electronic properties are modified by interaction with basic support species.[38]
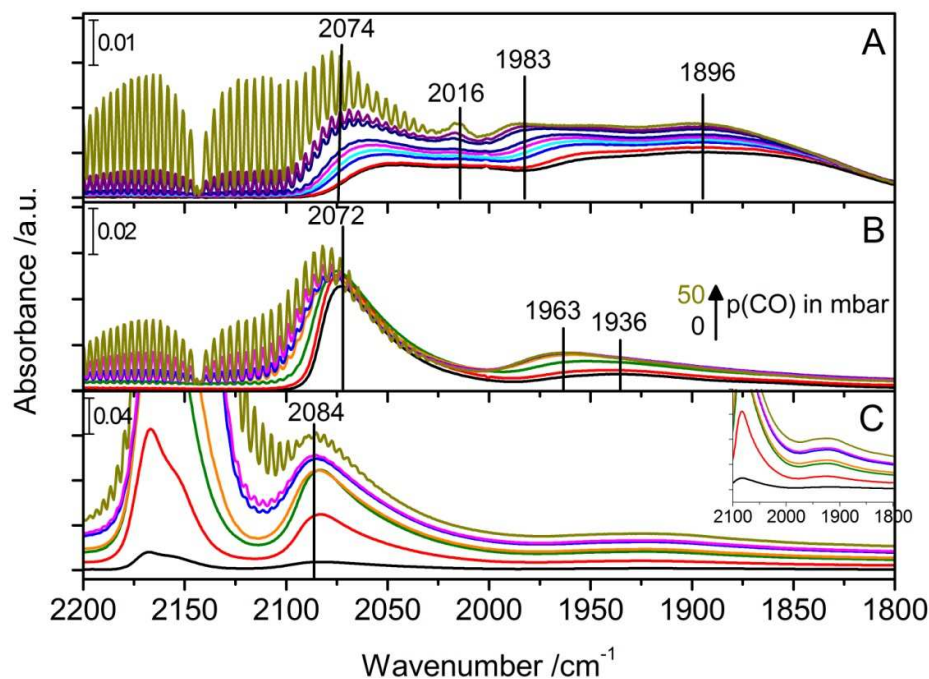
Figure 3- 12: IR spectra of CO adsorbed on Pd10 after LTR (A; 473 K) and HTR (B; 773 K) at RT, and after HTR at 77 K (C) in the CO stretching region from 2200 - 1800 cm^{-1}. (IR bands above 2100 cm^{-1} are due to physisorbed CO.)

High temperature reduction at 773 K modifies the ratio of multiply-bonded to linearly adsorbed CO on Pd–Ga surfaces as shown in Figure 3- 12B and C. The spectra clearly indicate an isolation of the adsorption sites presumably due to the increased Pd-Pd interatomic distances in Pd$_2$Ga compared to Pd metal. At RT adsorption (Figure 3- 12B) and low CO pressure predominantly on-top coordinated CO (2072 cm^{-1}) is present with only a weak band due to multiply-bonded CO at 1936 cm^{-1}. With increasing pressure the latter band grows and shifts to 1963 cm^{-1}. In contrast, CO adsorption at 77K prevails one predominant band at 2084 cm^{-1} and no change of the band due to multiply-bonded CO even at increased CO pressures was observed (Figure 3- 12C).
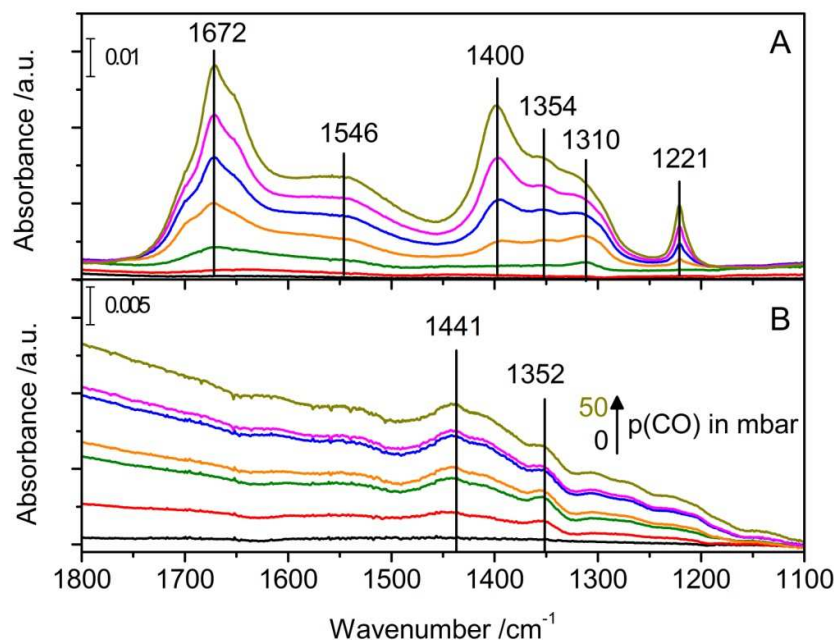
Figure 3- 13: IR spectra of CO adsorbed on Pd₂Ga10 in the carbonate region CO from 1800 - 1100 cm⁻¹ at RT (A) and 77 K (B).

While at low temperature CO is mostly unreactive and only small amounts of monodentate and bicarbonate carbonates were formed in the carbonate region (1700 - 1200 cm⁻¹), pronounced formation is observed at room temperature (Figure 3- 13). The signals located at 1650, 1546 and 1340 are ascribed to $\upsilon_{as}(CO_3^{2-})$ and $\upsilon_s(CO_3^{2-})$ modes of mono- and bidentate carbonate species. The more intense bands, located at 1671, 1400 and 1221 cm⁻¹, are assigned to $\upsilon_{as}(CO_3^{2-})$, $\upsilon_{sy}(CO_3^{2-})$ and $\delta(OH)$ modes, respectively, of surface bicarbonate species (HCO_3^-).[39, 40] The formation of different carbonate species can be either related to CO dissociation/ disproportionation (2 CO → CO₂ + C) [37, 40] or direct reaction of CO with hydroxyl groups on the surface to CO₂ (CO + OH → CO₂ + ½ H₂) [41]. The CO₂ formed further reacts with O²⁻ or OH groups of the support to form carbonate and bicarbonate. For our samples, the observed changes in the OH stretching suggest the reaction of CO with hydroxyl groups instead of CO disproportionation. Water evolution due to the release of hydrogen (3346 cm⁻¹) and bicarbonate formation (3621 cm⁻¹) occurred simultaneously (Figure S3- 5). The absence of the bridge-bonded band at 77 K suggests that carbonate (and water) formation and the population of an additional adsorption site due to the presence of metallic Pd are strongly correlated with each other. The formation of metallic Pd was also observed for Pd₂Ga samples after air exposure or pretreatment at insufficient high reduction temperature. Increasing the reduction temperatures and longer reduction periods have shown to minimize the contribution of bridged-bonded

carbonyl band and re-form the intermetallic surface (data not shown). We thus conclude that CO at sufficient temperature and pressure reacts with the surface of Pd$_2$Ga/MgO/MgGa$_2$O$_4$. This dynamic response of the surface to CO leads to partial decomposition of the intermetallic surface and formation of Pd0 as indicated by the appearance of multiply-bonded CO adsorbates. Our observations are in agreement with results reported by Haghofer et al. [42]. Initially isolated adsorption sites on the Pd$_2$Ga surface responds to CO exposure in a way that suggests an (at least partial) breakup of the intermetallic compound into surface regions containing metallic Pd. Although carbon monoxide itself is a reducing gas, it clearly induces some modification of intermetallic phase and support. Hence, we assume that dynamic changes of the oxide support (carbonate and water formation) in combination with the high oxophilicity of gallium give rise to the partial decomposition of Pd$_2$Ga nanoparticles into finely dispersed Pd and oxidized Ga.
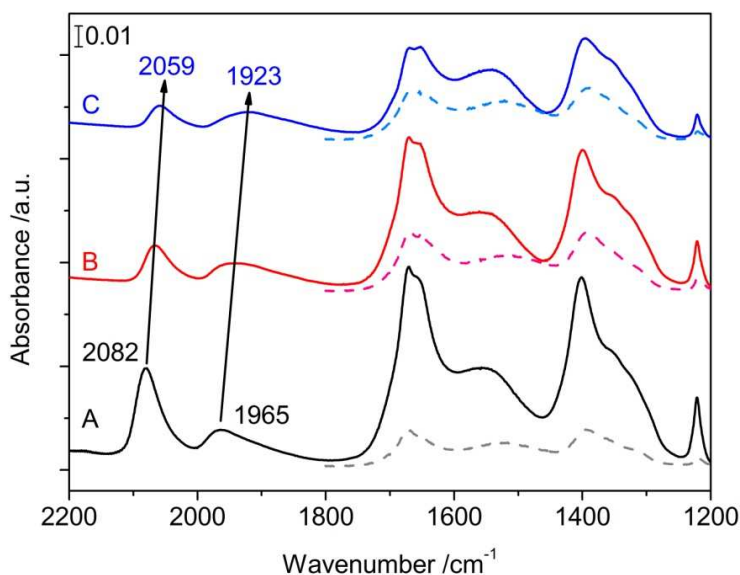
Figure 3- 14: IR spectra of Pd$_2$Ga0 (dotted) and Pd$_2$Ga10 (straight line) after CO adsorption at RT upon evacuation: A) p_{CO} = 50mbar, t = 30 min; B) p = 1.1·10^{-5} mbar; C) p = 3.9·10^{-6} mbar.

Furthermore, the desorption process of CO was examined particularly with regard to determination of the active metal surface by CO chemisorption. The recorded spectra obtained after CO adsorption at a CO pressure of 50 mbar (t = 30 min) and during evacuation to a pressure of 10^{-6} mbar are presented in Figure 3- 14. The bands of linearly and bridged-bonded CO on Pd^0 are shifted to lower wavenumbers upon evacuation and the overall intensity decreased significantly. After complete evacuation the intensity ratio of the bands is nearly equal and typical for metallic Pd rather than Pd$_2$Ga. Additionally, the formed carbonates and

bicarbonates species during CO adsorption are preserved. Same behavior was also found to minor extent for the Pd free sample (Figure 3- 14, dotted lines). Consequently, we assume that major contribution of the irreversible chemisorbed CO is attributed to metallic Pd and the oxide support. The intermetallic Pd$_2$Ga surface only weakly adsorbs CO and decomposes in reactive atmosphere like CO. These observations clearly complicate the interpretation of volumetric CO chemisorption data (Figure S3- 6).

In summary, CO-IR adsorption measurements highlight the presence of isolated adsorption sites by formation of intermetallic Pd$_2$Ga nanoparticles. While at 77 K only one distinctive carbonyl band at 2080 cm^{-1} is formed and no spectral changes were observed with increasing CO coverage, the Pd$_2$Ga surface is apparently instable in CO at RT. This is indicated by the population of a second adsorption site at 1963 cm^{-1}, which is typically observed for Pd metal. It suggests that Pd$_2$Ga nanoparticles are highly reactive towards different gas atmosphere in contrast to the bulk model catalysts due to an increased number of surface atoms by the nanostructuring. CO exposure of surface lead to partial the oxidation of metallic Ga, probably by oxidizing species (CO$_2$ and H$_2$O) originating from the interaction of CO with the support material, and the formation metallic Pd on Pd$_2$Ga surface.

3.3.5   Catalytic performance

In this part the catalytic experiments, which were performed in order to understand catalyst behavior and its activation process at a reaction temperature of 473 K, will be presented and discussed. Before the catalytic measurements the HTlc precursor was reduced in-situ in 5% H$_2$/Ar at low (473 K) and high reduction temperature (773 K).

In Figure 3- 15 the acetylene conversion and ethylene selectivities for all experiments are presented over time on stream (TOS). A different catalytic performance was obtained depending on the reduction temperature. Low reduction temperature yields a catalyst which slowly deactivates over TOS (Figure 3- 15A), probably because of the formation carbonaceous deposits originating from the feed gas.[12] The selectivity towards the desired semi-hydrogenation product is relatively stable at only 26% after 22 h TOS. As it was already shown by TEM, XANES and IR spectroscopy, a reduction temperature of 473 K is not sufficient to form the intermetallic compound. Accordingly, the catalytic properties – low selectivity and stability – are representative of pure Pd rather than that of the Pd$_2$Ga intermetallic compound.
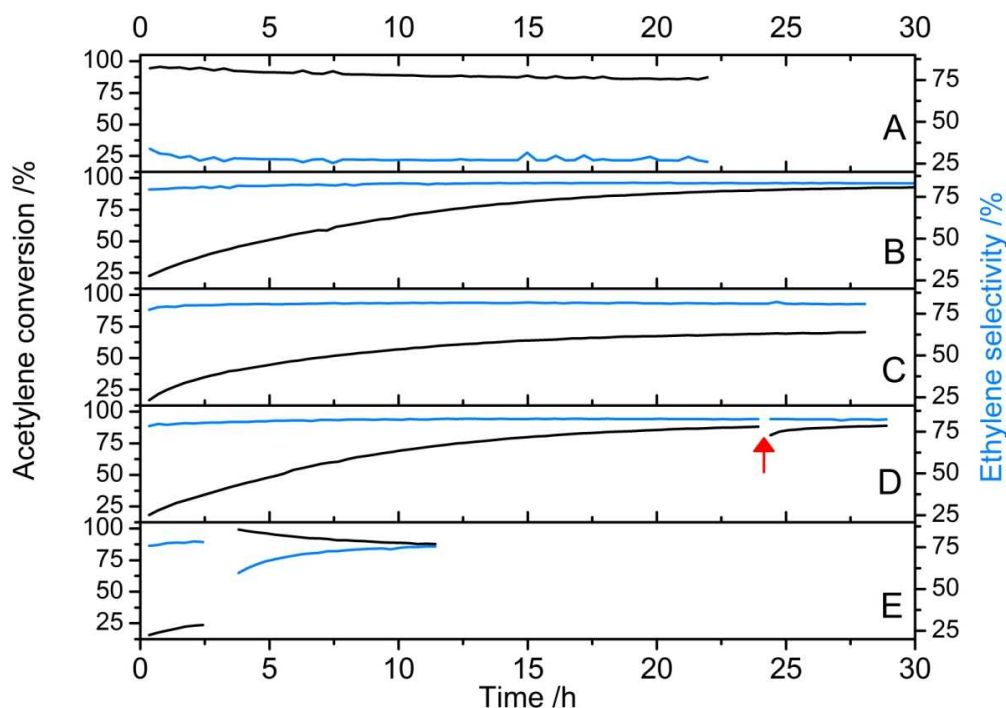
Figure 3- 15: Acetylene conversion and ethylene selectivity at 473 K over (A) Pd25 reduced at 473 K, (B) Pd$_2$Ga25 reduced at 773 K, (C) Pd$_2$Ga25 and activation in 5 Vol% H$_2$/Ar at 473 K, (D) Pd$_2$Ga25 and O$_2$ pulse after 24 h TOS (arrow), (E) Pd$_2$Ga25 and oxidative treatment after 2.5 h TOS at 473 K for 40 min.

If a reduction temperature of 773 K was applied (HTR), which according to TEM, XANES and IR spectroscopy is sufficient to create Pd$_2$Ga nanoparticles, a remarkable change in the catalytic properties is obtained (Figure 3- 15B). As reported previously [8], a slow and pronounced activation from 22 to 94 % conversion is observed within the first 30 h TOS. After 44 h TOS the ethylene selectivity account 80%, while the selectivities to C$_2$H$_6$, C$_4$ and C$_6$ hydrocarbons are each below 10%, as shown in Figure 3- 16. Interestingly, only slight changes in the selectivity are observed during the activation.
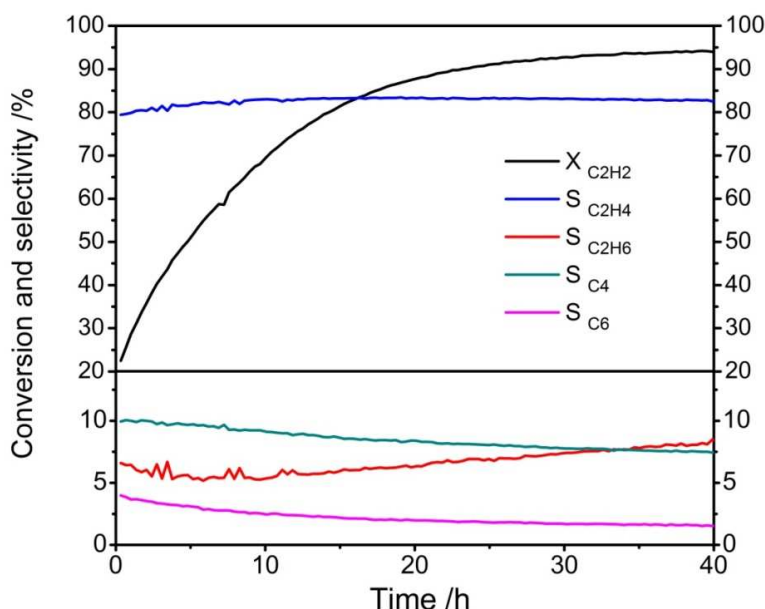
Figure 3- 16: Conversion and selectivities at 473 K over Pd$_2$Ga25 after HTR (100ml/min flow, 0.2 mg Pd25).

In principle, two different explanations will be discussed in the following. Corresponding models of the active state of the nanostructured Pd$_2$Ga catalyst are schematically shown in Figure 3- 17. Model I is only related to an increased accessibility of the intermetallic surface, while Model II includes changes in the nature of the active sites as well as modifications by the feed gas. The fundamental difference of both models is, that according to Model I the intermetallic surface is the catalytically active sate, while in Model II the decomposition product if the intermetallic compound is active.

Model I refers to the SMSI state of the catalyst that causes partial blocking of the active surface and was detected by TEM after HTR. The removal of the oxide shell formed at HTR can be triggered by re-oxidation [33], but also a lower reduction potential by decreasing the temperature from 773 K (reduction) to 473 K (reaction) might be sufficient to slowly reverse the SMSI state. The catalyst after HTR was pretreated in 5% H$_2$/Ar for 16 h at reaction temperature (473 K) to check if the activation occurs with time also under more mild reducing conditions in the absence of the reactant feed. The corresponding reaction profile of the pretreated sample is shown in Figure 3- 15C. No significant differences of the activation process are observed in comparison to profile B. The activation time is comparable to that of the catalyst without any pretreatment after reduction. Thus, either the SMSI state has not been reversed because of the different redox potentials of the 5% H$_2$/Ar stream and the 1%C$_2$H$_2$/15%H$_2$/30%C$_2$H$_4$ reaction mixture or the activation process is caused by another modification of the Pd$_2$Ga surface in the feed gas.
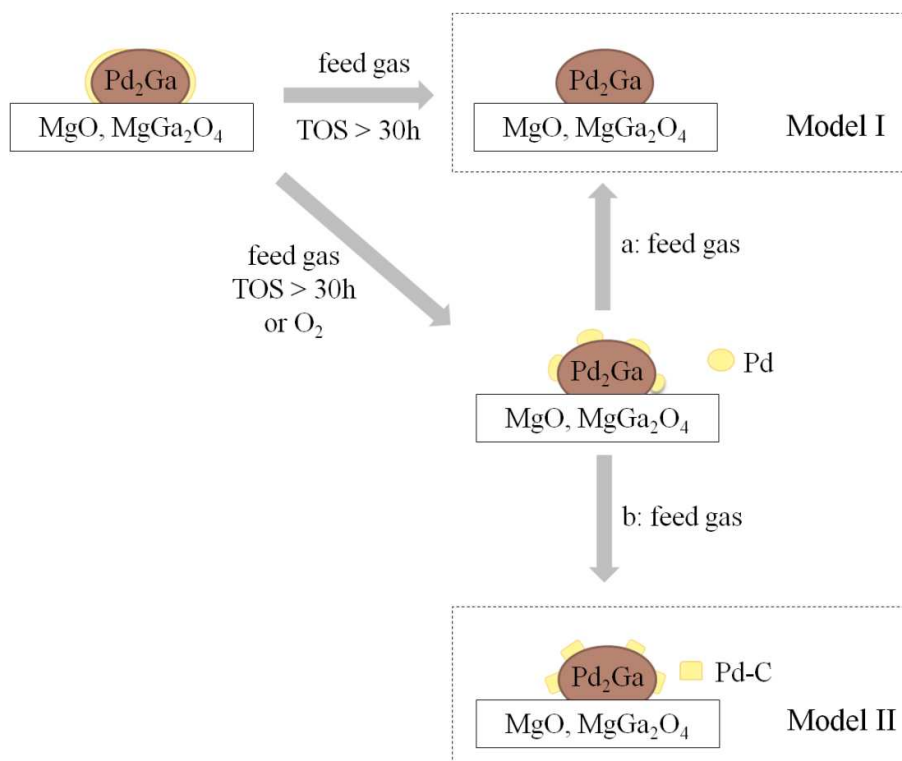
Figure 3- 17: Schematic models explaining the activation process during the selective hydrogenation of acetylene.

According to the IR results, the decomposition of the intermetallic compound into metallic Pd and oxidized Ga is responsible for the slow activation behavior of the catalyst. This segregation is represented in Model II. Under reaction conditions, the required oxygen may come from O-containing impurities in the feed gas or from the support, similar as discussed for CO adsorption at room temperature. The increase in activity might be explained by the formation of highly reactive, metallic Pd patches on the particle surface as reported for larger Pd$_2$Ga particles during methanol steam reforming.[42] Model II also assumes that the ethylene selectivity of the less active initial Pd$_2$Ga surface measured at low conversion and that of the more active, metallic Pd particles at higher conversion must be coincidently equal. The metallic Pd particles resulting from decomposition are most likely very small. Therefore hydride formation, which is known to be size-dependent [12] and was shown to be responsible for the unselective hydrogenation of alkynes [43, 44], will probably not occur. Thus, the newly formed Pd^0 particles might be highly selective due to their small size. On the other hand a transformation into a PdC$_x$ phase is a possible explanation for the high selectivity of the decomposed surface.[45] Small palladium particles have a larger tendency to form the PdC$_x$ phase [46] by the fragmentation of the reactant molecules under the reaction conditions, which also hinders subsurface hydride formation.

Neither hydride nor carbon formation were observed for bulk Pd-Ga intermetallic compounds [47, 48], but may play a role for the nanostructured Pd$_2$Ga compound, which are more reactive due to the increased number of surface atoms or tend to decompose as suggested by Model II.

In order to investigate the activated state of the catalyst, 50 mg of undiluted Pd25 precursor were reduced in-situ and activated in 150 ml/min feed gas flow for 44 h TOS. TEM analysis of this sample was done without air contact in order to keep the metallic state of the particles. Micrographs with different magnifications are presented in Figure 3- 18. Phase identification on basis of the lattice fringes suggests that the intermetallic Pd$_2$Ga phase is preserved in the bulk of the nanoparticles during activation (Figure 3- 18C). The particles exhibit contrast fluctuations in the Scanning TEM images, indicative of an inner inhomogeneity (Figure 3- 18D). Different types of material which differ in their Z-contrast seem to have segregated supporting the partial surface decomposition of the Pd$_2$Ga IMC into a metallic and an oxidic species during activation, as suggested by Model II. Unfortunately, it was not possible to identify the involved phases that are the origin of the contrast fluctuations.
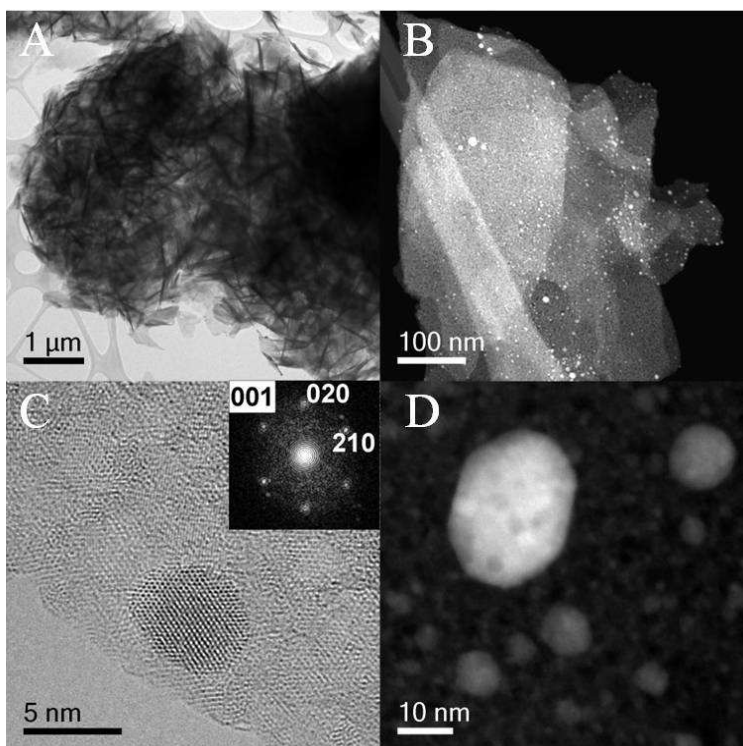
Figure 3- 18: (A) TEM overview micrograph; (B+D) STEM images; (C) HRTEM micrographs (with FFT pattern of Pd$_2$Ga along (110) zone axis) of post-reacted Pd$_2$Ga25 catalyst after 44 h TOS.

No indication for formation of amorphous carbon is found. The absence is also confirmed by Raman spectroscopy, which shows no characteristic bands for amorphous carbon. Before and after reaction no significant change in the spectra is observed (Figure S3- 7). Furthermore, a temperature programmed oxidation was performed by TG-DSC-MS. An exothermic mass loss of 3% that was associated with CO_2 formation is observed up to a temperature of 773 K (Figure S3- 8). This corresponds to an amount of 6 µmol of carbon. In the light that changes in the catalytic properties of Pd catalysts by carbonaceous deposits are reported typically to promote the selectivity rather than the activity in hydrogenation reactions [49], they are excluded as reason for the catalyst activation.

As the Pd$_2$Ga surface is known to be oxygen sensitive [42], the role of oxygen addition was studied (Figure 3- 15D, E). In the first experiment the catalyst was exposed to three pulses of O_2 (each 10 µmol) after activation in feed for 24 h at 473 K (Figure 3- 15D, indicated by red arrow). The unperturbed catalytic performance suggests that either the intermetallic surface has already been completely decomposed during the activation and cannot react any further with gas phase oxygen (Model II), or that reducing potential of the feed gas at 473 K is sufficient to instantaneously clean the surface again and re-form the oxygen-free state of the intermetallic surface (Model I). The catalyst was also exposed to three O_2 pulses directly after reduction and before switching to the reaction feed at 473 K. No significant impact on the catalytic performance was observed at the beginning of the activation period (Figure 3- 15E), which confirms a certain stability of the surface against low amounts of oxygen. After 2.5 h TOS, the catalyst was treated in a 5% O_2/He flow for 40 min at 473 K. This treatment is estimated to be harsh enough to trigger an oxidative surface decomposition of the intermetallic surface. As illustrated in Figure 3- 15E by this treatment the catalyst is transformed into a more active state. However, compared to the state obtained after prolonged TOS, the selectivity is initially considerably lowered. This is likely a result of the presence of highly active metallic, which has formed from the IMC decomposition. Due to the lower intrinsic selectivity of monometallic Pd and/or as a consequence of 100% conversion the selectivity is decreased. It fully recovers to the original value of 80% within the following 7.5 h TOS, while the conversion drops again to a similar level as observed in the other experiments. This result shows that another dynamic process has been triggered by the O_2 treatment, which is faster than the activation in the feed, but finally leads to the same catalytic performance. The effect of O_2 treatment can be explained by both models, the oxidative reversal of the SMSI state with subsequent self-cleaning of the intermetallic surface in the feed (Model I) as well as the accelerated oxidative decomposition, which leads to formation of a different active state, that can undergo further transformation in the feed (Model II). Two pathways are possible for such transformation under reaction

condition, as shown in Model II (a, b in Figure 3- 17). Either the evolving metallic Pd patches
on the Pd$_2$Ga particles are unique and selective, e.g. due to their small particle size (a) or the
dispersed Pd patches undergo a slow transformation to a Pd-C phase (b).
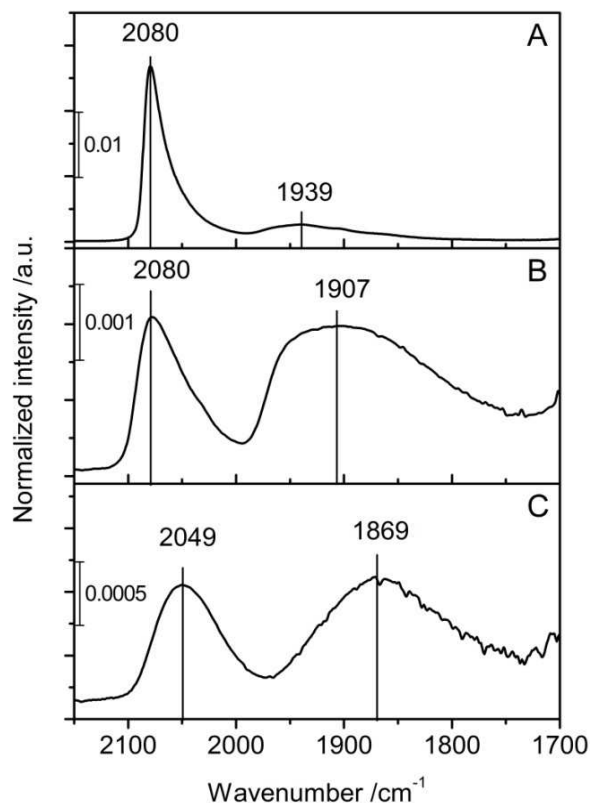
Figure 3- 19: CO-IR adsorption spectra of (A) Pd$_2$Ga25 after HTR for 4 h; (B) after subsequent
treatment in O$_2$ (5 Vol%, 30 min, 473 K) and H$_2$ (200 mbar, 2 h, 473 K); (C) after subsequent
treatment in O$_2$ (5 Vol%, 30 min, 473 K) and H$_2$/C$_2$H$_2$/C$_2$H$_4$ mixture (10 mbar, 7h, 473 K).
(The shown spectra were recorded at a CO pressure of 0.08 mbar.)

By means of CO-IR spectroscopy, a catalyst which was treated in oxygen for 30 min at 473 K
was studied. Figure 3- 19A shows the IR spectra of adsorbed CO of the fresh Pd$_2$Ga catalyst
directly after HTR with primarily on-top coordinated CO. After O$_2$ treatment and a subsequent
reduction in H$_2$ (Figure 3- 19B) and in feed gas (Figure 3- 19C) at 473 K characteristic bands of
linearly and multiply-bonded CO are present. This increased contribution of multiply-bonded
CO supports the decomposition of Pd$_2$Ga to metallic Pd upon O$_2$ treatment and the re-formation
of the intermetallic state in the feed can be excluded. Furthermore, compared to the spectrum
obtained after H$_2$ reduction which is typically of monometallic Pd, spectrum of the sample, that

was activated 7 h in the feed gas, is shifted to lower wavenumbers ($\Delta \upsilon$ = -31 cm^{-1}) and the band shape changes. This is an indication that the Pd patches formed by the decomposition process undergo a further transformation in the feed and favors Model IIb, i.e. formation of a highly selective PdC$_x$ phase. The exposure to reaction feed, which was sufficient to reach the active state in the catalytic measurements, was not sufficient to the re-form the intermetallic state, as shown in Figure 3- 19A.

In summary, the supported nano-Pd$_2$Ga catalyst obtained after high temperature reduction at 773 K show slow activation in the feed gas. Alternatively, activation in oxidative atmosphere can enhance the reactivity. In both cases, a highly selective, active and stable catalyst can be obtained. Excluding carbon deposits as the reason for this behavior, the results are consistent with two possible explanations for the activation. The first is the removal of surface coverage formed due to the SMSI effect at high reduction temperature. Secondly, similar to the dynamic processes occurring in CO atmosphere, the instability of the Pd$_2$Ga surface, induced by the reaction atmosphere (C$_2$H$_2$, C$_2$H$_4$, dissociated H or O$_2$), lead the partial decomposition to metallic Pd and formation of new very active and selective sites for hydrogenation. While we cannot unambiguously exclude the one or the other model, the data presented seems to favor the decomposition of Pd$_2$Ga with subsequent in-situ formation of PdC$_x$-sites.

3.4 Conclusions

Supported nanoparticles of the intermetallic compound Pd$_2$Ga with a monomodal and narrow particle size distribution can be prepared by decomposition of Hydrotalcite-like PdMgGa precursors in reducing atmosphere at 773 K. The size of the nanoparticles (2 - 6 nm) and the amount of Pd^{2+} initially incorporated in the Hydrotalcite lattice can be controlled by varying the Pd loading. Pd^{2+} incorporation was evidenced by a combined XANES and TPR study and a critical limit to avoid segregation was found around 1 mol% Pd.

The resulting nano-Pd$_2$Ga/MgO/MgGa$_2$O$_4$ materials exhibit a large specific surface area (100 - 120 m^{2}g^{-1}) rendering them to promising catalytic materials. IR spectroscopy of chemisorbed CO revealed different adsorptive properties of the nano-Pd$_2$Ga phase compared to nano-Pd^0 formed from the same precursor by reduction at lower temperature. Accordingly, the catalytic properties in semi-hydrogenation of acetylene were found to be superior after high reduction temperature and highly selective, active and stable catalysts have been obtained. A final stable state of the catalysts was only achieved after long activation with time on stream or after oxidative pre-treatment. These dynamics of the Pd$_2$Ga nanoparticles are related to an interplay of surface

decomposition into Pd^0 and Ga_2O_3 in reactive gas atmosphere, which was also observed by IR spectroscopy in CO atmosphere, and strong metal support interaction between Pd_2Ga nanoparticles and the $MgO·Ga_2O_3$ support. The active state of the final catalyst is attributed to a Pd_2Ga core - Pd/PdC_x shell configuration.

This study has shown that the Pd-based intermetallic hydrogenation catalysts can be prepared in a feasible and controlled manner in a nanostructured form. The known catalytic properties of the bulk intermetallic phases have only apparently been conserved. Instead, a great complexity has been observed, which is related to surface dynamics in reactive atmospheres.

3.5 References

[1]   Sauthoff, *Intermetallics*, Wiley-VCH Verlag GmbH Weinheim, **1995**.
[2]   D. B. Miracle, *Acta Metallurgica et Materialia* **1993**, *41*, 649-684.
[3]   J. H. Westbrook, R. L. Fleischer, *Intermetallic Compounds, Vol. 4*, Chichester, **2000**.
[4]   G. E. R. Schulze, *Metallphysik*, Springer Verlag Wien New York, **1967**.
[5]   K. Kovnir, D. Teschner, M. Armbrüster, P. Schnörch, M. Hävecker, A. Knop-Gericke, Y. Grin, R. Schlögl, *Bessy Highlights 2007* **2008**, 22-23.
[6]   J. Osswald, K. Kovnir, M. Armbrüster, R. Giedigkeit, R. E. Jentoft, U. Wild, Y. Grin, R. Schlögl, *Journal of Catalysis* **2008**, *258*, 219-227.
[7]   K. Kovnir, J. Osswald, M. Armbrüster, R. Giedigkeit, T. Ressler, Y. Grin, R. Schlögl, in *Studies in Surface Science and Catalysis, Vol. Volume 162* (Eds.: M. D. D. E. D. V. S. H. P. A. J. J. A. M. E.M. Gaigneaux, P. Ruiz), Elsevier, **2006**, pp. 481-488.
[8]   A. Ota, M. Armbrüster, M. Behrens, D. Rosenthal, M. Friedrich, I. Kasatkin, F. Girgsdies, W. Zhang, R. Wagner, R. Schlögl, *The Journal of Physical Chemistry C* **2010**, *115*, 1368-1374.
[9]   K. Kovnir, M. Schmidt, C. Waurisch, M. Armbrüster, Y. Prots, Y. Grin, *Zeitschrift für Kristallographie NCS* **2008**, *223*, 7-8.
[10]   H. Okamoto, *Journal of Phase Equilibria and Diffusion* **2008**, *29*, 466-467.
[11]   M. Armbrüster, K. Kovnir, M. Behrens, D. Teschner, Y. Grin, R. Schlögl, *Journal of the American Chemical Society* **2010**, *132*, 14745-14747.
[12]   A. Borodziński, G. C. Bond, *Catalysis Reviews: Science and Engineering* **2006**, *48*, 91 - 144.
[13]   S. E. Collins, M. A. Baltanás, J. L. Garcia Fierro, A. L. Bonivardi, *Journal of Catalysis* **2002**, *211*, 252-264.
[14]   A. De Roy, *Molecular Crystals and Liquid Crystals Science and Technology. Section A. Molecular Crystals and Liquid Crystals* **1998**, *311*, 173 -193.
[15]   K. Takehira, T. Shishido, *Catalysis Surveys from Asia* **2007**, *11*, 1-30.
[16]   V. Rives, S. Kannan, *Journal of Materials Chemistry* **2000**, *10*, 489-495.
[17]   C. Gérardin, D. Kostadinova, B. Coq, D. Tichit, *Chemistry of Materials* **2008**, *20*, 2086-2094.
[18]   X. Duan, D. G. Evans, *Layered Double Hydroxides*, Springer-Verlag, Berlin, Heidelberg, **2006**.
[19]   C. Forano, T. Hibino, F. Leroux, C. Taviot-Gueho, in *Handbook of Clay Science* (Eds.: F. Bergaya, B. K. G. Theng, G. Lagaly), Elsevier, **2006**, pp. 1021-1095.
[20]   R. Shannon, *Acta Crystallographica Section A* **1976**, *32*, 751-767.
[21]   A. Ota, E. L. Kunkes, I. Kasatkin, E. Groppo, D. Ferri, B. Poceiro, R. M. N. Yerga, M. Behrens, *submitted to Journal of Catalysis*.
[22]   E. López-Salinas, M. García-Sánchez, M. L. Ramón-García, I. Schifter, *Journal of Porous Materials* **1996**, *3*, 169-174.
[23]   E. López-Salinas, M. García-Sánchez, J. A. Montoya, D. R. Acosta, J. A. Abasolo, I. Schifter, *Langmuir* **1997**, *13*, 4748-4753.
[24]   M. A. Aramendia, Y. Aviles, V. Borau, J. M. Luque, J. M. Marinas, J. R. Ruiz, F. J. Urbano, *Journal of Materials Chemistry* **1999**, *9*, 1603-1607.
[25]   N. N. Das, S. C. Srivastava, *Bulletin of Materials Science* **2002**, *25*, 283-289.
[26]   A. G. Christy, S. M. Clark, *Physical Review B* **1995**, *52*, 9259-9265.
[27]   G. Demazeau, I. Omeran, M. Pouchard, P. Hagenmuller, *Materials Research Bulletin* **1976**, *11*, 1449-1452.
[28]   S.-J. Kim, S. Lemaux, G. Demazeau, J.-Y. Kim, J.-H. Choy, *Journal of Materials Chemistry* **2002**, *12*, 995-1000.
[29]   A. Eyssler, P. Mandaliev, A. Winkler, P. Hug, O. Safonova, R. Figi, A. Weidenkaff, D. Ferri, *The Journal of Physical Chemistry C* **2010**, *114*, 4584-4594.

[30] F. Cavani, F. Trifirò, A. Vaccari, *Catalysis Today* **1991**, *11*, 173-301.
[31] W. Jochum, S. Penner, R. Kramer, K. Föttinger, G. Rupprechter, B. Klötzer, *Journal of Catalysis* **2008**, *256*, 278-286.
[32] N. Iwasa, N. Takezawa, *Topics in Catalysis* **2003**, *22*, 215-224.
[33] S. J. Tauster, S. C. Fung, R. L. Garten, *Journal of the American Chemical Society* **1978**, *100*, 170-175.
[34] S. J. Tauster, *Accounts of Chemical Research* **1987**, *20*, 389-394.
[35] M. Che, C. O. Bennet, *Advances in Catalysis, Vol. 36*, **1989**.
[36] N. Sheppard, C. De La Cruz, *Catalysis Today* **2001**, *70*, 3-13.
[37] S. Bertarione, D. Scarano, A. Zecchina, V. Johanek, J. Hoffmann, S. Schauermann, J. Libuda, G. Rupprechter, H. J. Freund, *Journal of Catalysis* **2004**, *223*, 64-73.
[38] F. Prinetto, M. Manzoli, G. Ghiotti, M. d. J. Martinez Ortiz, D. Tichit, B. Coq, *Journal of Catalysis* **2004**, *222*, 238-249.
[39] Y. Hao, M. Mihaylov, E. Ivanova, K. Hadjiivanov, H. Knözinger, B. C. Gates, *Journal of Catalysis* **2009**, *261*, 137-149.
[40] H. Borchert, B. Jürgens, V. Zielasek, G. Rupprechter, S. Giorgio, C. R. Henry, M. Bäumer, *Journal of Catalysis* **2007**, *247*, 145-154.
[41] K. Föttinger, R. SchlAgl, G. A. n. Rupprechter, *Chemical Communications* **2008**, 320-322.
[42] A. Haghofer, K. Föttinger, F. Girgsdies, D. Teschner, A. Knop-Gericke, R. Schlögl, G. Rupprechter, *Journal of Catalysis* **2012**, *286*, 13-21.
[43] D. Teschner, E. Vass, M. Hävecker, S. Zafeiratos, P. Schnörch, H. Sauer, A. Knop-Gericke, R. Schlögl, M. Chamam, A. Wootsch, A. S. Canning, J. J. Gamman, S. D. Jackson, J. McGregor, L. F. Gladden, *Journal of Catalysis* **2006**, *242*, 26-37.
[44] D. Teschner, J. Borsodi, A. Wootsch, Z. Révay, M. Hävecker, A. Knop-Gericke, S. D. Jackson, R. Schlögl, *Science* **2008**, *320*, 86-89.
[45] S. B. Ziemecki, G. A. Jones, D. G. Swartzfager, R. L. Harlow, J. Faber, *Journal of the American Chemical Society* **1985**, *107*, 4547-4548.
[46] A. Borodziński, G. C. Bond, *Catalysis Reviews: Science and Engineering* **2008**, *50*, 379 - 469.
[47] J. Osswald, R. Giedigkeit, R. E. Jentoft, M. Armbrüster, F. Girgsdies, K. Kovnir, T. Ressler, Y. Grin, R. Schlögl, *Journal of Catalysis* **2008**, *258*, 210-218.
[48] K. Kovnir, M. Armbruster, D. Teschner, T. V. Venkov, L. Szentmiklosi, F. C. Jentoft, A. Knop-Gericke, Y. Grin, R. Schlogl, *Surface Science* **2009**, *603*, 1784-1792.
[49] D. Teschner, Z. Revay, J. Borsodi, M. Havecker, A. Knop-Gericke, R. Schlogl, D. Milroy, S. D. Jackson, D. Torres, P. Sautet, *Angewandte Chemie-International Edition* **2008**, *47*, 9274-9278.

Supplementary Information

Sample identification

Label	FHI internal sample number	Label	FHI internal sample number
Pd0	11369	Pd_2Ga0	11754
Pd01	10198	Pd_2Ga01	12462
Pd03	10199	Pd_2Ga03	12419
Pd05	10200	Pd_2Ga05	12385
Pd08	10201	Pd_2Ga08	12423
Pd10	10230	Pd_2Ga10	11121
Pd15	10231	Pd_2Ga15	12390
Pd25	10232	Pd_2Ga25	11782
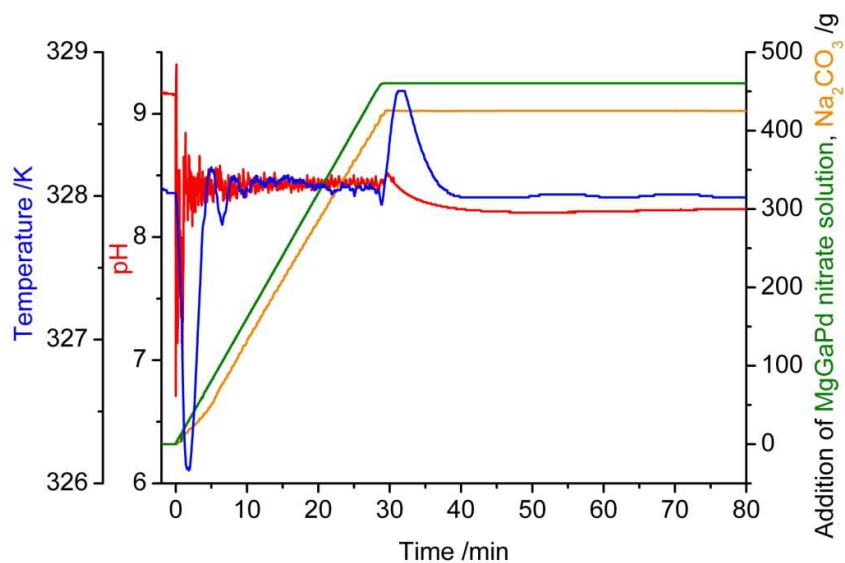
Figure S3- 1: Synthesis protocol of Pd15 HTlc precursor.
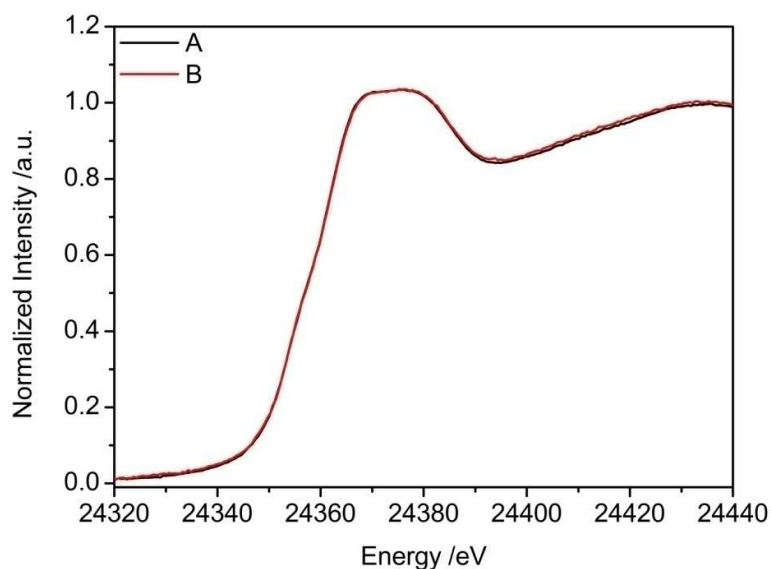
Figure S3- 2: XANES spectra of PdZnAl HTlc at RT in (A) Helium and (B) 5 Vol% H_2/He.

No change of the white line was observed upon feeding hydrogen over the PdZnAl HTlc reference sample with 1 mol% Pd at RT. This assumes that Pd^{2+} is completely incorporated into the HTlc lattice and not available for reduction at room temperature. Accordingly, no RTR H_2 consumption was observed- Thus, we conclude that PdZnAl HTlc can be used as reference for octahedrally coordinated Pd^{2+} in HTlc.

Synthesis:

PdZnAl HTlc were synthesized by controlled co-precipitation at pH = 8.5 and a temperature of 298 K by co-feeding appropriate amounts of mixed metal nitrate and mixed sodium hydroxide/sodium carbonate solutions(0.045 M Na_2CO_3 + 0.3 M NaOH). The following synthesis steps are equal to the herein presented synthesis protocol. The experimentally determined Pd:Zn:Al atomic ratio was 1:69.5:29.5.
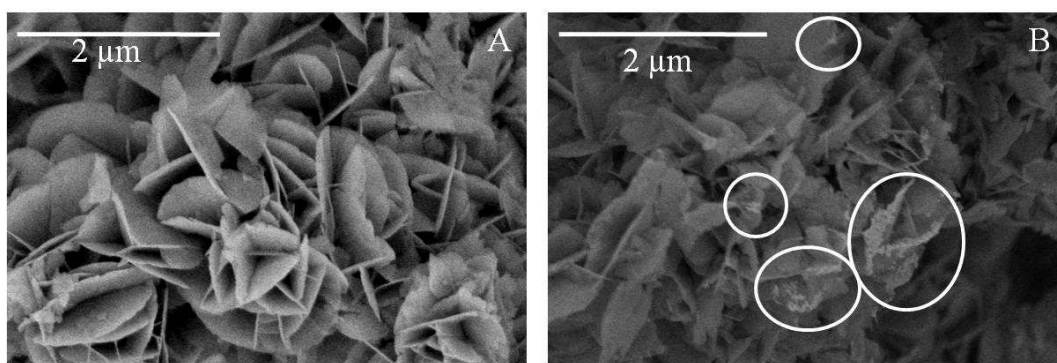
Figure S3- 3: BSE images of Pd10 (A) and Pd25 (B). Enhanced contrast allows the identification of Pd rich areas outside the platelets in the latter sample.
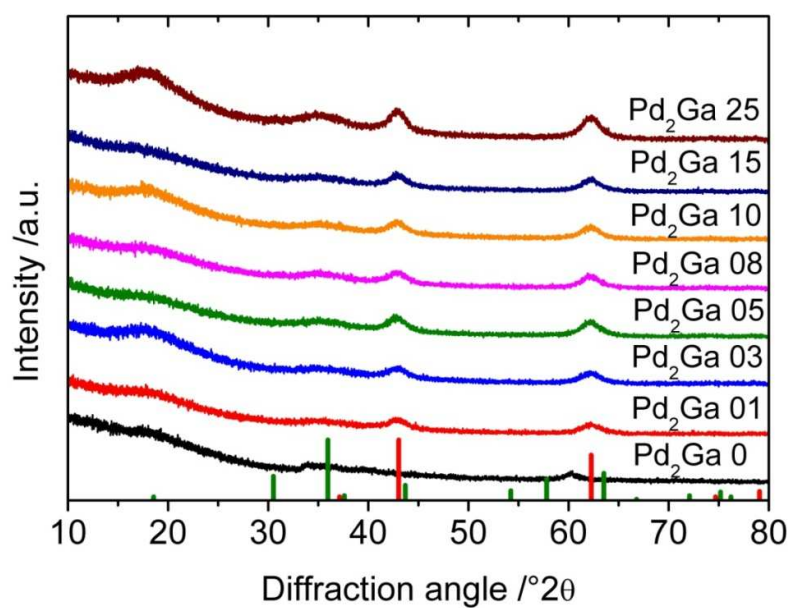
Figure S3- 4: Powder patterns of Pd_2Ga_x samples. Red column MgO (ICDD 1-1235) and black column $MgGa_2O_4$ (ICDD 10-113).
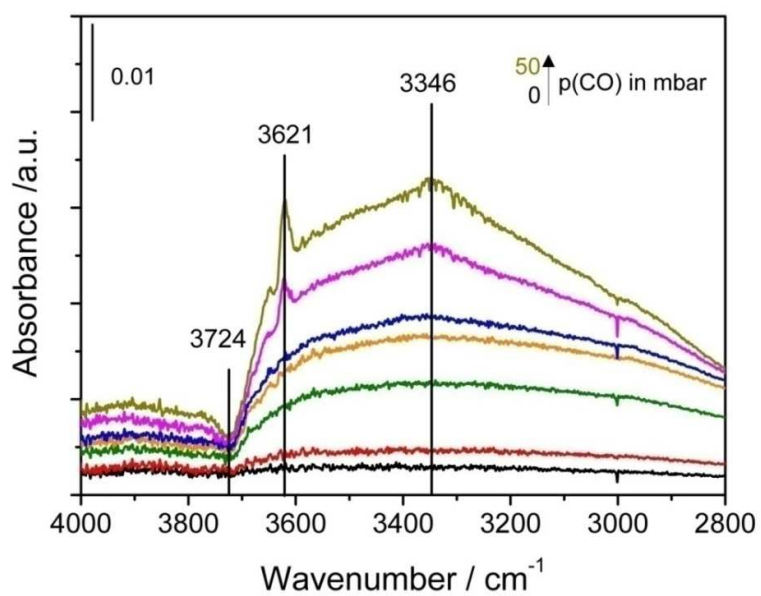
Figure S3- 5: IR spectra of CO adsorbed on Pd_2Ga10 in the OH stretching range from 4000 - 2800 cm^{-1} at RT.
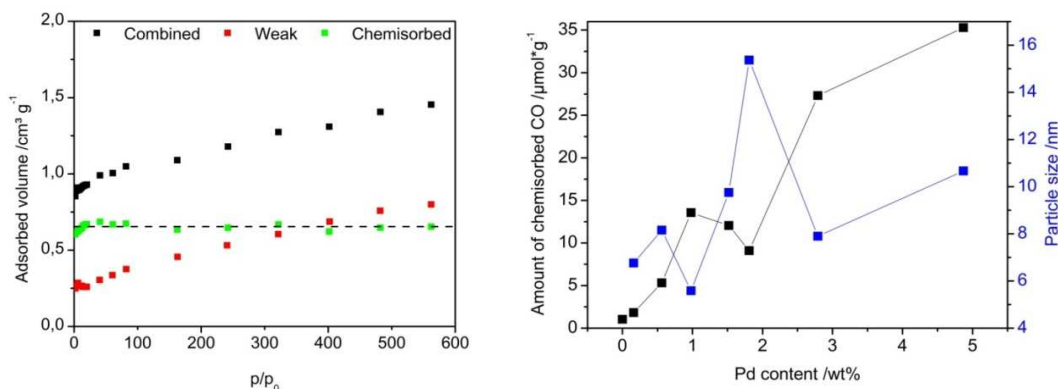
Figure S3- 6: (top) Combined, weak and chemisorbed isotherm of Pd_2Ga25 obtain by CO chemisorption at 313 K. (bottom) Irreversible CO uptake of Pd_2Ga samples and calculated corresponding particle sizes assuming Pd:CO stoichiometry of 1.5.

According to the CO-IR measurements, it is supposed that Pd_2Ga surface is partially decomposed Pd and Ga_2O_3 during chemisorption. No straight adsorption isotherm can be obtained to extrapolate the total amount and the amount of weakly adsorbed CO. No surface saturation with CO is achieved under the applied conditions and furthermore no quantification of the formed Pd patches is possible.

Experimental conditions:

The measurements were carried out in an Autosorb 1C (Quantachrome Instruments). The samples were pretreated in-situ in the sample cell by heating to 773 K for 240 min in 5% hydrogen in helium flow (20 ml/min), followed by an evacuation (240 min) at pretreatment temperature. CO chemisorption measurement was performed at 40°C and in the pressure range of 2 - 560 Torr. The active surface area was determined by Dual isotherm method. The difference of combined and weak isotherm (reversible) results in the irreversible chemisorbed amount of the CO that was used for the calculation.
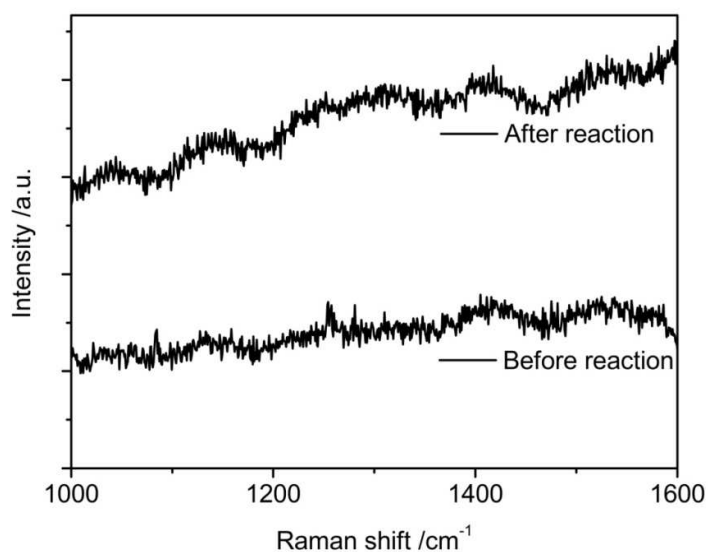
Figure S3- 7: Raman spectra of Pd_2Ga25 catalyst before and after acetylene hydrogenation over 44 h TOS.
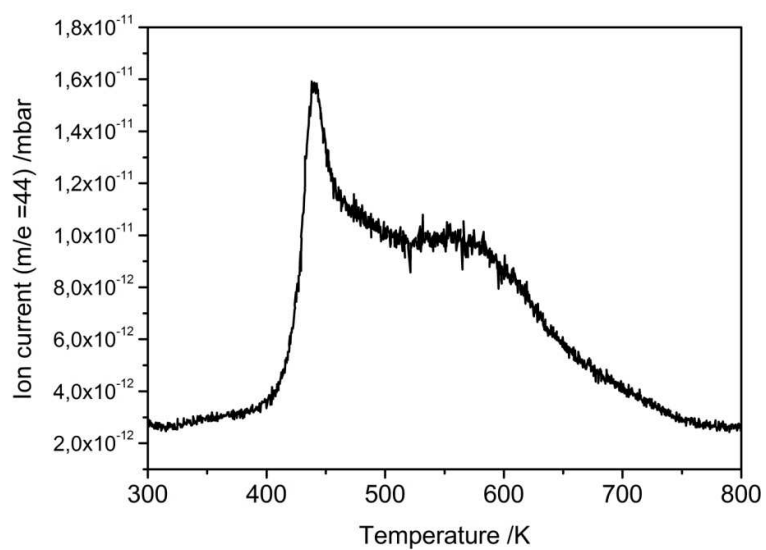
Figure S3- 8: Temperature programmed oxidation of post-reacted Pd_2Ga25 catalyst after 44 h TOS in 21% O_2/Argon.

Chapter 4: Methanol Synthesis and Methanol Steam Reforming of Supported Pd_2Ga and PdZn Intermetallic Nanoparticles

Authors: Antje Ota, Edward L. Kunkes, Igor Kasatkin, Elena Groppo, Davide Ferri, B. Poceiro, Rufino M. Navarro Yerga, and Malte Behrens.

Abstract

Supported PdZn, Pd_2Ga and Pd catalysts were synthesized by reductive decomposition of ternary Hydrotalcite-like compounds. The precursors and resulting catalysts were characterized by HRTEM, XRD, XAS and CO-IR spectroscopy. The Pd^{2+} cations were found to be at least partially incorporated into the cationic slabs of the precursor. Full incorporation was confirmed for the PdZnAl-Hydrotalcite-like precursor. After reduction of Ga- and Zn-containing precursors the intermetallic compounds Pd_2Ga and PdZn were present in form of nanoparticles with an average diameter of 6 nm or less. Tests of catalytic performance in methanol steam reforming and methanol synthesis from CO_2 have shown that the presence of Zn and Ga improves the selectivity to CO_2 and methanol respectively. The catalysts containing intermetallic compounds were 100 and 200 times respectively more active for methanol synthesis than the monometallic Pd catalyst. The beneficial effect of Ga in the active phase was found to be more pronounced in methanol synthesis compared to steam reforming of methanol, which is likely related to insufficient stability of the reduced Ga species in the more oxidizing feed of the latter reaction. Although the intermetallic catalysts were, in general less active than a Cu/ZnO-based material prepared by a similar procedure, the marked changes in Pd reactivity upon formation of intermetallic compounds render our precursor-method an effective and versatile approach to produce well dispersed supported intermetallic nanoparticles and to study the tunability of Pd-based catalysts for different reactions.

4.1.   Introduction

Methanol has been proposed as a promising energy storage molecule for portable applications such as direct methanol fuel-cells, as well as fuel for automobile internal combustion engines.[1] Additionally, methanol has been proposed as hydrogen storage medium [2-4], whose gravimetric hydrogen density exceeds that of compressed and even that of liquid hydrogen. Furthermore, the use of CO_2 as a carbon source for methanol synthesis enables the simultaneous reduction of emissions of this proven greenhouse gas.[1]

Methanol synthesis from CO_2 (Reaction 1) and its reverse reaction, methanol steam reforming (MSR) comprise a class of reactions critical to the application of methanol as an efficient energy carrier.

$$CO_2 + 3H_2 \leftrightarrow CH_3OH + H_2O \ \ \Delta H_0 = \ -49.8 \ kJ/mol \quad (1)$$

$$CO_2 + H_2 \leftrightarrow CO + H_2O \ \ \Delta H_0 = \ +41.2 \ kJ/mol \qquad (2)$$

$$CH_3OH \leftrightarrow CO + 2H_2 \ \ \Delta H_0 = \ +91.0 \ kJ/mol \qquad (3)$$
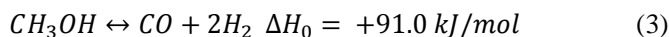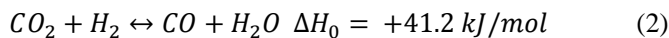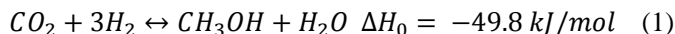
Both reactions are currently carried out at similar temperatures (523 - 603 K) on Cu/ZnO based catalysts. While MSR is not thermodynamically limited and is carried out at atmospheric pressure, methanol synthesis requires high pressures (30 - 100 bar) and lower operating temperatures due to unfavorable thermodynamics.[5] Reverse water gas shift (rWGS, Reaction 2) is a side reaction to methanol synthesis and thus diminishes selectivity. In MSR, methanol decomposition (Reaction 3) as well as rWGS are undesired side reactions and yield CO- a poison for fuel cell electrodes. The rates of both undesired reactions can be thermodynamically hindered by operating at lower temperatures. Lower temperature operation and low selectivity to rWGS or decomposition thus remain the driving forces behind the development and optimization of methanol catalysts.[5]

The current state of the industrial Cu/ZnO catalysts are well suited to stationary operation, however suffer from pyrophoricity, sintering with long reaction times and instability to changes in reaction conditions.[6] These shortcomings make Cu-based catalysts unsuitable for portable applications. To that end, Pd supported on reducible oxides such as ZnO, In$_2$O$_3$ and Ga$_2$O$_3$ has shown favorable reactivity similar to that of Cu-based catalysts for both methanol synthesis and MSR [7, 8], whereas Pd supported on non-reducible supports has been shown to be selective to rWGS and methanol decomposition. Additionally, Pd based catalysts have also shown good long-term stability and resistance to sintering. The alteration of the properties of Pd was

attributed to the formation of the intermetallic compounds (IMCs) Pd_2Ga [9-11] and PdZn [7, 12-14] upon partial reduction of the support components. An intimate interaction between Pd and these support components is therefore thought to be prerequisite to the formation of IMCs.

In that respect, we recently developed a facile wet chemical synthesis approach to prepare Pd-Ga intermetallic nanoparticles. Pd_2Ga nanoparticles supported on oxide matrix of MgO and $MgGa_2O_4$ were synthesized by co-precipitation of a single phase precursor, followed by thermal decomposition.[15] This method presents an efficient alternative to previously used top-down methods, such as etching or milling of materials obtained from high temperature melt synthesis, used previously to synthesize this material.[16] Ternary hydroxycarbonates, namely Hydrotalcite-like compounds (HTlc), were used as precursors. The advantage of these materials is that divalent (M^{II}) and trivalent (M^{III}) cations are uniformly distributed in slabs of edge-sharing MO_6 octahedra that allow a close interaction of all metal cations.[17, 18] HTlc exhibit the general composition $(M1^{II},M2^{II})_{1-x}M3^{III}_x(OH)_2(CO_3)_{x/2}\cdot$ m H_2O ($0.25 \leq x \leq 0.33$) and a huge flexibility of metal cations that can be incorporated into the structure, e.g. $M^{II} = Mg^{2+}$, Mn^{2+}, Co^{2+}, Ni^{2+}, Cu^{2+}, Zn^{2+} and $M^{III} = Al^{3+}$, Ga^{3+}, Fe^{3+}, Cr^{3+}.[19] In our previous work [15] HTlc $M^{II} = Mg^{2+}$ and Pd^{2+} and $M^{III} = Ga^{3+}$ were used to form the precursor of the Pd_2Ga phase. Herein we will present a systematic comparative study of metal-oxide supported Pd and intermetallic Pd-X (X = Ga, Zn) nanoparticles derived from ternary Pd based Hydrotalcite-like compounds. Well-dispersed Pd-Ga, Pd-Zn and Pd nanoparticles (2 - 6 nm) were obtained upon reduction of PdMgGa, PdZnAl and PdMgAl-HTlc synthesized by co-precipitation, respectively.

As all catalysts were derived from a similar well-defined precursor material, aspects of different preparation history, inhomogeneous microstructures, and variations in metal-support contacts, that often complicate the comparison of catalysts, should only play a minor role here. Thus, the aim of this study is to use these materials to investigate the role of different Pd-based IMCs in different reactions involving methanol, namely its synthesis from CO_2 and MSR. In addition to the catalytic performance data, we report on catalyst synthesis and present characterization data using a variety of complementary techniques (XRD, BET, TPR, SEM, TEM, FTIR, XANES) to correlate structural properties with activity.

4.2 Experimental

4.2.1 Synthesis conditions

Ternary palladium containing and binary Pd-free PdMgAl, PdMgGa, PdZnAl, MgGa, ZnAl and MgAl HTlc with $M^{2+}:M^{3+}$ molar ratios of 70:30 were synthesized by co-precipitation. The nominal composition of all Pd-M^{2+}-M^{3+} samples was set to 1:69:30. A mixed aqueous metal

nitrate ([Pd^{2+}] + [M^{2+}] + [M^{3+}] = 0.2 M) solution and 0.345 M basic precipitating agent solution were co-fed at pH = 8.5. For MgGa and MgAl HTlc precursors pure sodium carbonate solution and a precipitation temperature of 328 K were used, whereas in case of PdZnAl HTlc a mixture of sodium carbonate (0.3 M) and sodium hydroxide (0.045 M) and a temperature of 298 K has be applied in order to obtain an homogeneous precursor sample. During precipitation both solutions were added simultaneously dropwise into a 2 L precipitation reactor (Mettler-Toledo LabMax). The nitrate solution was automatically pumped with a constant dosing rate and the basic solution was added to maintain a constant pH of 8.5. After completion of addition, the mixture was aged for 1 h at the same temperatures applied during synthesis. The precipitate was filtered and washed twice with warm deionized water in order to remove the nitrate and sodium ions and obtain a conductivity of the filtrate lower than 0.2 mS/cm. The solid was dried for 12 h at 353 K in air. After drying a one-step decomposition-reduction in 5 Vol% H$_2$/Ar (2 K/min) was performed at the temperatures extracted from H$_2$-TPR experiments that yielded in the intermetallic phases and in metallic Pd in case of the PdMgAl HTlc precursor. A reduction temperature of 523 K was applied for the PdMgAl and PdZnAl system, whereas a reduction of 773 K is needed to obtain Pd$_2$Ga intermetallic particles.

A HTlc-based CuZnAl catalyst was prepared as described previously [20] and was used as reference material for the catalytic test in methanol synthesis. Additional details about the synthesis conditions of the CuZnAl HTlc precursor and the synthesis protocols of the Pd-based HTlc are given in the supplementary information (Figure S4- 1).

4.2.2   Characterization

X-ray diffraction. XRD patterns of the HTlc precursor and its decomposition products were recorded on a STOE Stadi P diffractometer in transmission geometry using Cu Kα_1 radiation, a primary Ge monochromater and a 3° linear position sensitive detector.

Specific surface area determination. Specific surface areas (SSA) of the precursors and reduced compounds were determined by N$_2$ adsorption–desorption measurements at 77 K by employing the BET method (Autosorb-1C, Quantachrome). Prior to N$_2$ adsorption, the sample was outgassed at 353 K/423 K (precursor sample / reduced catalyst) to desorb moisture from the surface and pores.

Chemical Analysis. About 5 mg were exactly weighted in and dissolved in 2 ml aqua regia. The solutions were transferred and filled up in 50 ml volumetric flasks. The content of the metals were determined with ICP-OES (Vista RL, Varian) after matrix matched calibration.

Temperature programmed reduction. The TPR experiments were performed in a fixed bed reactor using 400 mg of precursor (100 - 250 µm sieve fraction). PdMgGa and PdMgAl

precursors were reduced in 5 Vol% H_2 in Argon (100 ml/min) with a heating rate of 2 K/min up to a sample temperature of 773 K. The temperature was kept constant for 4 h. The PdZnAl precursor was heated to 1073 K (2 K/min). The hydrogen consumption was monitored with a thermal conductivity detector.

X-ray absorption near edge structure. XANES data were collected at the Pd K edge (24.350 keV) were carried out at the Super-XAS beamline of the Swiss Light Source (Villigen, Switzerland) in the transmission mode, using ionization chambers as detectors and a Si(311) Quick EXAFS monochromator. A Pd foil placed between the second and third ionization chamber was measured simultaneously as an internal reference. In-situ XANES measurements during hydrogen TPR were performed in transmission mode, using a 3 mm capillary reactor cell (Hilgenberg). The precursor (63 - 100 µm, 30 mg) was filled into the capillary between quartz wool plugs. The cell was connected to a gas manifold. The cell was convectively heated by means of an air blower. Spectra were collected during the reduction in 5 Vol% H_2/N_2 (100 ml/min) in the temperature range of 303 - 773 K. Data reduction was performed using the Athena 0.8.056 software package.

Fourier-Transformed infrared absorption spectroscopy of CO. In-situ experiments were carried out in a custom built quartz cell equipped with KBr windows allowing sample activation and successive measurements in the 292 - 823 K temperature range, at pressures from 10^{-4} to 760 Torr. The catalysts were pressed into self-supporting pellets and activated in the same cell used for the measurement. The thermal treatments were performed either in dynamic vacuum or under static conditions (no flux), according to procedures discussed below. In-situ FTIR spectra on the investigated catalysts were recorded at a resolution of 2 cm^{-1} on a Nicolet 6700 instrument, in transmission mode. PdZnAl and PdMgAl HTlc precursors was outgassed in dynamic vacuum up to 523 K for several hours (until the pressure reached values below 10^{-4} Torr), followed by reduction in H_2 gas (2 cycles of 30 min, p_{H2} = 100 Torr). H_2 was removed from the cell at the same temperature and the sample was allowed to reach room temperature in dynamic vacuum. PdGaMg HTlc precursor was outgassed in dynamic vacuum up to 823 K for several hours (until the pressure reached values below 10 - 4 mbar), followed by reduction in H_2 gas (4 cycles of 1 h, p_{H2} = 100 Torr). H_2 was removed from the cell at the same temperature and the sample was allowed to reach room temperature in dynamic vacuum.

Scanning electron microscopy. SEM images were acquired with a Hitachi S4800 FEG microscope equipped with an EDS system (EDAX) for elemental analysis. The samples were loosely dispersed on a conductive carbon tape to preserve the as-prepared morphology as much as possible. SEM images were acquired at low accelerating voltage, i.e. 1.5 kV, while EDX spectra were acquired at an accelerating voltage of 15 kV.

Electron Microscopy. HRTEM images were acquired using a FEI TITAN microscope, equipped with a field emission gun (FEG) and operated at 300 kV. With computer assisted correction and alignment, the value of the spherical aberration constant C_s was kept below 100 nm in the present experiments. Selected areas of the high resolution images have been Fourier transformed to obtain Power spectra and the lattice distances and angles were measured for phase identification (accuracy ± 1 % and ± 0.5°, respectively). Metal dispersions for Pd based catalysts were obtained by D = 1.1/d, where d is the average particle size determined by TEM neglecting the partial embedment of nanoparticles that reduces the availability of active sites. An estimate of the number of surface metal sites was calculated from this dispersion and the palladium loading, assuming complete accessibility of the surface to the gas phase. For bimetallic nanoparticles, incorporation of second metal (Zn or Ga) was assumed stoichiometric according to PdZn and Pd_2Ga.

4.2.3 Catalytic performance

4.2.3.1 *Methanol synthesis from CO_2*

Methanol synthesis experiments were carried out in a stainless steel fixed-bed flow reactor. 400 mg (100-200 µm) of HTlc precursor was mixed with 2 g of crushed SiO_2 chips and loaded into a 10 mm I.D. stainless steel reactor tube. Gas flows were controlled and monitored with analog mass flow controllers (Brooks 5850A).

The PdZnAl and PdMgAl HTlc precursors were reduced in-situ at 523 K (2 K/min) for 2 h in 100 ml/min (STP) of 20 Vol% H_2 in He. The PdMgGa HTlc precursor was reduced at 773 K (2 K/min) for 5 h in the same H_2/He mixture. Upon completion of the reduction, the reactor was cooled to 523 K, a 3:1 H_2/CO_2 mixture (100 ml/min) containing 4 Vol% Ar (as internal standard) was introduced into the reactor and the pressure was raised to 30 bar by means of a back-pressure regulator (Tescom). The back pressure regulator and all high-pressure line were heated to 423 K to avoid condensation of water and methanol, and all low-pressure lines downstream of the back-pressure regulator were heated to 393 K. Online analysis of products was performed with a GC (Agilent 6890) equipped with a J&W scientific Haysep Q Column and a TCD for analysis of non-condensable gases and a Agilent DB1 column interfaced to an FID for analysis of methanol. Methanol and CO were the main products observed, along with traces (less than 0.1% selectivity) of methane. After the start of the reaction, the catalysts were allowed to stabilize for 20 h time-on-stream at 523 K. After this period, the activation energies of methanol synthesis and rWGS were measured in the temperature range of 463 – 548 K, with

4 h allowed for each temperature point. Conversions of CO$_2$ were below 3% insuring the absence of thermodynamic artifacts.

4.2.3.2 Methanol steam reforming

Methanol Steam reforming (MSR) reaction was conducted using a fixed-bed flow reactor at 523 K and atmospheric pressure. Activity tests were performed using 0.125 g of HTlc precursor diluted with SiC at volume ratio of 3:1 to avoid adverse thermal effects. Catalyst bed was placed in a 6 mm I.D. quartz tubular reactor with a coaxially centered thermocouple. Prior to reaction, the PdZnAl and PdMgAl HTlc precursors were reduced in-situ at 523 K (2 K/min) for 4 h in 60 cm³ (STP) of 5 Vol% H$_2$ in N$_2$. The PdMgGa HTlc precursor was reduced at 823 K (2 K/min) for 4 h in the same H$_2$/N$_2$ mixture. The pretreating gases were flushed from the reactor with N$_2$ before admission of methanol-water-nitrogen reaction mixtures. Methanol and water mixture was supplied into a preheater by means of a liquid pump (Becton-Dickinson) before their mixture with nitrogen carrier supplied by Brooks model 5850E mass flow controller. For MSR reaction, the reactants were introduced into the reactor in the molar ratio H$_2$O/CH$_3$OH = 1.0. In the MSR tests, the total flow rate was kept at 26 ml/min (STP) and the methanol concentration in the feed gas mixture was fixed at 28.4 Vol% to avoid thermal effects derived from the high endothermicity of the reaction.

The reaction products were analyzed on-line by GC with TCD (HP 6890 GC) equipped with CP-Porabond Q (CO$_2$, water, methanol, formaldehyde, methyl formate and dimethyl ether) and molecular 5A (H$_2$, O$_2$, N$_2$, CO) connected in series, using He as carrier gas. Each value of total conversion is the average of two different analyses taken after 3h time-on-stream at a given temperature.

The hydrogen selectivity of the reaction was determined by comparing the molar hydrogen production rate to the maximum stoichiometrically allowable hydrogen production rate at a given methanol conversion (4).

$$S = \frac{r_{H2}}{3r_{MeOH}} \qquad (4)$$

If the reaction is dominated by MSR, H$_2$ and CO$_2$ selectivities should lie at around 100%, whereas if methanol decomposition is the primary reaction, the H$_2$ selectivity lies at 67% and the CO$_2$ selectivity near zero.

4.3 Results and discussion

4.3.1 Properties of the HTlc precursors

PdZnAl, PdMgGa and PdMgAl HTlc precursors have been prepared with 1 mol% of the cations being Pd^{2+} and a $M^{2+}:M^{3+}$ ratio of 70:30 by co-precipitation. The XRD patterns of all as-synthesized precursor samples are typical of Hydrotalcite-like structure, as shown in Figure 4-1. No Pd containing or other crystalline phases were observed. The crystallinity of the precursors decreased in the order of PdMgGa > PdZnAl > PdMgAl as indicated by the decreasing intensity as well as the increased peak broadening.
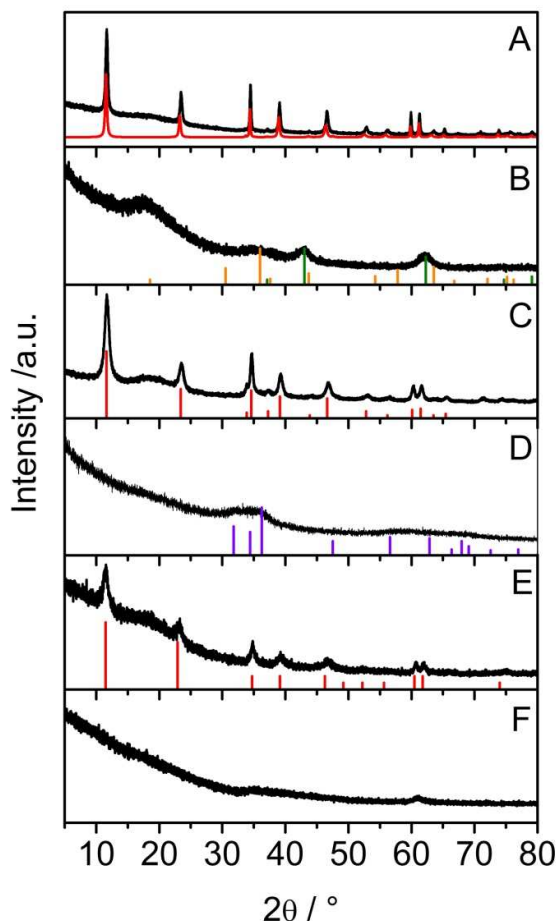
Figure 4- 1: XRD patterns of (A) PdMgGa and simulated MgGa HTlc precursor; (B) PdMgGa HTlc after reduction at 773 K, ICDD 1-1235 MgO (green), ICDD 10-113 $MgGa_2O_4$ (orange); (C) PdZnAl HTlc precursor and ICDD 38-486 $Zn_6Al_2(OH)_{16}CO_3 \cdot 4\ H_2O$; (D) PdZnAl HTlc after reduction at 523 K, ICDD 36-1451 ZnO (violet); (E) PdMgAl HTlc precursor and ICDD 14-191 $Mg_6Al_2(OH)_{16}CO_3 \cdot 4\ H_2O$; (F) PdMgAl HTlc after reduction at 523 K.

In Table 4- 1 the measured chemical composition of Pd containing and Pd-free HTlc precursors is listed. There are small deviations between the nominal and measured composition. In particular the M^{3+} content of PdMgAl and PdMgGa HTlc is increased to 35 mol% and the Pd content of PdMgAl HTlc is slightly higher than 1 mol% (1.3 mol%).

Table 4- 1: Chemical composition and textural properties of the HTlc precursor materials.

Sample	Measured Composition[a] Pd:M^{2+}:M^{3+}	BET SA Precursors [m²/g]	BET SA Reduced [m²/g]	Pd content after reduction [wt%]	Particle size by TEM [nm]
ZnAl	0:70.3:29.7	53	n.d.[b]	-	-
PdZnAl	1.0:69.5:29.5	85	86[c]	1.46	1.8[c]
MgGa	0:63.2:36.8	34	130	-	-
PdMgGa	1.0:64.5:34.5	48	116[d]	1.81	6.1[d]
MgAl	0:65.6:34.4	111	n.d.[b]	-	-
PdMgAl	1.3:69.1:29.6	127	123[c]	3.13	2.2[d]

[a] determined by ICP-OES; [b] n.d. = not determined; [c] reduced at 523 K; [d] reduced at 773 K

The specific surface areas of the HTlc precursor, as obtained by nitrogen physisorption, varied between 34 and 127 m²/g (Table 4- 1). The substitution of M^{2+} by Pd^{2+} resulted in an increase of the surface area in all samples probably due to hindered growth of the Pd distorted HTlc lattice. In general, the surface area increases from PdMgGa < PdZnAl < PdMgAl which is in agreement with the broader XRD line profiles suggesting smaller crystallite sizes. Differences in surface area and XRD peak widths are compatible with the observation of SEM measurements. As shown in Figure 4- 2, the HTlc precursors show similar platelet-like morphology, but the particle sizes differed considerably. Small platelets were obtained for PdMgAl (Figure 4- 2C) and PdZnAl (Figure 4- 2A). The thickness of the platelets is in the low nanometer range, while the lateral dimension is approximately around 250 nm or below. Although for PdMgAl and PdMgGa samples the same synthesis conditions were applied the lateral size of the PdMgGa platelets is increased to 0.4 - 1 μm. The PdMgGa and PdMgAl platelets exhibit sandrose morphology, while the PdZnAl platelets are randomly oriented. However, no large Pd agglomerates were detected outside the platelets by SEM and also EDX mapping suggests a homogenous metal distribution for all samples (not shown).
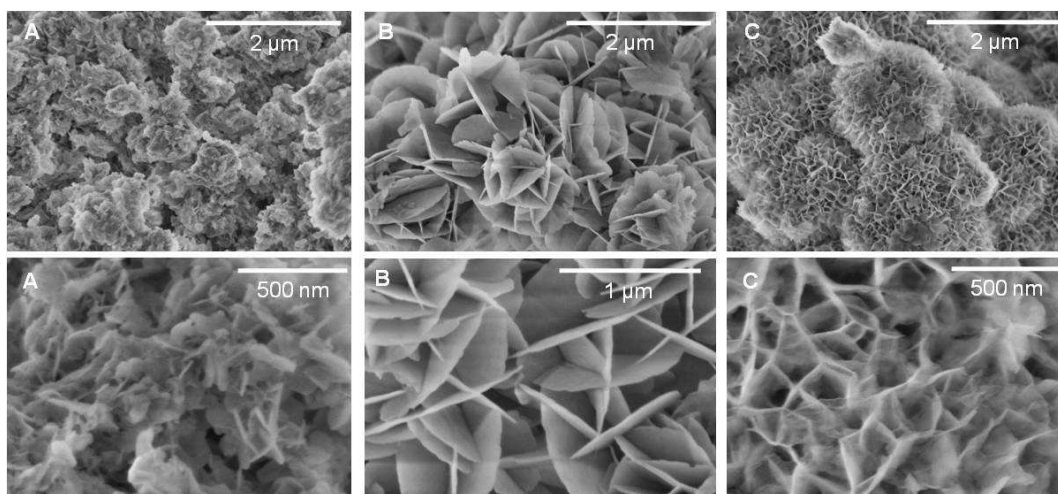
Figure 4- 2: SEM images of (A) PdZnAl, (B) PdGaMg and (C) PdMgAl HTlc precursor.

4.3.2   Reducibility of the HTlc precursors and IMC formation

4.3.2.1 TPR and MS measurements

TPR experiments were performed in order to study the IMC formation and monitor the reduction process. All TPR profiles can be separated into three regions: a room temperature reduction (RTR), a low temperature reduction (LTR, < 573 K) and high temperature reduction region (HTR, > 573 K). RTR contains any initial hydrogen consumption detected upon switching to reducing atmosphere at room temperature before the heating ramp was started. Figure 4- 3 includes the LTR and HTR processes, only. The reduction from Pd^{2+} to metallic Pd^0 normally occurs in the RTR or LTR regime, at temperatures lower than ca. 423 K. Quantification of the degree of reduction from the hydrogen consumption turned out to be complex for these samples. Metallic Pd particles form hydrides and transfer spillover hydrogen to the support material; both phenomena lead to higher hydrogen consumption than expected for stoichiometric Pd^{2+} reduction.[21] The PdH$_x$ phase is not stable during heating and decomposes at higher temperatures producing a negative peak in the TPR profile. In the HTR regime hydrogen consumption due to partial reduction of reducible metal oxides overlaps with further H$_2$ consumption due to conversion of CO$_2$, which is released as a decomposition product of the interlayer carbonate ions. As matters of fact, CO and CH4 have been detected by MS during LTR and HTR (Figure 4- 3, bottom). Thus, evolved CO$_2$ is not completely emitted from the catalyst bed, but varying fractions undergo rWGS and methanation at the surface of the metallic nanoparticles. This resulted in considerably higher hydrogen consumption than expected for stoichiometric reduction of the metal cations. Apparently, hydride formation, spillover

hydrogen, and CO$_2$ conversion are dominating the consumption and it is only considered in a semi-quantitative manner here, i.e. by comparison of the TCD peak integrals of the different samples in the different temperature regimes.

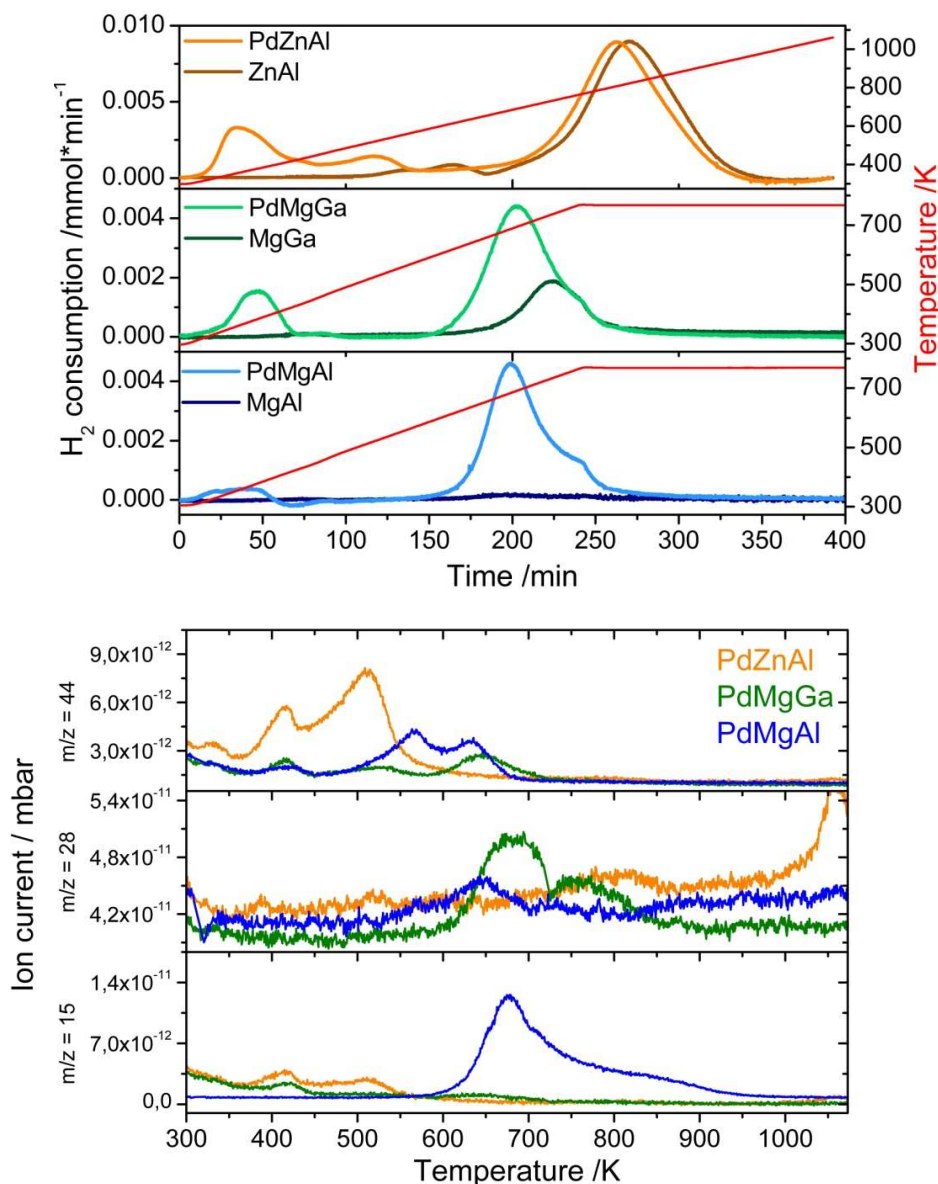Figure 4- 3: (top) TPR profiles of Pd substituted and unsubstituted Hydrotalcite-like precursors and (bottom) MS profiles (obtained by TGA-MS) in 5 Vol% H$_2$/Ar.

As expected, no hydrogen consumption was observed in the RTR and LTR regions for the Pd-free samples. For the Pd containing precursors, the profiles in this region are different. RT and LT hydrogen consumption were observed for PdMgGa and PdMgAl samples, while for PdZnAl

sample H_2 uptake was not detected at RT. This suggests that in the former samples two different Pd^{2+} species were present, one easily and one harder to reduce. The main LTR peaks are found at 359, 382 and ca. 343 K for PdZnAl, PdMgGa and PdMgAl, respectively, which are relatively high values for the reduction of Pd^{2+}. From this observation, the RTR peak can be assigned reduction to PdO-like species not incorporated into the HTl lattice, while the LTR peaks are due to reduction of HTl-lattice Pd^{2+} cations. This assumption is consistent with XANES measurements discussed below. Furthermore, Pd hydride is observed only for the PdMgAl (small negative peak around 423 K). Additional LT hydrogen uptake was observed for PdZnAl at 520 K. It is known that ZnO can be reduced in the presence of Pd at such mild temperatures to form the IMC PdZn.[13, 21] Since the above mentioned LTR peak is absent for the Pd-free precursor, it is assigned to reduction of ZnO with consequent IMC formation (although small amounts of CH_4 were detected at this temperature). No further peaks are detected in the LTR region for PdMgGa and PdMgAl samples. In PdMgAl there are no other reducible species. In PdMgGa this observation indicates that the IMC formation takes place at higher temperature. Therefore, the process cannot be accurately studied by TPR, because of the overlap with CO_2 conversion in the higher temperature regime (see Figure 4- 3, bottom).

In the HTR regime, hydrogen consumption was detected for all precursors, also for the Pd-free MgGa and ZnAl, except for MgAl. At these temperatures, partial reduction of the reducible oxides is expected also in the absence of Pd. Starting from PdZnAl and ZnAl, HTR consumption peaks having a similar integral area were observed at approximately same temperature (808 K and 823 K). No traces of CO, or CH_4 by MS were noticed at that temperature (Figure 4- 3). As a consequence, the peaks are assigned to reduction of the ZnO-component of the support. For MgGa and PdMgGa, the presence of Pd leads to an increase of the total HTR hydrogen consumption and to a decrease in temperature from 736 to 695 K. In both samples, CO was detected by MS. Thus, at sufficiently high temperature CO_2 from decarboxylation of the interlayer carbonate anions undergoes rWGS on the reducible oxides.[22] In case of PdMgGa the hydrogen uptake due to rWGS and support reduction overlaps with IMC formation (Figure 4- 3). Only the non reducible MgAl sample does not show any significant hydrogen consumption over the whole temperature range. Addition of Pd to this sample induced an uptake of hydrogen at 679 K; correspondingly, CH_4 was detected by MS (Figure 4- 3). Therefore, it is concluded that CO_2 deriving from decomposition of the interlayer carbonates is converted to methane over metallic Pd. TPR and MS data provide first evidence that the catalytic properties of Pd have been markedly modified by formation of IMCs. While PdMgAl (where no IMC is formed) was found to be active in methanation, PdMgGa converts CO_2 in the

rWGS to CO at comparable conditions. The HTR hydrogen conversion of PdZnAl can be completely ascribed to the reducibility of the support material. From the TPR results, the reduction temperatures for IMC formation were estimated to 523 K for PdZnAl and 773 K for PdMgGa. The PdMgAl reference sample was reduced at 523 K.

4.3.2.2 XANES measurements

XANES measurements were carried out to gain more insight into the Pd speciation in the precursor and in the RTR and LTR events. Since TPR measurements suggested the presence of two Pd-species in PdMgAl and PdMgGa, different reference materials were used to evaluate the XANES data. Commercial PdO was chosen as reference material for segregated Pd^{2+} species in the precursor, which is not incorporated in to the HTl lattice. Pd^{2+} in PdO prefers square planar coordination as well as Pd^{2+} in aqueous solution and most other solids. On the contrary, incorporation into the Hydrotalcite lattice requires octahedral coordination of Pd. The low-spin d^8 electronic configuration of Pd^{2+} makes regular octahedral coordination unstable with respect to large tetragonal elongations. Octahedral coordination of Pd^{2+} with oxygen was obtained in a high-pressure phase of PdO at 12 GPa.[23] Moreover, octahedral environment was also observed for Pd cations having higher oxidation states. For instance, Zn_2PdO_4 is a compound where Pd^{4+} has regular octahedral symmetry in the cubic spinel structure [24], while in $LaPdO_3$ Pd^{3+} has a distorted perovskite structure that stabilizes the trivalent ion in octahedral coordination.[25] The XANES spectra of the HTl precursors are shown in Figure 4- 4; both in the unreduced state and after treatment at 323 K in hydrogen, i.e. at a temperature where RTR has already occurred, but low enough not to trigger LTR. XANES spectra of PdO as reference for segregated Pd^{2+} species before RTR and of metallic Pd for the state after RTR were included.
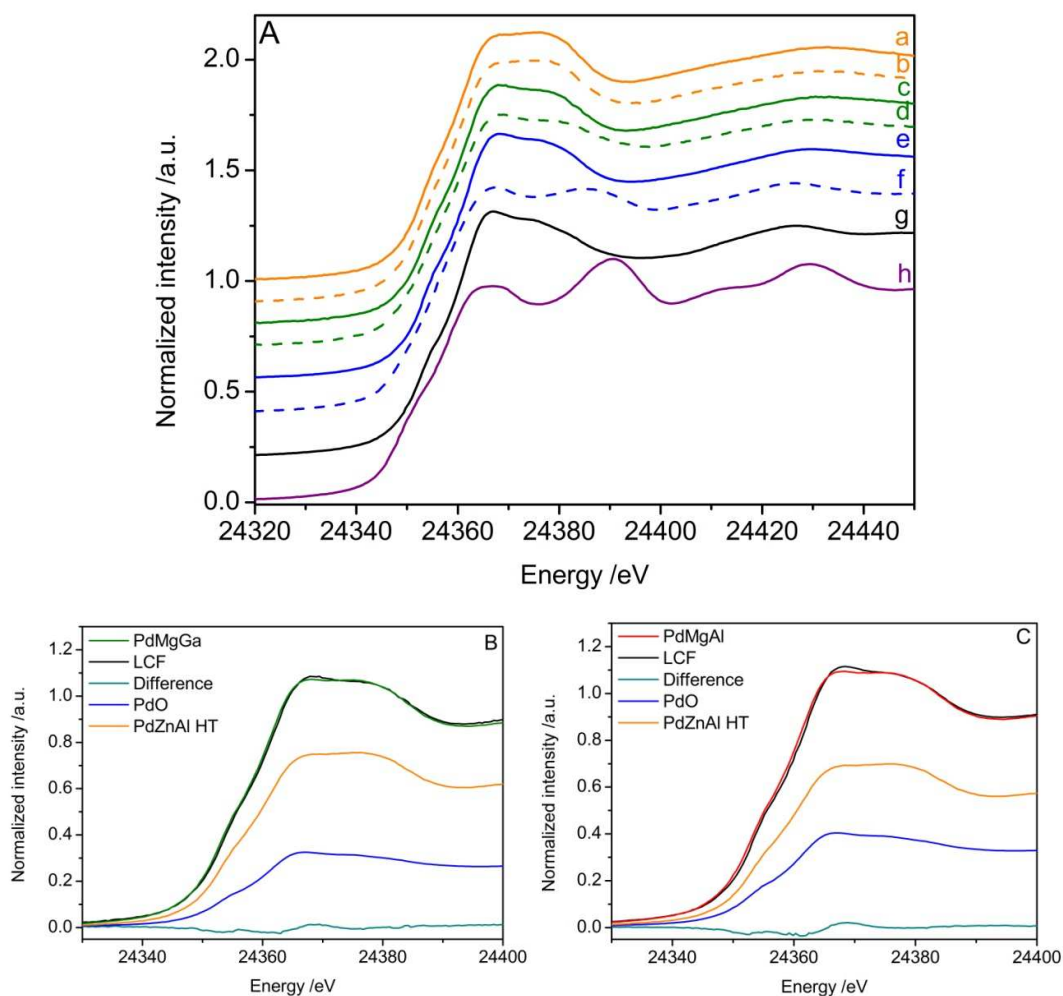
Figure 4- 4: (A) XANES spectra PdZnAl at RT/He (a) and 323 K/H_2 (b), PdMgGa at RT/He (c) and 323 K/H_2 (d), PdMgAl at RT/He (e) and 323 K/H_2 (f), PdO (g) and Pd foil (h) reference. (B+C) Linear combination fit of the XANES spectra of PdMgGa and PdMgAl precursor, by using PdO and PdZnAl as references for Pd^{2+} in square planar and octahedral coordination, respectively

The intensity ratio of the white line and the first feature of the XANES spectrum of PdZnAl HTlc are significantly different from that of PdO. It is similar to that reported for LaFe$_{0.95}$Pd$_{0.05}$O$_3$ where Pd exhibits a distorted octahedral coordination and occupies Fe sites.[26] Changing to reducing atmosphere did not induce a change of the XANES of PdZnAl, which is in agreement with the TPR experiment that did not show any RT reduction. Therefore we assume that in this sample Pd^{2+} is fully incorporated into the HTl structure and not available for reduction to metallic Pd below 323 K. Therefore the PdZnAl spectrum recorded at RT in inert atmosphere was taken as a second reference for Pd^{2+} that is incorporated into the HTlc structure

and exhibits octahedral coordination. Linear combination of PdO and PdZnAl spectra were used to obtain the fraction of Pd present as PdO and as incorporated within HTlc structure, as shown in Figure 4- 4B and C. Accordingly, analysis revealed that 68% of Pd^{2+} is present in octahedral coordination for PdMgGa, while in case of PdMgAl only 61% of Pd^{2+} is incorporated. Both samples showed a certain degree of RT reduction in the TPR and also the XANES spectra changed significantly upon H$_2$ reduction at 323 K (Figure 4- 4). In case of PdMgAl the near-edge features approach those of metallic Pd^0. The PdMgGa sample is apparently more stable and changes only slightly. This stability is in agreement with the increased onset of the reduction temperature for PdMgGa as well as significantly higher LT reduction temperature observed in the TPR experiments (Figure 4- 3).

4.3.3   Properties of the ex-HTlc samples after reduction

The XRD patterns of the reduced samples presented in Figure 4- 1 contain only broad modulations of the background suggesting poor crystallinity and small crystallize sizes. After reduction at 523 K PdMgAl is amorphous (Figure 4- 1F) and only heating to 773 K leads to significant growth of XRD peaks due to poorly crystalline MgO and MgAl$_2$O$_4$ (not shown). Formation of periclase and spinel phases was also observed for PdMgGa after reduction at 773 K (Figure 4- 1B). The PdZnAl sample showed very weak and broad peaks due to ZnO after reduction at 523 K (Figure 4- 1D). The XRD data is an agreement with HRTEM analysis of the phases of the support.

Because the metallic component was not able to be identified by means of XRD, probably due to the low total Pd content and the small crystallite size, XANES and HRTEM were applied for phase identification. Figure 4- 5 shows the XANES spectra of the reduced precursors at the reduction temperatures deduced from the TPR experiment. Palladium foil, bulk Pd$_2$Ga and PdZn are shown as reference materials. In general, lower amplitudes of the oscillations were observed for the nanoparticulate samples, in particular for PdZnAl. Nevertheless the spectra show a high agreement and resembled those of the associated bulk references.
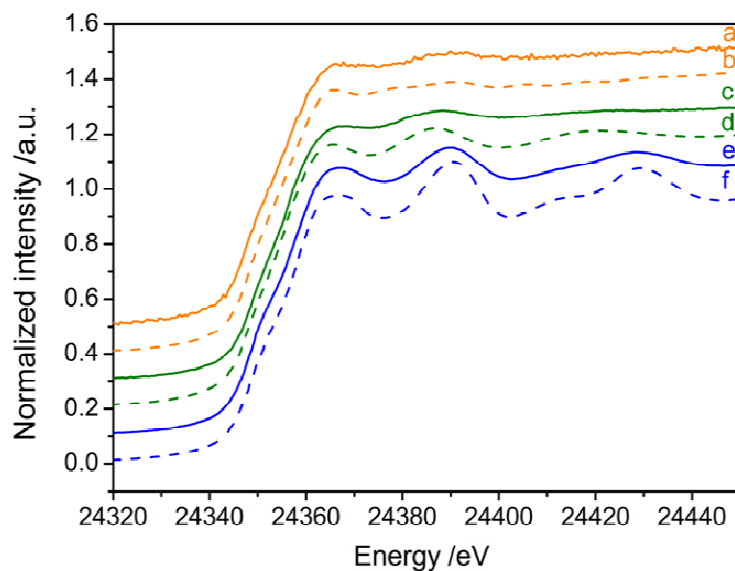
Figure 4- 5: In-situ XANES spectra of (a) PdZnAl reduced at 523 K and (b) bulk PdZn, (c) PdMgGa reduced at 773 K and (d) bulk Pd$_2$Ga, (e) PdMgAl reduced at 523 K and (f) Pd foil.

TEM revealed that the platelet-like morphology of the HTlc precursor was retained after reduction and all catalysts showed spherical particles distributed on the platelets as presented in Figure 4- 6A and Figure 4- 7A. HRTEM images were used to determine the net plane distances and plane angles by FFT.
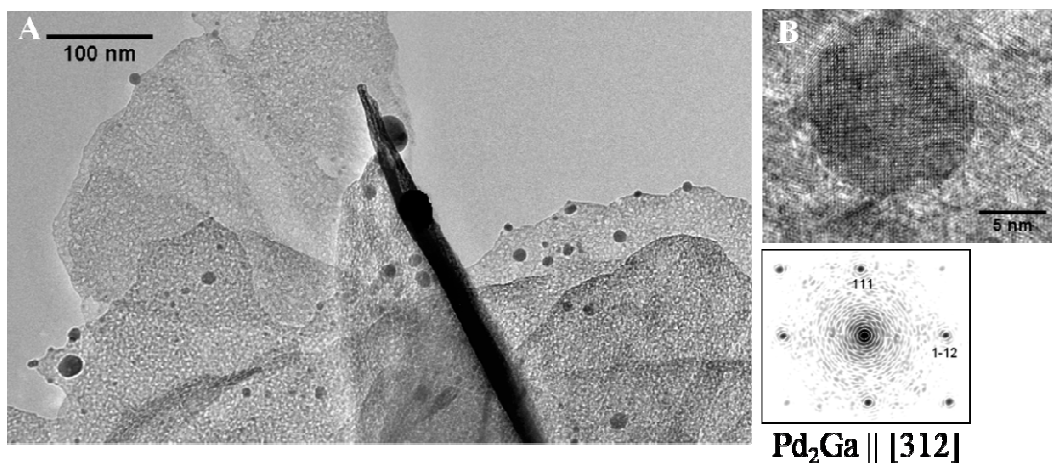
Figure 4- 6: (A) overview TEM images PdMgGa after reduction at 773 K in 5 Vol% H$_2$/Ar, and (B) HRTEM image and corresponding FFT pattern of Pd$_2$Ga.
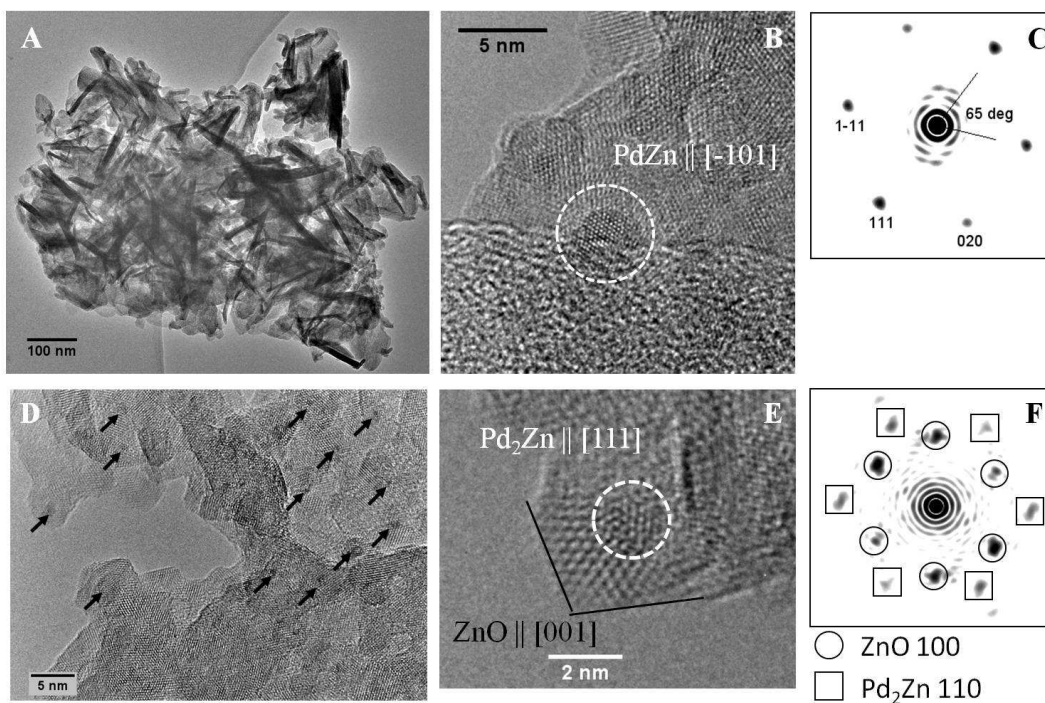
Figure 4- 7: (A+D) Overview TEM images, and (B, E) HRTEM and corresponding FFT pattern
(C, F) of PdZnAl after reduction at 523 K in 5 Vol% H$_2$/Ar.
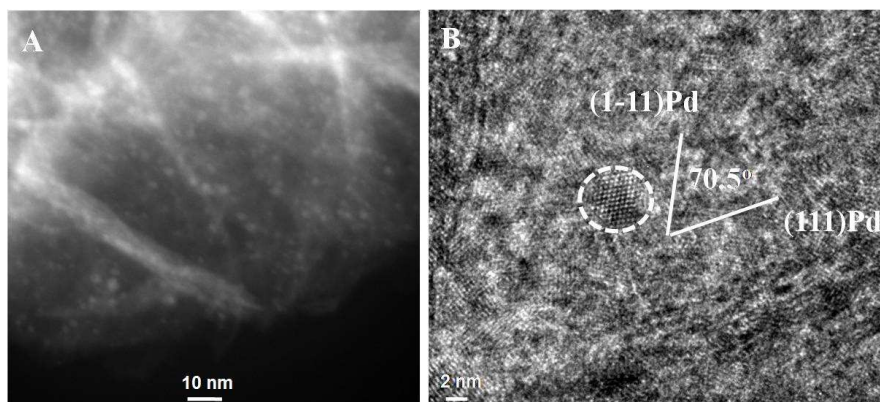
Figure 4- 8: (A) STEM, and (B) HRTEM images of PdMgAl after reduction at 773 K in 5 Vol%
H$_2$/Ar.

Reduction of PdMgGa yielded well dispersed, supported nanoparticles as presented in Figure 4-
6A. The corresponding power spectrum of the HRTEM image, shown in Figure 4- 6B, allowed
identification of the intermetallic Pd$_2$Ga phase (ICDD 65-1511). In agreement with XRD,
partially crystalline MgO and MgGa$_2$O$_4$ were present as oxidic support.[15] However, for

95

PdZnAl two different Pd-Zn IMCs were identified after reduction at 523 K. The crystal planes
($1\bar{1}1$) and (111) of PdZn (ICDD 6-620) were identified with the characteristic acute angle of 65°
along the [$\bar{1}01$] zone axis (Figure 4- 7B+C). Additionally, nanoparticles with a core-shell
structure were present. The phase in the core was identified as Pd$_2$Zn (circled area, ICDD 6-
629) surrounded by an ordered shell of ZnO (Figure 4- 7E+F). This arrangement suggests that
Pd$_2$Zn might be an intermediate of the reduction of PdZnAl. ZnO seems to have segregated
from the oxide support to encapsulate the metal core by strong metal support interaction and
supply further Zn atoms for IMC formation through the reactive Pd-ZnO and Pd$_2$Zn-ZnO
interfaces, finally resulting in formation of PdZn. Figure 4- 8 shows the PdMgAl sample after
reduction at 773 K. In STEM mode homogeneous and small-sized Pd nanoparticles on MgAlO$_x$
support were observed (Figure 4- 8A) and HRTEM investigations (Figure 4- 8B) confirming the
presence of metallic Pd (ICDD 46-1043). The average particle sizes were obtained from
projected areas of the metal particles and were 1.8, 2.2 and 6.1 nm for PdZnAl, PdMgAl and
PdMgGa HTlc, respectively. The considerably large size of the Pd$_2$Ga particles can be
explained by higher reduction temperature that was necessary to form the IMC. The
corresponding size distributions are shown in Figure S4- 2.

FT-IR spectroscopy of adsorbed CO was adopted to investigate the surface properties of the
metallic Pd, PdZn and Pd$_2$Ga components in PdMgAl, PdZnAl and PdMgGa after reduction,
respectively. The spectra of CO adsorbed at room temperature on the three samples are shown
in Figure 4- 9 as function of CO coverage. Several IR absorption bands were observed in the
range of 2100 - 2000 cm^{-1} and 1970 -1 800 cm^{-1}. These bands are characteristic of linearly and
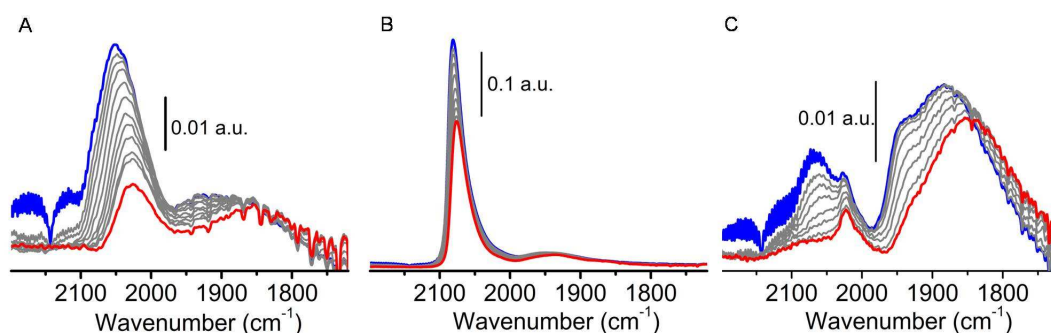multiply bonded CO on Pd^0 atoms, respectively.[27]

Figure 4- 9: FT-IR spectra of CO adsorbed at room temperature on (A) PdZnAl (reduced at 523
K), (B) PdMgGa (reduced at 823 K) and (C) PdMgAl (reduced at 523 K) as a function of CO
coverage (θ_{max}: blue, θ_{min}: red).

As reported by Kovnir et al. [28] and Conant et al. [14] the absence or strong reduction of multiple bonded carbonyl species should be observed for Pd-Ga and Pd-Zn intermetallic compounds. Indeed, mainly on-top coordinated CO species, characterized by IR absorption bands at 2080 cm^{-1} and 2050 cm^{-1} were observed for PdMgGa and PdZnAl, as shown in Figure 4- 9A and B. In contrast, CO absorption on PdMgAl sample revealed a much larger population of multiply bonded sites compared to linearly coordinated CO (Figure 4- 9C). At low CO coverage the band of linearly coordinated CO was observed at 2020 cm^{-1} , which is relatively low, but still in the characteristic range. According to Prinetto et al. [29] the frequency red shift originates from CO absorption on Pd sites, whose electronic properties are modified by interaction with basic support species. With increasing CO coverage, an additional band at 2080 cm^{-1} gains intensity and slightly shifts to higher wavenumbers due to increased dipole-dipole coupling of the neighboring CO groups.

In summary, small particles of the IMCs have been obtained from HTlc precursors with at least partial Pd^{2+} incorporation on octahedral sites in the cationic layers. Upon reduction in hydrogen, metallic Pd segregated from the precursors at low temperature and as the reduction temperature increases, IMC particles are formed. For PdZnAl the IMC PdZn is formed at 523 K probably via a Pd_2Zn intermediate stage. The average particle size is about 1.8 nm. Pd_2Ga formed from PdMgGa at higher temperature (773 K) and the average particle size is larger (6.1 nm). Compared to the monometallic Pd particles obtained by PdMgAl, the adsorptive properties of the IMC particles are strongly modified suggesting differences in catalytic properties.

4.4 Catalytic properties of the IMCs

4.4.1 Methanol synthesis from CO_2

Activity versus time-on-stream data for methanol synthesis and rWGS at 523 K is shown in Figure 4- 10 for all Pd based catalysts. After a 5 h stabilization period, all catalysts show only very slow loss of activity with time-on-stream. PdMgGa and PdZnAl showed similar steady-state activities for methanol synthesis of 18.7 and 17.6 µmol/(g_{cat}·min), respectively. These activities amounted to nearly 30 times the methanol synthesis activity of PdMgAl (0.65 µmol/(g_{cat}·min)). In contrast to this difference, the rWGS of all catalysts were within a similar range, with PdMgGa (27.8 µmol/(g_{cat}·min)) being twice as active as PdMgAl and PdZnAl with 14.3 and 13.5 µmol/(g_{cat}·min), respectively. These results are consistent with those of Iwasa et al. [30] and Fujitani et al. [31], who showed that Pd supported on ZnO and Ga_2O_3 possessed significant methanol synthesis activity, whereas unsupported Pd and Pd on irreducible SiO_2

were almost inactive for methanol synthesis. Additionally, the results of Iwasa showed far less significant differences in rWGS rates on these catalysts. A similar observation about rWGS activities can be made for the catalysts studied in this work. From this observation it can be concluded that free Pd may be responsible for the rWGS activity, whereas the intermetallic sites lead to methanol formation. However, Iwasa et al. [30] had shown, that the rWGS activity of Pd/ZnO decreases by only 40% upon the complete conversion of Pd into a PdZn alloy. It is therefore possible that the intermetallic surfaces behave similarly to Cu, in that they possess sites for both methanol synthesis and rWGS.
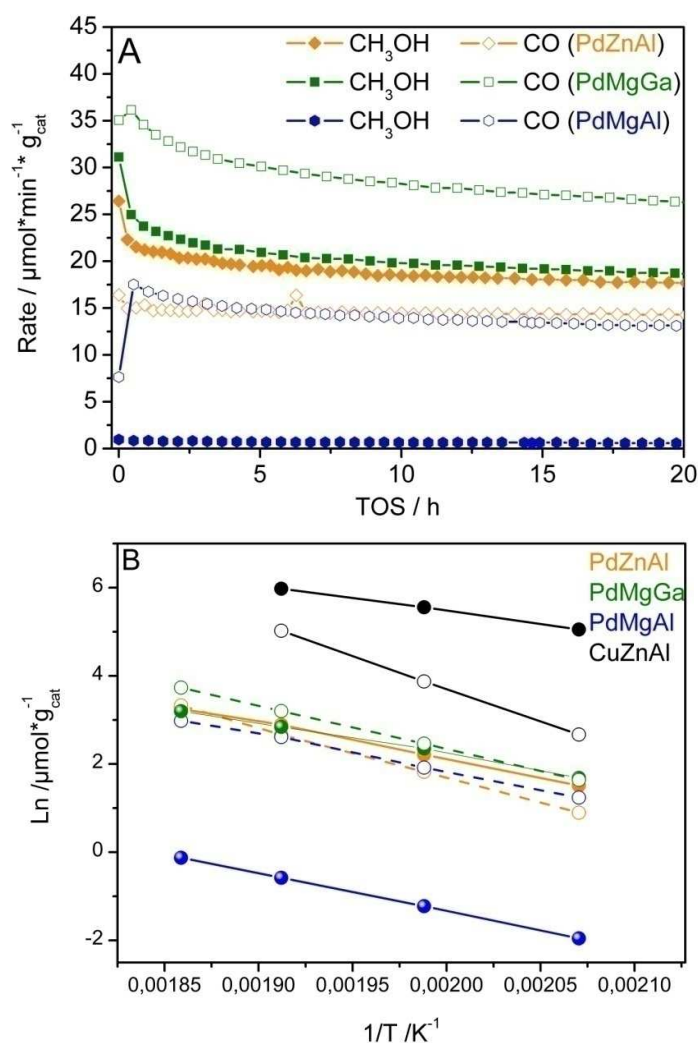

Figure 4- 10: (A) Rate of CO_2 hydrogenation over PdZnAl, PdMgGa and PdMgAl at 523 K (30 bar, 400 mg catalyst, 100 ml/min CO_2/H_2). (B) Arrhenius plot for methanol synthesis from CO_2 (closed symbols: MeOH, open symbol CO).

Table 4- 2: Activities for methanol synthesis from 1:3 CO_2:H_2 mixture at 30 bar on Pd and Cu catalysts.

Catalyst	Metal site [µmol/g$_{cat}$]	X$_{CO2}$ [%]	Rate [µmol/min·g$_{cat}$]		S.V. [mmol/g$_{cat}$·min]	S$_{MeOH}$ [%]	TOF [min^{-1}]	
			MeOH	CO			MeOH	CO
PdZnAl	73.4	0.60	9.1	6.2	10	60	0.12	0.08
PdGaMg	20.4	1.0	10.5	11.7	10	47	0.51	0.57
PdAlMg	90.9	0.30	0.3	6.8	10	4	0.003	0.07
CuZnAl	170.9	5.0	67.3	47.6	10	59	0.39	0.28
		1.30	222.4	47.6	93	82	1.30	0.28

In order to correctly compare the intrinsic activities and apparent activation energies for the Pd catalysts with those of a more active CuZnAl catalyst, which was also prepared from a single phase HTlc precursor, the space velocity had to be varied. When all catalysts are compared at 523 K and a space velocity of 10 mmol/(g$_{cat}$·min) , the Cu based catalyst shows a CO_2 conversion of 5% and a mass normalized methanol synthesis rate that is 6 times that of the bimetallics, of which each show less ~1% CO_2 conversion. At these conditions, PdMgGa (0.51 min^{-1}) appears twice as intrinsically active (TOF) as PdZnAl (0.12 min^{-1}) and is more active than the CuZnAl catalyst (0.39 min^{-1}). PdZnAl shows a similar methanol selectivity to that of CuZnAl (60%) and is more selective that PdMgGa (47%). According to several investigators, the water produced during methanol synthesis and rWGS acts to inhibit methanol synthesis on Cu. [32, 33] The concentration of this water is directly dependent on the CO_2 conversion. In that respect, the CuZnAl catalyst is exposed to 5 times more water than the IMC catalysts when tested at the same gas space velocity. To take the effects of water inhibition into account, the space velocity for CuZnAl was raised to 93 mmol/(g$_{cat}$·min), resulting in a CO_2 conversion of 1.3%, i.e. in the same range as for the IMC catalysts at lower space velocities. At these conditions, the methanol TOF increased to 1.3 min^{-1}, and is 4-12 times higher than that of the IMCs (Table 4- 2). Furthermore, at these conditions CuZnAl shows a significantly higher selectivity to methanol synthesis (82%) as compared to the IMCs. It should be noted however, that the intrinsic activities of the IMCs are still two orders of magnitude higher than of PdMgAl. The comparison of apparent activation energies between Cu- and Pd-based catalysts results in an intuitive understanding to the effect of IMC formation on reactivity. The Arrhenius plots for methanol synthesis and rWGS are shown in Figure 4- 10B for Pd-based catalysts tested at a space velocity of 10 mmol/(g$_{cat}$·min) and CuZnAl at 93 mmol/(g$_{cat}$·min). It is interesting to note

that the activation energy for methanol synthesis decreases from 72 kJ/mol in PdMgAl to 68 kJ/mol in PdZnAl and 59 kJ/mol in PdMgGa upon the substitution of Al with Ga and Mg with Zn respectively, and approaches 54 kJ/mol as measured for CuZnAl. Similarly for rWGS, substitution causes an increase in the apparent activation energy from 69 kJ/mol in PdMgAl to 94 kJ/mol and 82 kJ/mol for PdZnAl, PdMgGa respectively, in the direction of CuZnAl (122 kJ/mol). The results suggest that the reactivity of Pd in methanol synthesis and rWGS approaches that of Cu upon substitution of irreducible species with Zn and Ga. In particular, these extraordinary differences in reactivity correspond to the formation of PdZn and Pd$_2$Ga IMCs upon reduction of PdZnAl and PdMgGa respectively and the presence of only pure Pd upon reduction of PdMgAl, as evidenced by the aforementioned characterization results. The similarity of the catalytic properties of PdZn and Cu has been reported in literature and was attributed to the similar electronic structure. Both exhibit similar valence electron densities of states (DOS) as confirmed by DFT, UPS and XPS.[34-37]

4.4.2 Steam reforming of methanol

The catalytic activities of the Pd-based catalysts derived from HTlc precursors in MSR tests are summarized in Table 4- 3. For all tested catalysts the main products were H$_2$, H$_2$O, CO and CO$_2$. Other reaction products such as formaldehyde or dimethylether were not observed.

Table 4- 3: Activity results for the Pd-based IMC catalysts for the steam reforming of methanol at 523 K.

Catalyst	Metal sites[a] [μmol/g)]	X_{MeOH} [%]	S_{CO2} [%]	Rate [μmol/(min·g)] MeOH converted	Rate [μmol/(min·g)] H$_2$ released	S_{H2} [%]	TOF [min^{-1}] MeOH	TOF [min^{-1}] H$_2$
PdZnAl	73	14.0	61.1	369	964	87	5.1	13.2
PdMgGa	20	15.3	16.4	404	874	72	20.2	43.7
PdMgAl	91	12.6	6.1	331	681	69	3.6	7.5

[a] estimated from the metal particle size determined by TEM

The PdZnAl and PdMgGa catalysts showed similar overall activity (9.5% methanol conversion), while the PdMgAl catalyst was somewhat less active (7% methanol conversion). The PdZnAl catalyst exhibited the highest hydrogen yield (660 μmol/(g$_{cat}$·min)) of all catalysts tested, and this hydrogen yield was 23% and 75% higher than those of PdMgGa and PdMgAl, respectively (Figure 4- 11). In terms of intrinsic activity for hydrogen production, the PdZnAl

and PdMgGa were 2 and 6 times respectively more active than PdMgAl. The hydrogen selectivities of PdMgGa and PdMgAl were significantly lower (70%) than that of PdZnAl (87%). While the reactivity of methanol on PdMgAl and PdMgGa is almost entirely dominated by methanol decomposition, PdZnAl shows considerable MSR activity (S$_{CO2}$=61%).
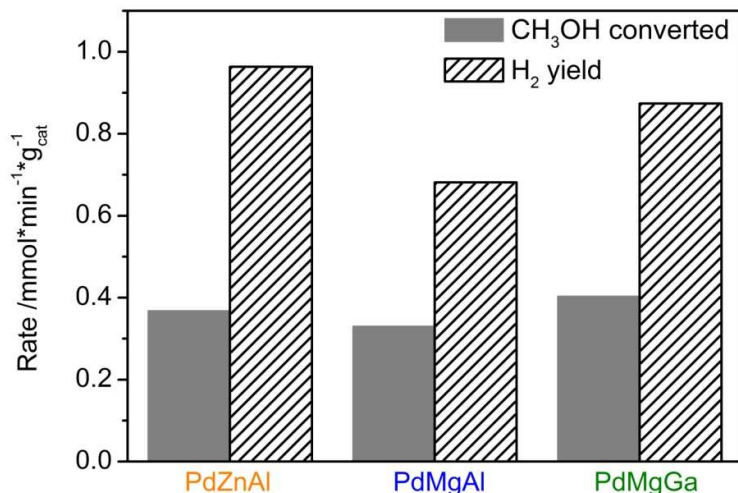

Figure 4- 11: Rate of MSR of PdZnAl, PdMgGa and PdMgAl catalysts in MSR conducted at 523 K.

Iwasa et al. [7] have attributed this CO$_2$ selectivity to the formation PdZn intermetallic phases during reduction of Pd/ZnO. However the CO$_2$ selectivities observed by Iwasa et al. were near 95% and thereby similar to those observed on CuZn based catalysts. It should be noted that the PdZn particles observed by Iwasa et al. [8] were large enough to produce rather sharp XRD peaks and where therefore far larger than the particles obtained in this work. It may therefore be possible that under reaction conditions the smaller particles decompose partially to yield metallic Pd, or that the methanol decomposition reaction is structure sensitive, and occurs faster on smaller particles. In accordance with the latter statement, Karim et al.[38], found a positive correlation between the number of small particles (< 1.5 nm) and decreasing selectivity towards CO$_2$ on Pd/ZnO catalysts using TEM analysis.

Iwasa et al.[8] and more recently, Haghofer et al.[9] have shown that Pd supported on Ga$_2$O$_3$ is also very selective to MSR with CO$_2$ selectivities above 80% , and have attributed this high selectivity to the formation of Pd-Ga IMCs. However, for the PdMgGa sample investigated herein the CO$_2$ selectivity (16%) is only somewhat higher than that of the PdMgAl (6%) catalyst, in which no IMCs are formed. Haghofer et al. [20] have shown by in-situ IR spectroscopy on Pd/Ga$_2$O$_3$ that the intermetallic Pd$_2$Ga surface is not entirely stable during MSR

at 480 K, and that metallic Pd forms on the surface, as evidenced by the presence of bridge-bonded CO. At the higher temperatures (523 K) used in this study, such surface decomposition may occur to a greater extent and leave a higher fraction of exposed Pd, thus leading to lower CO_2 selectivities. It should be noted that the promotional effect of Pd_2Ga formation on the selectivity is far more evident during methanol synthesis (as described previously) as compared to steam reforming. To that end, the higher hydrogen pressures and virtual absence of water during methanol synthesis may ensure the stability of the Pd_2Ga intermetallic surface responsible for the enhanced selectivity. In contrast, the presence of large concentrations of water during MSR may lead to the decomposition of this surface into metallic Pd and Ga_2O_3. Corresponding to its lower formation temperature, the PdZn IMC seems to possess a greater stability in less reducing atmospheres than Pd_2Ga and the beneficial intrinsic catalytic properties prevail to a greater extent in the PdZnAl catalyst.

4.5 Conclusion

A flexible synthetic approach for the synthesis of nanoparticles of intermetallic compounds has been presented. PdZn (1.8 nm) and Pd_2Ga (6.1 nm) nanoparticles were obtained from HTlc precursor with a homogeneous distribution of Pd and intimate interaction with the other reducible metal species. At a degree of substitution of 1 mol%, full incorporation of Pd^{2+} in the HTlc lattice has been confirmed for PdZnAl, while in PdMgAl and PdMgGa the majority of Pd^{2+} was incorporated. Upon reduction in hydrogen, metallic Pd segregated from the precursors at low temperature and for PdZnAl the PdZn IMC is formed at 523 K probably via a Pd_2Zn intermediate stage. Formation of Pd_2Ga IMC in PdMgGa requires 773 K. In comparison with the analogous PdMgAl sample, which does not contain a second reducible species and yields monometallic Pd nanoparticles, the CO absorption properties as well as the catalytic properties have markedly changed through formation of the IMCs. Improved activities and selectivities in MSR, and methanol synthesis from CO_2 have been observed. This effect is larger for CO_2 hydrogenation than for MSR and for the PdZn-based than for the Pd_2Ga-based catalyst. These differences are probably related to the different sensitivity of the IMC surface against decomposition into Pd metal and oxide. The more reducing conditions of methanol synthesis seem to stabilize the IMC better than the more oxidizing conditions of MSR. Under steady state conditions our Pd-based IMC catalysts are inferior to Cu/ZnO reference systems. Nevertheless, the potential of these materials for MSR operation at higher temperature and under changing reaction conditions like on-off operations remains to be investigated. Also the stability of the IMC surface under different conditions needs further investigation.

4.6   References

[1]   G. A. Olah, A. Goeppert, G. K. S. Pakash, *Beyond Oil and Gas: The Methanol Economy*, Wiley-VCH Verlag GmbH & Co. KGaA, Weinheim, **2006**.

[2]   R. Schlögl, *Chemsuschem* **2010**, *3*, 209-222.

[3]   P. J. de Wild, M. J. F. M. Verhaak, *Catalysis Today* **2000**, *60*, 3-10.

[4]   F. Joensen, J. R. Rostrup-Nielsen, *Journal of Power Sources* **2002**, *105*, 195-201.

[5]   R. Schögl, *Energy Storage Materials*, Walter de Gruyter, Berlin, **2012**.

[6]   L. Guczi, A. Erdôhelyi, *Catalysis for Alternative Energy Generation*, 1st ed., Springer **2012**.

[7]   N. Iwasa, S. Masuda, N. Ogawa, N. Takezawa, *Applied Catalysis A: General* **1995**, *125*, 145-157.

[8]   N. Iwasa, T. Mayanagi, N. Ogawa, K. Sakata, N. Takezawa, *Catalysis Letters* **1998**, *54*, 119-123.

[9]   A. Haghofer, K. Föttinger, F. Girgsdies, D. Teschner, A. Knop-Gericke, R. Schlögl, G. Rupprechter, *Journal of Catalysis* **2012**, *286*, 13-21.

[10]   S. Penner, H. Lorenz, W. Jochum, M. Stöger-Pollach, D. Wang, C. Rameshan, B. Klötzer, *Applied Catalysis A: General* **2009**, *358*, 193-202.

[11]   H. Lorenz, S. Penner, W. Jochum, C. Rameshan, B. Klötzer, *Applied Catalysis A: General* **2009**, *358*, 203-210.

[12]   C. Rameshan, W. Stadlmayr, C. Weilach, S. Penner, H. Lorenz, M. Hävecker, R. Blume, T. Rocha, D. Teschner, A. Knop-Gericke, R. Schlögl, N. Memmel, D. Zemlyanov, G. Rupprechter, B. Klötzer, *Angewandte Chemie International Edition* **2010**, *49*, 3224-3227.

[13]   K. Föttinger, J. A. van Bokhoven, M. Nachtegaal, G. n. Rupprechter, *The Journal of Physical Chemistry Letters* **2011**, *2*, 428-433.

[14]   T. Conant, A. M. Karim, V. Lebarbier, Y. Wang, F. Girgsdies, R. Schlögl, A. Datye, *Journal of Catalysis* **2008**, *257*, 64-70.

[15]   A. Ota, M. Armbrüster, M. Behrens, D. Rosenthal, M. Friedrich, I. Kasatkin, F. Girgsdies, W. Zhang, R. Wagner, R. Schlögl, *The Journal of Physical Chemistry C* **2010**, *115*, 1368-1374.

[16]   K. Kovnir, J. Osswald, M. Armbruster, D. Teschner, G. Weinberg, U. Wild, A. Knop-Gericke, T. Ressler, Y. Grin, R. Schlogl, *Journal of Catalysis* **2009**, *264*, 93-103.

[17]   X. Duan, D. G. Evans, *Layered Double Hydroxides*, Springer-Verlag, Berlin, Heidelberg, **2006**.

[18]   C. Forano, T. Hibino, F. Leroux, C. Taviot-Gueho, in *Handbook of Clay Science* (Eds.: F. Bergaya, B. K. G. Theng, G. Lagaly), Elsevier, **2006**, pp. 1021-1095.

[19]   F. Cavani, F. Trifirò, A. Vaccari, *Catalysis Today* **1991**, *11*, 173-301.

[20]   M. Behrens, I. Kasatkin, S. Kŭhl, G. Weinberg, *Chemistry of Materials* **2009**, *22*, 386-397.

[21]   N. Iwasa, T. Mayanagi, W. Nomura, M. Arai, N. Takezawa, *Applied Catalysis A: General* **2003**, *248*, 153-160.

[22]   W. Jochum, S. Penner, R. Kramer, K. Föttinger, G. Rupprechter, B. Klötzer, *Journal of Catalysis* **2008**, *256*, 278-286.

[23]   A. G. Christy, S. M. Clark, *Physical Review B* **1995**, *52*, 9259-9265.

[24]   G. Demazeau, I. Omeran, M. Pouchard, P. Hagenmuller, *Materials Research Bulletin* **1976**, *11*, 1449-1452.

[25]   S.-J. Kim, S. Lemaux, G. Demazeau, J.-Y. Kim, J.-H. Choy, *Journal of Materials Chemistry* **2002**, *12*, 995-1000.

[26]   A. Eyssler, P. Mandaliev, A. Winkler, P. Hug, O. Safonova, R. Figi, A. Weidenkaff, D. Ferri, *The Journal of Physical Chemistry C* **2010**, *114*, 4584-4594.

[27]   N. Sheppard, C. De La Cruz, *Catalysis Today* **2001**, *70*, 3-13.

[28]   K. Kovnir, M. Armbrüster, D. Teschner, T. V. Venkov, F. C. Jentoft, A. Knop-Gericke, Y. Grin, R. Schlögl, *Science and Technology of Advanced Materials* **2007**, *8*, 420-427.

[29]   F. Prinetto, M. Manzoli, G. Ghiotti, M. d. J. Martinez Ortiz, D. Tichit, B. Coq, *Journal of Catalysis* **2004**, *222*, 238-249.

[30]   N. Iwasa, H. Suzuki, M. Terashita, M. Arai, N. Takezawa, *Catalysis Letters* **2004**, *96*, 75-78.

[31]   T. Fujitani, M. Saito, Y. Kanai, T. Watanabe, J. Nakamura, T. Uchijima, *Applied Catalysis A: General* **1995**, *125*, L199-L202.

[32]   W. Wang, S. Wang, X. Ma, J. Gong, *Chemical Society Reviews* **2011**, *40*, 3703-3727.

[33]   T. Inui, T. Takeguchi, *Catalysis Today* **1991**, *10*, 95-106.

[34]   A. P. Tsai, S. Kameoka, Y. Ishii, *Journal of the Physical Society of Japan* **2004**, *73*, 3270-3273.

[35]   A. Bayer, K. Flechtner, R. Denecke, H.-P. Steinrück, K. M. Neyman, N. Rösch, *Surface Science* **2006**, *600*, 78-94.

[36]   K. M. Neyman, K. H. Lim, Z.-X. Chen, L. V. Moskaleva, A. Bayer, A. Reindl, D. Borgmann, R. Denecke, H.-P. Steinrück, N. Rösch, *Physical Chemistry Chemical Physics* **2007**, *9*, 3470-3482.

[37]   Z.-X. Chen, K. M. Neyman, A. B. Gordienko, N. Rösch, *Physical Review B* **2003**, *68*, 075417.

[38]   A. Karim, T. Conant, A. Datye, *Journal of Catalysis* **2006**, *243*, 420-427.

Supplementary Information

Sample identification

Label	FHI internal sample number
PdZnAl	11120
PdMgGa	10230
PdMgAl	9319
CuZnAl	9270

CuZnAl reference catalyst

The CuZnAl HTlc precursor was precipitated from a $Cu^{2+}/Zn^{2+}/Al^{3+}$ nitrate solution (total metal concentration: 0.43M; Cu:Zn:Al = 50:17:33) with an aqueous solution of NaOH (0.3M) and Na_2CO_3 (0.045M) as the precipitating agent. The reaction was carried out at a constant pH value (pH = 8 ± 0.7) at 298 K – pH and temperature were controlled by the automated lab reactor system (Labmax from Mettler Toledo). After an ageing time of 1 h the blue powder was isolated by filtration, washing and drying at 373 K for 13 h. Afterwards the sample was calcined in air at 603 K for 3 h (heating rate 2 K/min). The Cu based catalyst was obtained by in-situ reduction of the calcined sample in 5 Vol% H_2/Argon and a heating rate of 6 K/min at 603 K for 30 min before the catalytic measurement was performed at 523 K.

For the determination of the specific Cu surface area N_2O-reactive frontal chromatography (RFC) is used and carried out at 303 K (details see Ref. 20). This technique is based on the decomposition of nitrous oxide molecules on the surface of copper to produce chemisorbed oxygen atoms and gas phase nitrogen. The Cu surface area was 7 m²/g.
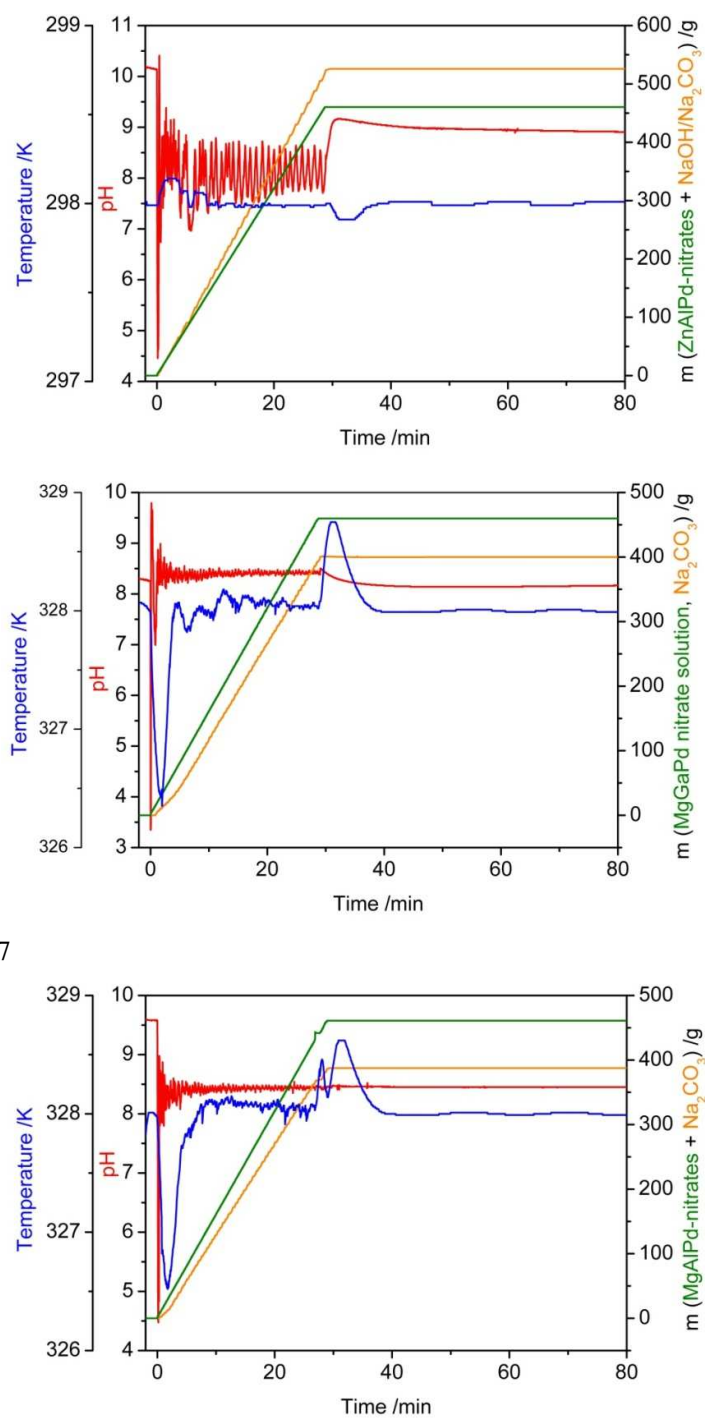
7

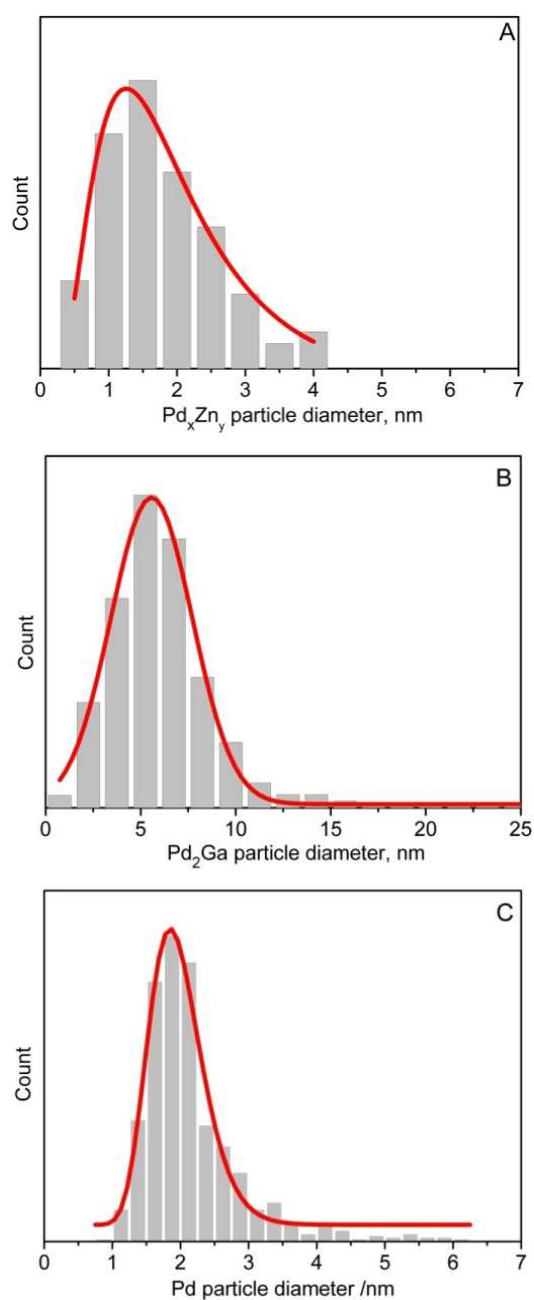Figure S4- 1: Synthesis protocols of PdZnAl, PdMgGa and PdMgAl HTlc precursors.

Figure S4- 2: Particle size distributions of (A) PdZnAl reduced at 523 K (B) PdMgGa reduced at 773 K and (C) PdMgAl reduced at 523 K.

Chapter 5: Final summary and conclusion

In the present work a novel, feasible synthesis approach of supported Pd-based intermetallic nanoparticles derived from ternary Hydrotalcite-like compounds (HTlc) was introduced. Mixed HTlc with the nominal composition $(Pd^{2+}, M^{2+})_{0.70}(M^{3+})_{0.30}(OH)_2(CO_3)_{0.15} \cdot m\ H_2O$ were synthesized by pH-controlled co-precipitation. Mg^{2+}/Ga^{3+} and Zn^{2+}/Al^{3+} were chosen as M^{2+}/M^{3+} combinations to enable formation nanoparticulate Pd_2Ga and $PdZn$ intermetallic compounds on a $MgO/MgGa_2O_4$ and $ZnO/ZnAl_2O_4$ support, respectively. In addition, a PdMgAl HTlc was synthesized to exemplify a monometallic Pd reference compound on a $MgO/MgAl_2O_4$ support. The effects of Pd loading, pH and temperature on the resulting co-precipitated HTlc have been examined in detail.

For all the different precursor systems no Pd containing by-phase was observed by XRD up to a Pd^{2+} content of 2.5 mol% of the cations. However, Pd rich areas on the external surface of the plate-like HTlc particles were noticed by SEM-EDX with increased Pd loading in case of PdMgGa. Apparently a limit of incorporation into the HTlc lattice exists at ≤ 1 mol%. This rather low value was related to the differences in size and coordination requirements of Pd^{2+} compared to other typical M^{2+} cation in HTlc. Incorporation of Pd into the HTlc structure requires octahedral coordination of the cations, while Pd^{2+} ions prefer square planar coordination in aqueous solution. It could be shown by XANES that, at the same substitution degree of M^{2+} by Pd^{2+} of 1 mol%, full incorporation of Pd^{2+} was confirmed for PdZnAl HTlc, while in PdMgGa and PdMgAl the majority of Pd^{2+} was incorporated, but a significant fraction of Pd^{2+} was present in a segregated form with a local environment similar to PdO, i.e. in a square-planar coordination. Apparently Zn^{2+} containing HTlc facilitate the incorporation of Pd^{2+} into the HTlc structure. Upon TPR, the hydrogen consumption at room temperature was in good correlation with the fraction of segregated PdO-like species segregated. The Pd^{2+} fraction that was successfully incorporated into the HTlc lattice was reduced only upon heating in a separated reduction step. At Pd^{2+} loadings above the critical limit for incorporation, the partial incorporation into the PdMgGa precursor caused to a bimodal size distribution of the Pd metal particles formed at a reduction temperature of 473 K. The fraction of smaller Pd particles probably resulted from the incorporated Pd, while bigger ones were produced from the segregated PdO-like particles.

Upon thermal decomposition in reducing atmosphere of the PdMgGa HTlc precursor at higher temperature of 773 K supported Pd_2Ga nanoparticles were formed. Metallic Pd segregated from

the precursors at low temperature (T < 423 K) and reacts with the reducible species of the support upon further heating. For formation of PdZn from the PdZnAl HTlc, a reduction temperature of 523 K was sufficient, where PdZn is probably formed via a Pd_2Zn intermediate stage. The metallic and intermetallic phases were identified by HRTEM, IR studies of adsorbed CO and XANES measurements. Particle sizes ranging from < 2 nm to 6 nm were achieved depending on the precursor system, reduction temperature and metal loading. Independent of the degree of Pd^{2+} incorporation in the HTlc precursor, monomodal particle size distributions were obtained after complete reduction and formation of intermetallic phase. In case of the Pd_2Ga particles, a disordered shell probably of oxide material was observed after high temperature reduction, which suggests the presence of strong-metal-support-interaction (SMSI) between Pd_2Ga and the Gallia-containing support. The precursor decomposition and reduction processes were found to be rather complicated as anion decomposition and hydrogenation of the decomposition products interfered with reduction and formation of the intermetallic compound. Compared to the monometallic Pd particles obtained from the PdMgAl precursor, the CO adsorption properties of the IMC particles are strongly modified and lead to the absence or strong reduction of multiple bonded carbonyl. Alloying of Pd with Ga and Zn changes the geometric surface structure as well as the electronic structure and leads to the increased formation of isolated adsorption sites for CO. Furthermore, dynamic surface changes of intermetallic Pd_2Ga nanoparticles were noticed at prolonged CO exposure and higher coverage already at room temperature. The additional population of an adsorption site typical for metallic Pd suggested the partial oxidation of metallic Ga and the formation of finely dispersed metallic Pd patches on a partially decomposed Pd_2Ga surface. This effect of CO was suppressed at liquid nitrogen temperature. These results suggest that the outermost surface of the intermetallic Pd_2Ga compound, despite its partial covalent bonding, can be very reactive towards gas phase species if it is present in form of nanoparticles. Thus, the previously reported intrinsic stability of Pd-Ga intermetallic compounds in catalytic reactions, which was observed on unsupported bulk materials, is not necessarily transferable to a nanosized catalyst material and has to be addressed with regard to the catalytic reaction under study and the exact reaction conditions.

However, the intermetallic Pd_2Ga nanoparticles showed excellent performance in the selective semi-hydrogenation of acetylene. Under the chosen reaction conditions, the selectivity to ethylene was stable and identical to bulk a Pd_2Ga model catalyst, prepared by conventional metallurgical synthesis. Due to the successful nanostructuring, the activity per mass Pd increased by a factor of 5700. In comparison to a monometallic Pd reference catalyst, the selectivity was improved from 26% to 80%. Interestingly, the nanostructured Pd_2Ga catalyst

showed slow, but pronounced activation in the feed gas. Alternatively, the activation could be triggered faster by a treatment in oxidative atmosphere. These dynamics of the Pd_2Ga nanoparticles are discussed as an interplay of surface decomposition into Pd^0 and Ga_2O_3 in oxygen, similar to the state after incomplete reduction or prolonged CO exposure studied with IR spectroscopy, and reversal of the SMSI effect leading to an increase in exposed metallic surface area. The highly reactive Pd patches formed by the decomposition process undergo a further transformation in the feed gas and the active final state of the catalyst is probably attributed to a Pd_2Ga core ─ Pd/PdC_x shell configuration.

In addition, the supported PdZn, Pd_2Ga and Pd nanoparticles were tested in methanol steam reforming and methanol synthesis from CO_2. Improved activities and selectivities have been observed for the Pd_2Ga and PdZn nanoparticles compared to unmodified Pd particles. The catalysts containing intermetallic compounds were 100 and 200 times, respectively, more active for methanol synthesis than the monometallic Pd catalyst. The beneficial effect of Ga in the active phase was found to be more pronounced in methanol synthesis compared to steam reforming of methanol. This is probably related to insufficient stability of the reduced Ga species in the more oxidizing feed of the latter reaction.

Appendix

Curriculum vitae

Personal information

Name: Antje Ota
Date of birth: 29.03.1984
Place of birth: Hennigsdorf

Education

2003-2008	Study of chemistry at the Humboldt Universität zu Berlin - qualification: Diplom Chemiker
02-09/2008	Diploma thesis at the Leibniz-Institut für Katalyse e.V., Außenstelle Berlin. Title: Reformierung von Ethanol an Edelmetallkatalysatoren.
11/2008-03/2012	PhD thesis at the Fritz-Haber-Institute of the Max-Planck-Society in Berlin, Department of Inorganic Chemistry. Title: Synthesis, Characterization and Application of intermetallic Pd-X (Ga, Zn) Nanoparticles derived from ternary Hydrotalcite-like precursors.

Publications

A. Ota, M. Armbrüster, M. Behrens, D. Rosenthal, M. Friedrich, I. Kasatkin, F. Girgsdies, W. Zhang, R. Wagner, R. Schlögl: *The Intermetallic Compound Pd$_2$Ga as Selective Catalyst for the Semi-Hydrogenation of Acetylene: From Model to High Performance Systems.*
Journal of Physical Chemistry C **2011**, *115*, 1368-1374.

S. F. Moya, R. L. Martins, A. Ota, E. L. Kunkes, M. Behrens, M. Schmal: *Nanostructured supported palladium catalysts - Non-oxidative methane coupling.*
Applied Catalysis A: General **2012**, *411-412*, 105-113.

A. Ota, E. L. Kunkes, I. Kasatkin, E. Groppo, D. Ferri, R. M. Navarro Yerga, M. Behrens: *Methanol Synthesis and Methanol Steam Reforming on Supported Pd$_2$Ga and PdZn Intermetallic Nanoparticles. (submitted to Journal of Catalysis)*

M. Armbrüster, M. Behrens, F. Cinquini, K. Föttinger, Yu. Grin, A. Haghofer, B. Klötzer, A. Knop-Gericke, H. Lorenz, A. Ota, S. Penner, J. Prinz, C. Rameshan, Z. Révay, D. Rosenthal, G. Rupprechter, P. Sautet, R. Schlögl, L. Szentmiklósi, D. Teschner, D. Torres, R. Wagner, R. Widmer, G. Wowsnick: *How to control the selectivity of palladium-based catalysts in hydrogenation reactions: The role of subsurface chemistry. (submitted to ChemCatChem)*

A. Ota, J. Kröhnert, G. Weinberg, I. Kasatkin, E. L. Kunkes, F. Girgsdies, N. Hamilton, R. Schlögl, M. Behrens: *Dynamic surface processes of nanostructured Pd$_2$Ga Catalysts derived from ternary Hydrotalcite-like Precursors. (to be submitted)*

A. Ota, E. L. Kunkes, J. Kröhnert, M. Schmal, M. Behrens: *Particle Size Effect in Methane Activation over Supported Palladium Nanoparticles. (to be submitted)*

Oral presentations

Federal University of Rio de Janeiro, COPPE Institute Seminar, Rio de Janeiro, Brazil, 06.05.2010
Preparation of Pd based intermetallic compounds via a novel synthesis approach.

22. North American Meeting of the North American Catalysis Society, Detroit, USA, 05.-10.06.2011
Supported Intermetallic Pd$_2$Ga Nanoparticles: Synthesis, Characterization and Application.

Patent application

M. Behrens, A. Ota, R. Schlögl, M. Armbrüster, Y. Grin: *Palladium-modified hydrocalcites and their use as catalyst precursors.*
Application EP 10 002419.9 submitted on 9.05.2010.

Poster presentations

A.Ota, H. Ehrich, K. Jähnisch: *Pt-, Pd- und Rh-dotierte Co/ZnO-Katalysatoren für die Ethanolreformierung im Mikroreaktor.*
42. Jahrestreffen deutscher Katalytiker, 11. - 13.03.2009, Weimar, Germany

A. Ota, F. Girgsdies, M. Armbrüster, W. Zhang, R.Schlögl, M. Behrens: *Supported Pd-Ga Intermetallics as hydrogenation catalysts.*
43. Jahrestreffen deutscher Katalytiker, 10. - 12.03.2010, Weimar, Germany

A. Ota, M. Behrens: *Supported Pd-Ga Intermetallics as hydrogenation catalysts.*
15th Conference of GDCh, Division for Solid State Chemistry and Material Research,
20. - 21.09.2010, Berlin, Germany

A. Ota, D. Rosenthal, J. Kröhnert, M. Armbrüster, R. Schlögl, M. Behrens: *Supported Intermetallic Pd_2Ga: Synthesis, Characterization and Application.*
44. Jahrestreffen deutscher Katalytiker, 16.-18.03.2011, Weimar, Germany

A. Ota, D. Rosenthal, J. Kröhnert, M. Behrens, R. Schlögl: *Supported intermetallic Pd_2Ga nanoparticles investigated by CO-IR adsorption spectroscopy and X-ray Photoelectron Spectroscopy.*
7th Brazilian/German Workshop of Applied Surface Science, 03. - 08.04.2011, Buzios, Brazil

A. Ota, E. Kunkes, J. Kröhnert, I. Kasatkin, W. Zhang, F. Girgsdies, R. Schlögl, M. Behrens: *Pd-based Catalysts derived from Hydrotalcite-like compounds in CO_2 Hydrogenation.*
EuropaCat X, 28.08. - 02.09.2011, Glasgow, Great Britain